INVESTIGATING THE STRUCTURE OF ACTIVE GALACTIC NUCLEI: THE DUSTY TORUS

Marko Stalevski

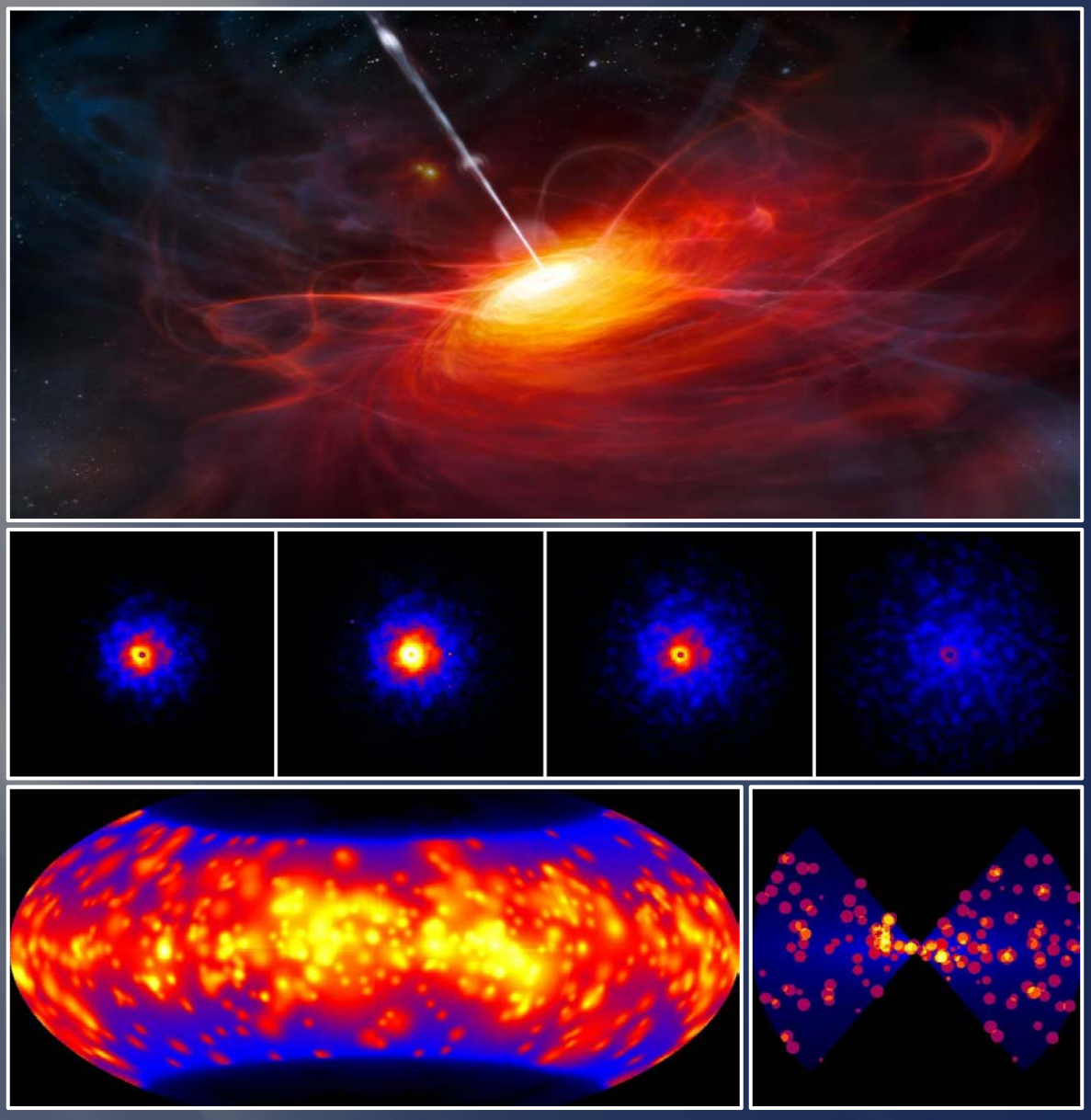

Doctoral Dissertation

Faculty of Mathematics
University of Belgrade

Faculty of Sciences
Ghent University

UNIVERSITY OF BELGRADE
FACULTY OF MATHEMATICS

GHENT UNIVERSITY
FACULTY OF SCIENCES

Marko Stalevski

INVESTIGATING THE STRUCTURE OF ACTIVE GALACTIC NUCLEI: THE DUSTY TORUS

Doctoral Dissertation

Belgrade, Ghent, 2012

Cover

– Top: artist's impression of an active galactic nuclei – a supermassive black hole surrounded by an accretion disk and enshrouded in a dusty doughnut-shaped torus. Credit: ESO/M. Kornmesser.

– Middle: simulated images of the dusty torus based on radiative transfer, from near- to mid- and far-infrared wavelengths.

– Bottom: calculated map of optical depth of the sky, as it would be seen from the center of an active galactic nuclei (left), based on the dust density distribution shown on the right.

Promotors

Prof. Dr. Maarten Baes
Department of Physics and Astronomy
Ghent University, Belgium

Prof. Dr. Dragana Ilić
Department of Astronomy
University of Belgrade, Serbia

Other members of the examination committee

Prof. Dr. Freddy Callens
President of the jury
Department of Solid State Sciences
Ghent University, Belgium

Prof. Dr. Sven De Rijcke
Department of Physics and Astronomy
Ghent University, Belgium

Prof. Dr. Martin Gaskell
Department of Physics and Astronomy
University of Valparaiso, Chile

Dr. Predrag Jovanović
Astronomical Observatory
Belgrade, Serbia

Dr. Luka Č. Popović
Astronomical Observatory
Belgrade, Serbia

Prof. Dr. Jean Surdej
Department of Astrophysics, Geophysics
and Oceanography
University of Liege, Belgium

Acknowledgements

This thesis was done under the supervision of Luka Č. Popović, Predrag Jovanović and Maarten Baes. I am truly indebted and thankful to all three of them for their guidance and selfless help along the way. My warmest gratitude also goes to Jacopo Fritz and to the numerous colleagues at Astronomical Observatory of Belgrade and the Department of Physics and Astronomy at the Ghent University, for sharing their knowledge and experience and countless useful discussions. I am very grateful to my parents for their support through out my entire education and to many friends for the encouragements. The work for this thesis was supported by the Ministry of Education, Science and Technological Development of the Republic of Serbia through the projects 'Astrophysical Spectroscopy of Extragalactic Objects' (176001) and 'Gravitation and the Large Scale Structure of the Universe' (176003), and by the European Commission (Erasmus Mundus Action 2 partnership between the European Union and the Western Balkans, http://www.basileus.ugent.be).

Contents

List of Figures

List of Tables

List of publications of the candidate

Stalevski, M., Fritz, J., Baes, M., Nakos, T., & Popović, L. Č. 2012, *3D radiative transfer modelling of the dusty tori around active galactic nuclei as a clumpy two-phase medium*, MNRAS, 420, 2756

Stalevski, M., Jovanović, P., Popović, L. Č., & Baes, M. 2012, *Gravitational microlensing of active galactic nuclei dusty tori*, MNRAS, 425, 1576

Stalevski, M. 2012, *SKIRTOR - database of modeled AGN dusty torus SEDs*, accepted for publication in BlgAJ

Popović, L. Č., Jovanović, P., Stalevski, M., et al. 2012, *Photocentric variability of quasars caused by variations in their inner structure: consequences for Gaia measurements*, A&A, 538, A107

Stalevski, M., Fritz, J., Baes, M., Nakos, T., & Popović, L. Č. 2011, *AGN Dusty Tori as a Clumpy Two-Phase Medium: the 10 μm Silicate Feature*, Baltic Astronomy, 20, 490

Baes M., Verstappen J., De Looze I., Fritz J., Saftly W., Vidal Pérez E., Stalevski M., Valcke S., 2011, *Efficient Three-dimensional NLTE Dust Radiative Transfer with SKIRT*, ApJS, 196, 22

Jovanović, P., Popović, L. Č., Stalevski, M., Shapovalova, A. I. 2010, *Variability of the Hβ Line Profiles as an Indicator of Orbiting Bright Spots in Accretion Disks of Quasars: A Case Study of 3C 390.3*, ApJ, 718, 168

Stalevski, M., Jovanovic, P., & Popovic, L. C. 2010, *Perturbations In The Accretion Disk Emissivity: Theory Versus Observations*, POBeo, 89, 387

Stalevski, M., Jovanović, P., Popović, L. Č. 2008, *Line profile variability due to perturbations in AGN accretion disk emissivity*, POBeo, 84, 491

Резиме

АКТИВНА ГАЛАКТИЧКА ЈЕЗГРА Данас је опште прихваћено да се у средишту сваке масивне галаксије налази супермасивна црна рупа. Уочен је већи број корелација између маса ових црних рупа и динамичких и структурних особина галаксија у којима се налазе. Конкретно, корелација између маса црних рупа и маса средишњих овала њихових галаксија сугерише да постоји и веза између њиховог раста (Kormendy & Richstone, 1995; Kormendy & Gebhardt, 2001). Активно галактичко језгро (АГЈ) представља фазу у развоју галаксије током које околна материја интензивно упада у супермасивну црну рупу расте приликом чега се њена маса увећава. Појам АГЈ обухвата мноштво енергијски снажних феномена који су последица таквог пада материје, тј. акреције, у црну рупу.

Зрачење које потиче из АГЈ настаје услед конверзије гравитационе потенцијалне енергије у термалну, током спиралног пада материје у супермасивну црну рупу кроз акрециони диск (Lynden-Bell, 1969). Њихова луминозност може да буде и до 10000 пута већа од луминозности обичне галаксије. Израчени континуум покрива широк спектрални опсег, од X до радио подручја, делимично је поларизован и променљив у току времена. Зрачење из овог централног региона јонизује околну средину, стварајући услове за појаву јаких емисионих линија, суперпонираних на континуум. Под одређеним условима може доћи до појаве уских снопова материје ("млазева") нормално на акрециони диск.

Још од открића да оријентација Сејферт 1 галаксија није насумична уочено је да особине АГЈ зависи од угла посматрања (Keel, 1980). Ово је довело до тзв. "уједињења по оријентацији" (Antonucci, 1993; Urry & Padovani, 1995), по којем су АГЈ у основи слични објекти, чија привидно другачија појава зависи од угла под којим се посматрају (види сл. 1). У овом обједињеном моделу, централна црна рупа је окружена геометријски танким и оптички дебелим акреционим диском који је извор јаког X-зрачења и UV/оптичког континуума (Jovanović, 2012). Диск је окружен турбулентним, густим гасом који је извор емисионих линија, тзв. широколинијска област (Gaskell, 2009). Акрециони диск и широколинијска област су обавијени геометријски и оптички дебелим појасом прашине, приближно распоређене у виду торуса, која апсорбује упадно зрачење и поново га емитује у инфрацрвеном делу спектра. Поред ових компоненти, присутан је и гас који карактерише мања густина и брзина кретања, који је извор уских емисионих линија - тзв. усколинијска област. Широке линије и термални континуум могу бити уочени само при малим инклинацијама, када их торус прашине не заклања, и тада се објекат означава као активна галаксија типа 1. При већим инклинацијама, торус прашине апсорбује UV/оптички континуум и широке линије и такав објекат ће бити сврстан у активну галаксију типа 2. Ако се објекат у коме је присутан млаз материје избачен нормално на акрециони диск, посматра дуж тог млаза, биће детектован снажан нетермални континуум, који је по-

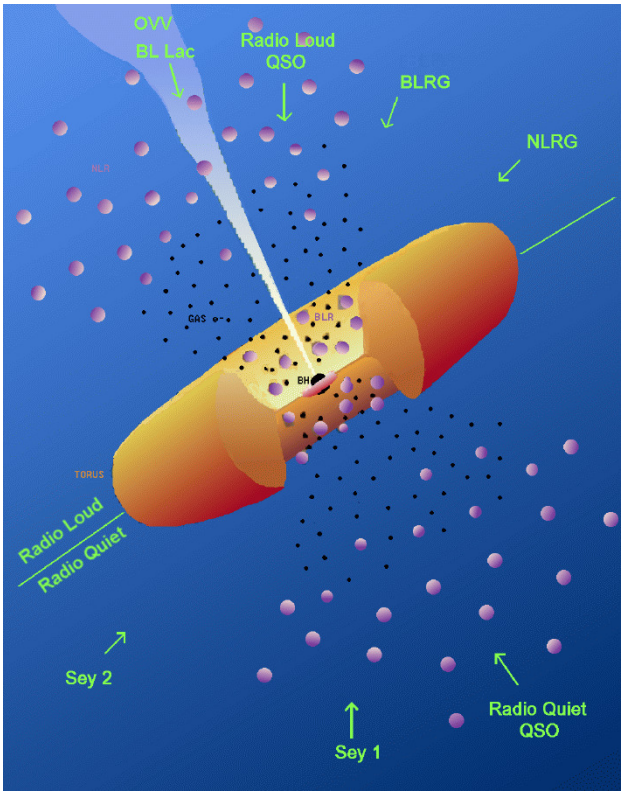

Слика 1 Шема стандардног обједињеног модела АГЈ. У зависности од угла посматрања различите емисионе области су изложене погледу посматрача који ће сходно томе објекат сврстати у одговарајући тип АГЈ. (M. Polletta, на основу Urry & Padovani, 1995).

ларизован и веома променљив у току времена (види Antonucci, 2012 за свеобухватан преглед различитих типова АГЈ).

Масе супермасивних црних рупа се могу лако одредити код неких типова АГЈ, (Dibai, 1977). Поред тога, АГЈ тренутно представљају једини начин за изучавање еволуције супермасивних црних рупа током космичког времена. АГЈ спадају у најсјајније квази-стабилне изворе зрачења у универзуму, и као такви представљају драгоцене изворе информација о космичкој еволуцији све до великих црвених помака. Да бисмо разумели како црне рупе расту током космичког времена и њихову везу са растом галаксија, неопходно је да у потпуности разумемо како функционишу АГЈ. Стандардни модел који је представљен у преходном делу текста мора бити проширен да би био у стању да објасни неке од посматраних феномена.

ЦИЉ ТЕЗЕ Циљ ове тезе је да се начини корак напред ка бољем разумевању структуре АГЈ, са нагласком на торус прашине, који има веома важну улогу у стандардном моделу АГЈ. Материја која упада у супермасивну црну рупу преко акреционог диска потиче управо из овог торуса, који, иако представља кључни елемент АГЈ, још увек није довољно добро испитан. Основна слика је јасна већ неко време

али постоје многа неразјашњена питања. Међу њима су посматрани интензитет и облик тзв. силикатне карактеристике (емисиона или апсорпциона трака која се појављује на 10 и 18 μm) чијим проучавањем се може доћи до увида о расподели и хемијском саставу прашине у торусу. Наиме, посматрани интензитет и облик ове силикатне карактеристике често одступа од теоријских предвиђања. Још један проблем присутан у многим истраживањима је недостатак емисије у блиском инфрацрвеном подручју када се пореде посматране спектралне енергијске расподеле са оним које предвиђају теоријски модели. Међу осталим неразјашњеним проблемима су и питања порекла, формирања и стабилности торуса. Иако је главни део истраживања у овој тези посвећен моделовању и анализи торуса прашине, такође су испитани и неки сродни феномени, као што су пертурбације у акреционом диску. Развијени модели торуса и диска су примењени у испитивању утицаја гравитационих микросочива на зрачење торуса и променљивости фотоцентра квазара. У даљем тексту укратко ћемо изложити резултате истраживања приказаних у овој тези и навести најважније закључке до којих се дошло.

ТОРУС ПРАШИНЕ Конструисан је нови, физички реалнији модел торуса, у коме је прашина предствљена као тзв. двофазна средина, са грудвама високе густине које су уроњене у хомогено распоређену прашину ниске густине. За израчунавање спектралних енергијских расподела и слика торуса на различитим таласним дужинама, користили смо SKIRT, 3D код за пренос зрачења заснован на Монте Карло методи (Baes et al., 2003, 2011). Генерисали смо мрежу модела за различите параметре, анализирали карактеристике инфрацрвене емисије и упоредили их са карактеристикама модела у којима се прашина налази искључиво у грудвама и модела у којима је прашина хомогено распоређена. На основу наше анализе, извели смо следеће закључке (Поглавље 2; Stalevski et al., 2011, 2012a; Stalevski, 2012c):

(i) Облик и количина емисије у блиском и средњем инфрацрвеном подручју су одређени условима и стањем у којем се налази прашина близу унутрашње ивице торуса: модели са идентичним параметрима али са различитим насумичним распоредом грудви могу да резултирају сасвим другачијим спектралним енергијским расподелама.

(ii) Расподела прашине, оптичка дубина, величина грудви и конкретан распоред грудви утичу на појаву силикатне карактеристике на 10 μm. Силикатна карактеристика је природно ослабљена у грудвастим моделима, али и модели са хомогено распоређеном прашином могу да имају силикатне карактеристике разних интензитета.

(iii) Прашина ниске густине, која се налази између грудви, значајно доприноси емисији у блиском инфрацрвеном домену. Према томе, прашина као двофазна

средина може да представља природно решење за проблем недостатка емисије у блиској инфрацрвеној области, са којим се сусрело више аутора приликом поређења посматраних спектралних енергијских расподела са оним који предвиђају тренутно доступни модели.

На сл. 2 дате су упоредо спектралне енергијске расподеле двофазног, грудвастог и модела са хомогеном расподелом прашине.

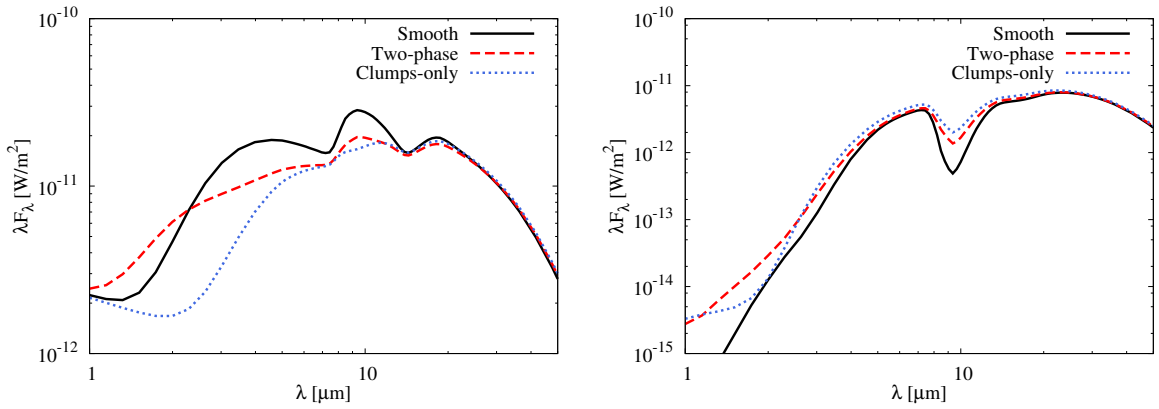

Слика 2 Поређење спектралних енергијских расподела различитих модела. Пуна линија представља модел са хомогеном расподелом прашине, испрекидана линија двофазни модел, тачкаста линија грудвасти модел. Леви панел: поглед на торус одозго. Десни панел: поглед на торус са стране.

УТИЦАЈ ГРАВИТАЦИОНИХ МИКРОСОЧИВА Објекти код којих услед ефекта гравитационих сочива долази до појаве више ликова представљају веома моћан алат за изучавање величине и структуре и галаксије која има улогу сочива и извора који се налази у позадини. У одређеном броју оваквих система у којима је извор квазар, однос флуксева између ликова одступа од вредности које предвиђају једноставни модели сочива. Када се испитује ова аномалија односа флуксева, важно је да се утврди стварни однос флуксева, у одсуству утицаја микросочива. У принципу, то може да се уради ако се посматрају емисионе линије, инфрацрвено или радио подручје, јер свака од ових емисионих области би требало да је довољно велика да ефекти микросочива не дођу до изражаја. Међутим, у свим радовима до сада присутним у литератури нису коришћени реални модели торуса прашине када је испитиван утицај микросочива. Користећи наш двофазни модел торуса прашине као извор, симулирали смо утицај мапе појачања микросочива услед звезда у галаксији-сочиву, са циљем да испитамо да ли микросочива могу значајније да утичу на инфрацрвену емисију торуса. Из нашег истраживања издвајамо следеће закључке (Поглавље 3; Stalevski et al., 2012b):

(i) Упркос величини торуса прашине АГЈ, микросочива могу значајно појачати његову инфрацрвену емисију. Како се ефективна величина торуса мења са

таласном дужином, тако и амплитуда појачања зависи од таласне дужине (види сл. 3). Појачање је највеће у блиско инфрацрвеном подручју, брзо опада ка средњем инфрацрвеном и остаје готово константно у далеком инфрацрвеном домену.

(ii) Пошто утицај микросочива зависи од величине извора, параметри који одређују величину торуса имају веома значајну улогу. Торуси чији радијус не прелази 10 pc могу бити под знатним утицајем микросочива.

(iii) Процењена времена између почетка и максимума појачања се крећу од неколико десетина до неколико стотина година.

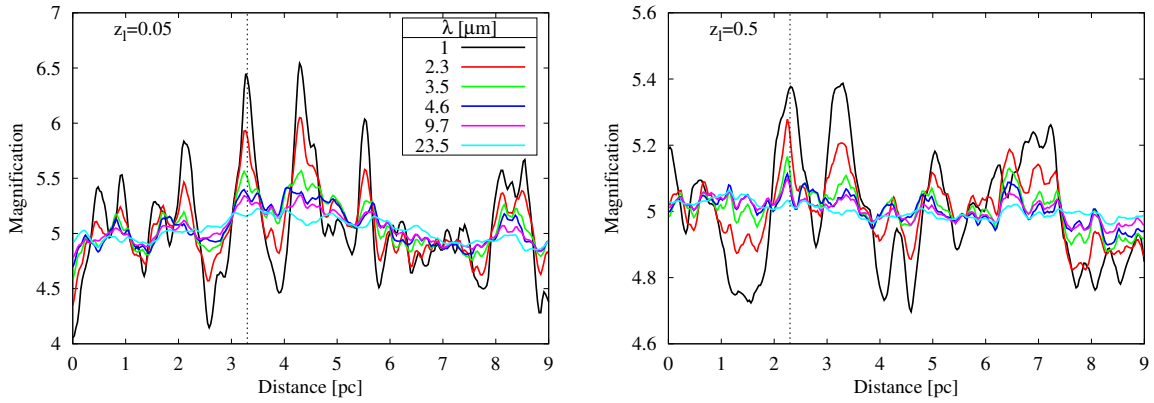

Слика 3 Симулиране криве сјаја под утицајем микросочива за различите таласне дужине (означене у легенди), за галаксију-сочиво која се налази на црвеном помаку од 0.05 (леви панел) и 0.5 (десни панел). Уочити различити распон вредности на y оси на приказаним панелима.

Имајући у виду тако дугачке временске скале, изучавање ефекате микросочива није нарочито погодан метод за одређивање параметера торуса прашине. Међутим, резултате овог истраживања треба имати на уму када се испитује аномалија односа флуксева код квазара са више ликова јер је тада битно утврдити стварни однос флуксева, у одсуству утицаја микросочива. Резултати истраживања показују да инфрацрвено зрачење торуса прашине може бити под значајним утицајем микросочива у неким случајевима, тако да посматрања у овом домену представљају мање поуздан метод за одређивање стварног односа флуксева.

ПЕРТУРБАЦИЈЕ У АКРЕЦИОНОМ ДИСКУ Нека физичка разматрања указују да варијабилност акреционог диска не може бити осно-симетрична, већ се јавља на одређеном делу диска у виду области високе емисивности, тзв. сјајне "пеге". Уколико је варијабилност изазвана сјајном пегом значајна, то може имати битне последице по метод реверберације за одређивање структуре АГЈ као и за потраге за двојним супермасивним црним рупама. У овом истраживању моделирали смо пер-

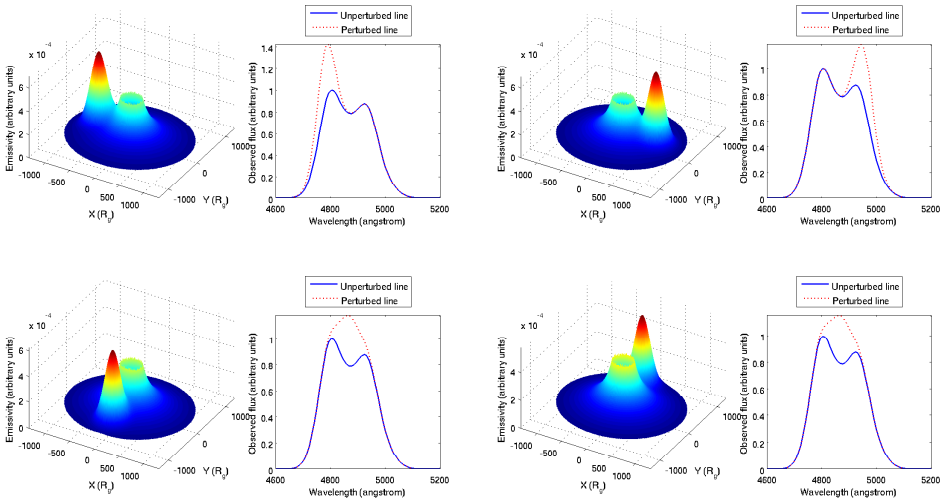

Слика 4 Пертурбована емисивност акреционог диска и одговарајући пертурбовани и непертурбовани профили Hβ линије. У зависности од положаја, сјајна пега утиче само на једно од крила линије или на језгро линије.

турбације у акреционом диску у виду сјајне пеге. Развијен модел смо применили на посматране профиле Hβ линије код квазара 3C 390.3. Из овог истраживања издвајамо следеће закључке (Поглавље 4; Jovanović et al., 2010; Stalevski et al., 2010:

(i) Модел пертурбације емисивности акреционог диска у виду сјајне пеге може успешно да објасни различите облике профила и варијабилност линија са два пика. (види сл. 4).

(ii) Користећи овај модел, успешно смо репродуковали посматране варијације профила Hβ линије код квазара 3C 390.3, укључујући два велика излива енергије која су примећена у датом периоду.

(iii) Наши резултати подржавају хипотезу да су пертурбације емисивности акреционог диска највероватније узроковане фрагментацијом спиралног крака у диску.

ВАРИЈАБИЛНОСТ ФОТОЦЕНТРА КВАЗАРА У овом делу истраживања користили смо оба претходно развијена модела торуса прашине и пертурбованог акреционог диска ради изучавања промена положаја фотоцентра квазара, изазваних великим променама емисивности диска и променама у структури торуса, а у контексту будуће Gaia мисије. Gaia мисија ће носити астрометријски интерферометар са циљем да са високом прецизношћу одреди астрометријске параметре за чак милијарду објеката. Очекује се да ће се међу овим објектима наћи и око 500 000 квазара. На основу ових квазара биће сачињен нови небески референтни систем. Разматрали смо пертурбације у акреционом диску и промене зрачења расејаног на прашини у

торусу. Проценили смо колико ови ефекти могу да допринесу померању фотоцентра и да ли ће Gaia бити у могућности да их детектује. На основу нашег истраживања, издвајамо следеће закључке (Поглавље 5; Popović et al., 2012):

(i) Пертурбације у акреционом диску могу да изазову померај фотоцентра који ће мисија Gaia бити у стању да детектује. Очекивани максимални померај (у случају када је сјајна пега на ивици диска) је реда величине неколико мили лучних секунди.

(ii) Значајан померај фотоцентра може се јавити и услед промена у структури торуса, у случају када је централни извор заклоњен прашином. Максимални померај износи неколико мили лучних секунди, што ће Gaia такође моћи да детектује.

(iii) Посматрана варијабилност фотоцентра код два посматрана квазара не може бити објашњена променама у њиховој унутрашној структури (тј. у акреционом диску и торусу прашине). Посматране варијације могу да буду објашњене у случају да се у средиштима извора налазе по два променљива региона. Ово, као и комплексни облици широких линија, указују да су ова два објекта добри кандидати за системе двојних супермасивних црних рупа.

БУДУЋИ РАД Рад представљен у оквиру ове тезе је део текућег истраживања које ће бити настављено у неколико праваца. Наставићемо и проширити рад на моделирању торуса прашине са унапређеном верзијом SKIRT кода. Размотрићемо сложеније расподеле прашине, попут вишефазне, влакнасте средине какве произилазе из хидродинамичких симулација. Такође ћемо наставити и проширити представљено истраживање утицаја гравитационих сочива, узимајући у обзир ефекте мили и макро сочива, што ће омогућити боље разумевање аномалије односа флуксева код квазара са више ликова.

Samenvatting

Actieve galactische kernen Het is vandaag door de meeste sterrenkundigen aanvaard dat alle massieve melkwegstelsels een supermassief zwart gat in hun kern herbergen. Er blijken ook een aantal correlaties te bestaan tussen de massa van dit supermassief zwart gat en de structurele en dynamische eigenschappen van de gastgalaxie. De correlatie tussen de massa's van supermassieve zwarte gaten en de bulten van hun gastgalaxieën suggereren een verband tussen de groei van beiden (Kormendy & Richstone, 1995; Kormendy & Gebhardt, 2001). Een actieve galactische kern (AGN) is een fase in het leven van een melkwegstelsel, waarbij de groei van het supermassieve zwarte gat rechtstreeks waarneembaar is. De term AGN is een verzamelnaam voor een reeks van verschillende energetische fenomenen in de kernen van melkwegstelsels, die allen worden aangedreven door materie die in een redelijk hoog tempo invalt op een supermassief zwart gat.

De straling van AGNs onstaat door de omzetting van gravitationele potentiële energie in thermische energie, via materie die op een supermassief zwart gat invalt langs een accretieschijf (Lynden-Bell, 1969). De lichtkracht van een AGN kan tot 10000 keer groter zijn dan de totale lichtkracht van een normaal melkwegstelsel. De uitgestraalde continuümenergie bestrijkt een breed gedeelte van het elektromagnetisch spectrum (gaande van Röntgenstraling to radiostraling), is gedeeltelijk gepolariseerd en veranderlijk in de tijd. Straling van de centrale motor ioniseert het omliggende medium, waardoor het de voorwaarden creëert voor de productie van sterke emissielijnen bovenop het continuüm. In sommige gevallen verschijnen ook sterk gecollimeerde en snelle jets loodrecht op de accretieschijf.

Sinds de ontdekking van Keel (1980) dat de oriëntatie van Seyfert 1 galaxieën (één van de deelklassen van de AGN familie) niet willekeurig is, is het algemeen aanvaard dat de schijnbare aard van een AGN varieert naargelang de hoek waaronder die gezien wordt vanop aarde. Dit heeft geleid tot het beeld van de oriëntatie-unificatie (zie Antonucci, 1993; Urry & Padovani, 1995). Het centrale punt van deze theorie is dat de intrinsieke structuur van AGNs grotendeels gelijkaardig is, maar wat we waarnemen een sterke functie is van de oriëntatie (zie Figuur 5). In dit geünificeerde model is het centrale supermassieve zwarte gat omgeven door een geometrisch dunne accretieschijf die de bron is van de sterke continuümstraling in Röntgen, UV en optische straling (zie Jovanović, 2012, en referenties daarin). Boven en onder de accretieschijf bevindt zich het bredelijnengebied, dat bestaat uit een turbulent en snel bewegend gas met een hoge dichtheid dat rond het supermassieve zwarte gat roteert (zie Gaskell, 2009, voor een overzicht). Zowel de accretieschijf als het bredelijnengebied zijn omgeven door een geometrisch en optisch dikke, ruwweg toroïdale structuur van gas en stof, de zogenaamde stoftorus. Deze stoftorus absorbeert de invallende straling zeer efficiënt en zet deze om naar infraroodstraling. Naast deze componenten bevindt zich ook nog een gascomponent met een lagere dichtheid en rotatiesnelheid, met een ruimtelijke schaal gelijkaardig of groter dan de stoftorus. Dit gas kan worden waargenomen wanneer het wordt opgelicht door de kegel van ioniserende straling die wordt uitgezonden binnen de torus. Het is een bron van nauwe emissielijnen en is dan ook

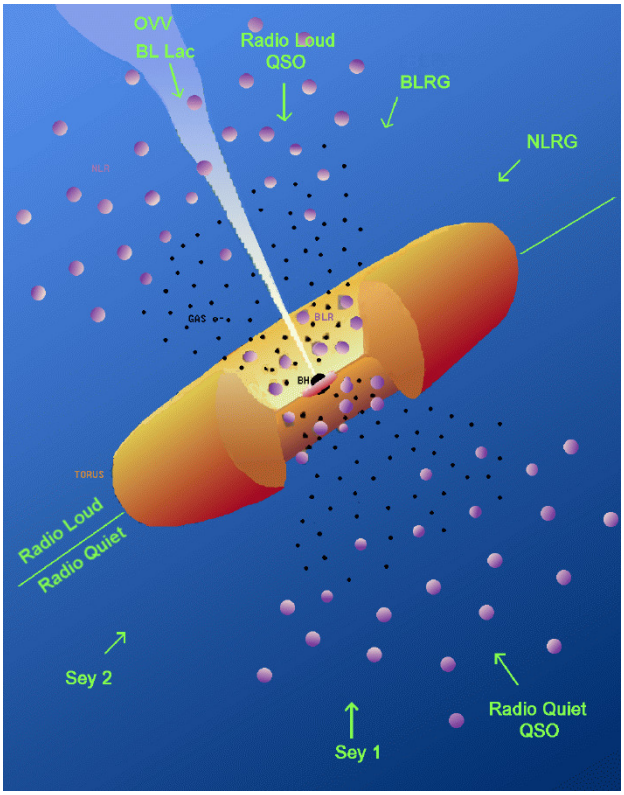

Figuur 5 Het standaard unificatiemodel voor AGNs. Afhankelijk van de oriëntatie, zal een waarnemer verschillende gebieden van de AGN kunnen zien en worden intrinsiek identieke objecten waargenomen als verschillende types van AGNs. © M. Polletta, naar (Urry & Padovani, 1995).

gekend als het nauwelijnengebied. Het bredelijnengebied en het thermische continuüm kunnen enkel worden waargenomen wanneer de torus vrijwel loodrecht op de gezichtslijn staat (d.w.z. in vooraanzicht); zulke systemen worden aangeduid als type 1 AGNs. Wanneer we hetzelfde systeem zouden zien in zijaanzicht, blokkeert de stoftorus de straling van de accretieschijf en het bredelijnengebied. In dit geval zijn de UV en optische continuümstraling en de brede emissielijnen niet waarneembaar, en zien we een type 2 AGN. Als een jet van materie, loodrecht op de accretieschijf, aanwezig is en we kijken recht in deze jet, dan zien we een krachtig, niet-thermisch, gepolariseerd en sterk variabel continuüm. Voor een uitgebreide bespreking van de verschillende types van AGNs verwijzen we naar Antonucci (2012).

In sommige klassen van AGNs kunnen de massa's van de supermassieve zwarte gaten onmiddellijk worden geschat (Dibai, 1977); dit is belangrijk aangezien AGNs momenteel de enige methode zijn om de evolutie van supermassieve zwarte gaten op kosmische tijdschalen te bestuderen. Bovendien zijn de helderste AGNs de lichtkrachtigste quasi-stabiele compacte stralingsbronnen in het heelal, waardoor we hun evolutie kunnen traceren tot op zeer hoge roodverschuiving. Om de groei van supermassieve zwarte gaten in functie van de kosmische tijd en het verband tussen supermassieve zwarte gaten en hun gastgalaxieën te begrijpen, moeten we eerst goed begrijpen hoe AGNs zelf zijn opgebouwd. We moeten het standaardmodel dat hierboven

is geschetst testen; in het bijzonder moeten we een verklaring zoeken voor waarnemingen die dit model momenteel klaarblijkelijk tegenspreken, en zo nodig het standaardmodel verfijnen en bijstellen.

Opzet van dit doctoraat Het doel van deze doctoraatsscriptie is een stap voorwaarts te zetten naar een beter begrip van de structuur van AGNs, in bet bijzonder van de stoftorus. Deze stoftorus heeft een belangrijk effect op de manier waarop AGNs zich vertonen aan de waarnemer. Hoewel de torus een vitaal onderdeel is van het standaardmodel, is ons begrip ervan ondermaats en zijn er nog vele onopgeloste problemen. Een eerste probleem is de intensiteit en de vorm van waargenomen lijnprofielen van silicaten op 10 en 18 μm. Deze lijnprofielen geven een unieke kijk op de verdeling en chemische samenstelling van het stof in de torus, maar de waarnemingen komen niet overeen met de theoretische verwachtingen. Een tweede probleem dat in verschillende werken is vermeld is het tekort aan straling in het nabije infrarood in state-of-the-art modellen voor de stoftorus, in vergelijking met de waargenomen spectrale energieverdeling van AGNs. Verdere open vragen betreffen de oorsprong en vorming van de stoftorus en het fysische proces dat ervoor zorgt dat de vereiste schaalhoogte van de torus behouden blijft. Het voornaamste doel van deze thesis is de ontwikkeling van een nieuw model voor de stoftorus in AGNs dat deze fenomenen kan verklaren. Daarnaast hebben we nog enkele andere, verwante fenomenen behandeld, zoals perturbaties in de accretieschijf. We hebben de modellen die we hebben ontwikkeld voor stoftorus en accretieschijf ook toegepast in een onderzoek naar de effecten van microlensing en de fotometrische variabiliteit van quasars. We presenteren hier een beknopte samenvatting van het onderzoek verricht in het kader van dit doctoraatswerk en geven de belangrijkste conclusies weer.

De stoftorus Wij hebben een nieuw, fysisch gemotiveerd model geïntroduceerd voor de stoftorus als een klonterig twee-fasig medium. Het bestaat uit klonters met een hoge dichtheid die zijn ingebed in een ijler medium. We hebben de 3D stralingsoverdrachtscode SKIRT (Baes et al., 2003, 2011) gebruikt om de spectrale energieverdelingen en beelden van de torus te genereren op verschillende golflengten. We hebben een grote set van modellen berekend met verschillende waarden voor de belangrijkste parameters, voor elk van deze modellen de eigenschappen van de infraroodemissie geanalyseerd, en deze vergeleken met de eigenschappen van gelijkaardige modellen met enkel klonters, of volledig zonder klonters (t.t.z. modellen met een *smoothe* verdeling). De voornaamste resultaten van deze analyse zijn de volgende (zie Hoofdstuk 2; Stalevski et al., 2011, 2012a; Stalevski, 2012c):

(i) De vorm en de sterkte van de emissie in het nabije en mid-infrarood worden bepaald door de toestand van het stof in de binnenste regionen van de torus: modellen die enkel verschillen in een verschillende random verdeling van klonters kunnen sterk verschillende spectrale energieverdelingen opleveren.

(ii) De ruimtelijke verdeling van het stof, de optische diepte, de grootte van de klonters en de feitelijke ruimtelijke verdeling van de klonters in de binnenste gebieden van de torus hebben allen een impact op het waargenomen lijnprofiel van silicaten op 10 μm. Deze silicaatlijn wordt op natuurlijke wijze onderdrukt in modellen met klonters, maar ook modellen met een smoothe verdeling van stof kunnen sterk verschillende sterktes van de 10 μm lijn genereren.

(iii) Het diffuse stof tussen de klonters kan een belangrijke bijdrage leveren aan de emissie van de torus in het nabije infrarood. Ons model met twee fases biedt zo een natuurlijke oplossing voor het probleem dat al vaak is aangekaart, namelijk dat modellen met enkel klonters een nabij-infrarood deficiet vertonen ten opzichte van waargenomen spectrale energieverdelingen van AGNs.

Het verschil in de spectrale energieverdeling in het nabije en mid-infrarood tussen een twee-fasig model, een model met enkel klonters en een smooth model is geïllustreerd in Fig. 6.

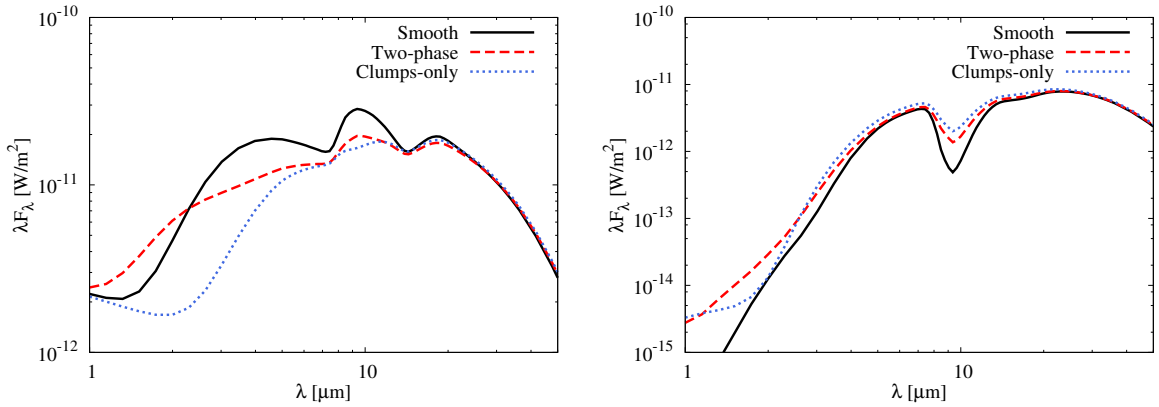

Figuur 6 De spectrale energieverdeling in het nabije en verre infrarood voor een model met typische waarden voor de parameters. Alle drie modellen zijn identiek, behalve the structuur van de stoftorus: de drie lijnen in elk paneel corresponderen met het smoothe model, het twee-fasige model en het model met enkel klonters. Het linkse paneel correspondeert met vooraanzicht (type 1 AGN), het rechtse paneel met zijaanzicht (type 2 AGN).

De invloed van microlensing Gravitationeel gelensde systemen met meervoudige beeldvorming vormen zijn uiterst handig om de grootte en de structuur van zowel de lens als de gelensde achtergrondbron te bestuderen. In een aantal gelensde systemen waarin een quasar de achtergrondbron is, blijkt de verhouding van de fluxen van de verschillende beelden van de quasar af te wijken van de verhouding die wordt voorspeld door eenvoudige lensmodellen. Microlensing door sterren in de lensgalaxie zou hierbij een rol kunnen spelen. Wanneer we deze anomalie willen begrijpen, is het belangrijk om de echte fluxverhouding van de beelden te kennen, zonder de bijdrage van microlensing. In principe kan dit gerealiseerd worden door te kijken naar

gebieden van de quasar die emissielijnen, infraroodstraling or radiostraling uitzenden, aangezien deze gebieden groot genoeg zijn om ongevoelig te zijn voor de effecten van microlensing. Tot nu toe heeft geen enkel werk in de literatuur echter een realistisch torusmodel in rekening gebracht in de studie van de effecten van microlensing. Wij hebben onze twee-fasige modellen voor stoftori gebruikt als een model, daarvan magnificatiekaarten gemaakt, en daarmee microlensing door sterren in de gastgalaxie gesimuleerd. Het doel hiervan is om te onderzoeken of microlensing de infraroodstraling van quasars kan beïnvloeden. Uit deze studie hebben we de volgende conclusies kunnen trekken (zie Hoofdstuk 3; Stalevski et al., 2012b):

(i) Ondanks hun aanzienlijke dimensie, kunnen de stoftori van AGNs in sommige gevallen sterk worden versterkt door microlensing. Aangezien de grootte van de torus golflengte-afhankelijk is, hangt ook de amplitude van de magnificatie sterk af van de golflengte (zie figuur 7). De magnificatie is het grootst in het nabije infrarood, zwakt sterk af naar het mid-infrarood toe, en blijft dan ongeveer constant in het verre-infrarood gedeelte van de spectrale energieverdeling.

(ii) Aangezien microlensing gevoelig is aan de grootte van de bron, spelen de parameters die de geometrie en de schijnbare grootte van de torus bepalen een heel belangrijke rol. Tori met een dimensie kleiner dan ongeveer 10 pc kunnen aanzienlijk sterker onderhevig zijn aan microlensing.

(iii) De geschatte tijdsschaal van microlensing events met een grote magnificatie, gemeten als de tijdsspanne tussen het begin en de piek van het event, variëren van enkele tientallen tot verschillende honderden jaren.

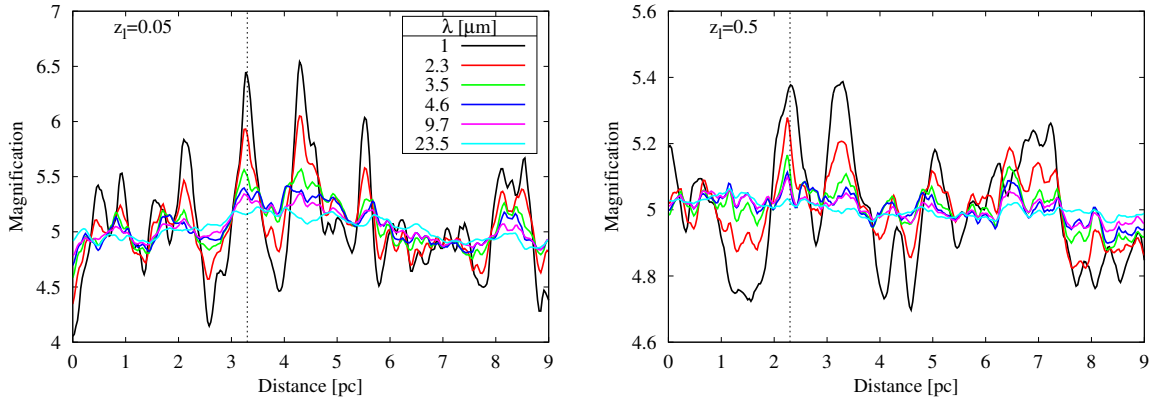

Figuur 7 Gesimuleerde microlensing lichtkrommen voor verschillende golflengten (aangegeven in de legende), voor een gravitationele lens op een roodverschuiving van 0.05 (links) en 0.5 (rechts). Merk op dat het vertikale bereik van beide figuren verschillend is.

Aangezien de tijdsschalen voor microlensing events zo groot zijn, is het moeilijk om microlensing te gebruiken als een praktisch hulpmiddel om de eigenschappen van stoftori rond AGN te bepalen, zoals dat wel het geval is bij de accretieschijven van AGN. De resultaten van onze

studie zijn echter wel van belang voor het interpreteren van de anomalie in de fluxverhouding van gelensde quasars met meervoudige beeldvorming in verschillende golflengtegebieden. We hebben aangetoond dat de infraroodstraling van stoftori wel degelijk onderhevig kan zijn aan microlensing, en dus een minder betrouwbare maatstaf voor de intrinsieke fluxverhouding van meervoudige beelden.

Perturbaties in de accretieschijf AGNs vertonen vaak een variabiliteit in hun UV en optische emissie, wat wijst op een variabiliteit in de emissie van de accretieschijf. Een aantal fysische overwegingen suggereren dat deze variabiliteit sterk niet-axiaal-symmetrisch moet zijn. Als zogenaamde off-axis variabiliteiten belangrijk zijn in AGN accretieschijven, dan heeft dit belangrijke gevolgen voor de zogenaamde reverberatiemethode die gebruikt wordt om de structuur van AGNs te onderzoeken, en voor de zoektocht naar binaire supermassieve zwarte gaten. Wij hebben zulke off-axis perturbaties in de emissiviteitsverdeling van AGNs gemodelleerd door middel van een heldere vlek in de accretieschijf. We hebben dit model toegepast op de waargenomen Hβ lijnprofielen van de quasar 3C 390.3. Uit dit onderzoek konden we de volgende besluiten trekken (zie Hoofdstuk 4; Jovanović et al., 2010; Stalevski et al., 2010):

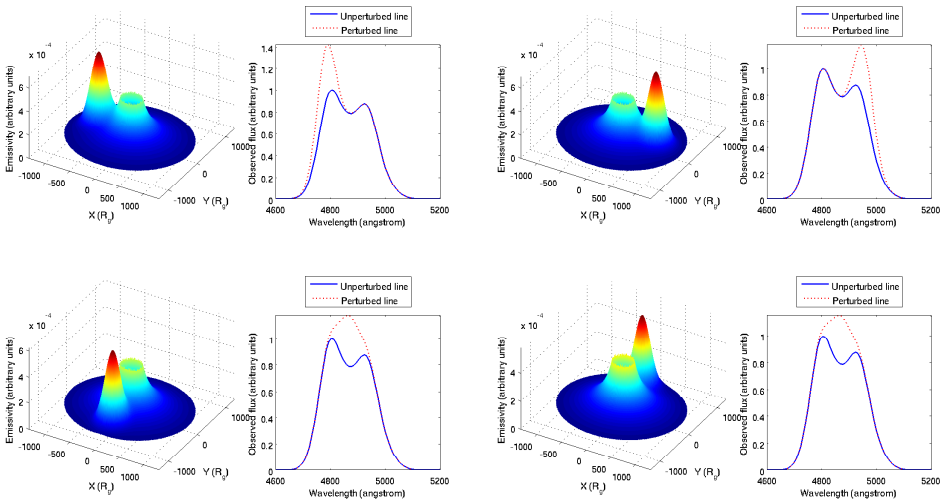

Figuur 8 Illustratie van de verstoorde emissiviteit van een accretieschijf rond een AGN, gemodelleerd als een heldere vlek, en de daarbij horende verstoorde (stippellijn) en onverstoorde (volle lijn) Hβ lijnprofielen. Afhankelijk van de positie van de heldere vlek, wordt één van de twee vleugels of het centrum van de lijn aangetast.

(i) Het model waarbij we de emissiviteitsperturbaties als een heldere vlek in de accretieschijf voorstellen kan met succes de verschillende waargenomen vormen en de variabiliteit van dubbel gepiekte lijnprofielen verklaren (zie figuur 8).

(ii) Met dit model zijn we erin geslaagd om de waargenomen variaties van het Hβ lijnprofiel van 3C 390.3 te modelleren en reproduceren, inclusief de twee grote uitbarstingen die zijn

waargenomen tijdens de periode waarbinnen we de data hebben geanalyseerd.

(iii) Onze resultaten ondersteunen de hypothese dat perturbaties in de emissiviteit van de accretieschijf veroorzaakt worden door fragmenten van spiraalarmen in de schijf.

Fotocentrische variabiliteit van quasars We hebben de nieuw ontwikkelde modellen voor de stoftorus en de verstoorde accretieschijf rond AGNs toegepast om de veranderlijkheid van het fotometrische centrum van quasars te bestuderen. Het fotocentrum kan immers worden beïnvloed door een uitbarsting in de lichtkracht van de accretieschijf of veranderingen in de structuur van de torus, en dit heeft mogelijk gevolgen voor de toekomstige Gaia missie. Gaia is een globale astrometrische interferometrische missie die als doel heeft om met hoge astrometrische nauwkeurigheid de positie van meer dan een miljard objecten in de ruimte te meten. Naar schatting zullen daarbij 500 000 quasars zijn. Deze quasars zullen worden aangewend om een nauwmazig optisch referentiekader aan de hemel te construeren. Wij hebben perturbaties in de accretieschijf en veranderingen in het stralingspatroon door verstrooiing aan stofdeeltjes in de torus beschouwd als mogelijke oorzaken voor fotocentrische variabiliteit. We hebben ingeschat in welke mate deze effecten kunnen bijdragen aan de variabiliteit van het fotocenter van quasars, en of deze effecten kunnen worden waargenomen met Gaia. Dit onderzoek leidde tot de volgende conclusies (zie Hoofdstuk 5; Popović et al., 2012:

(i) Perturbaties in de accretieschijf kunnen een verschuiving van het fotocenter teweegbrengen, en het is goed mogelijk dat we dit effect zullen kunnen waarnemen met Gaia. De verwachte maximale verschuiving, die wordt gerealiseerd door een heldere vlek aan de rand van de accretieschijf, bedraagt van de orde van enkele milliboogseconden.

(ii) Een fotocentrische verschuiving kan worden veroorzaakt door veranderingen in de structuur van de stoftorus als gevolg van verschillende belichtingspatronen van deze torus als deze de centrale bron verduistert. De maximale verschuiving kan verschillende milliboogseconden bedragen, en dit effect kan ook worden waargenomen met Gaia.

(iii) De waargenomen fotocentrische variabiliteit van twee quasars kan niet worden verklaard door variaties in hun binnenste structuur (d.w.z. van de accretieschijf en de stoftorus). Het blijkt dat de waargenomen fotocentrische variabiliteit goed verklaard kan worden door een scenario met twee variabele bronnen in het centrum van deze systemen. In samenspel met de complexe vorm van de brede lijnen, is dit een indicatie dat deze twee systemen goede kandidaten zijn voor galaxieën met een binair supermassief zwart gat.

Toekomstig werk Het onderzoek uitgevoerd in het kader van dit doctoraatsproefschrift maakt deel uit van een breder onderzoekskader, dat op verschillende manieren zal worden verdergezet. Wij zullen ons werk omtrent het modelleren van de stoftorus rond AGN verderzetten en uitbreiden met een vernieuwde versie van de SKIRT code. Ingewikkelder verdelingen en geometrieën

voor het stof in de torus, zoals deze die worden gegenereerd in numerieke hydrodynamische simulaties, zullen worden beschouwd. We zullen ook de uitgevoerde studie over microlensing uitbreiden door ook de effecten van millilensingen en sterke lensing in rekening te brengen, wat hopelijk tot een beter begrip van de anomalie in de fluxverhouding van gelensde quasars zal leiden.

1 Introduction

1.1 The phenomena of active galactic nuclei

Nowadays it is widely accepted that every massive galaxy harbors a supermassive black hole (SMBH) at its center. A number of apparent correlations between SMBH mass and host galaxy structural and dynamical properties have been observed. The correlation between the masses of SMBHs and their host galactic bulges suggests a link between their growth (Kormendy & Richstone, 1995; Kormendy & Gebhardt, 2001). The growth of SMBHs and the relationship between them and their host galaxies is one of the most vigorous areas of research in astrophysics, with about 200 papers per year. Active galactic nucleus (AGN) represents a phase in the life of a galaxy, during which the SMBH growth is directly observable. The term AGN encompasses a variety of energetic phenomena in galactic centers, powered by SMBHs accreting matter at a relatively high rate.

The radiation coming from AGNs originates in the conversion of gravitational potential energy into thermal energy as matter spirals towards the SMBH in an accretion disk (Lynden-Bell, 1969). Their luminosity can be up to 10000 greater than the total luminosity of a normal galaxy. The radiated AGN continuum covers a broad range of spectrum, from the X to radio domain, it is partially polarized and variable in time. Radiation from the central engine is ionizing the surrounding medium, creating conditions for the strong emission line spectrum, superimposed on the continuum. Sometimes AGN spectra are showing absorption lines as well. These could originate in the AGN itself, or from the host galaxy or the intergalactic medium (e.g. Ly α forest). Sometimes, highly collimated and fast outflows ("jets") emerge perpendicular to the accretion disk.

Figure 1.1 Artist's impression of an AGN – a supermassive black hole surrounded by an accretion disk and enshrouded in a dusty doughnut-shaped torus. Credit: ESO/M. Kornmesser.

The masses of SMBHs can be readily estimated in some types of AGN, (Dibai, 1977) and AGNs are currently our only way of studying the evolution of SMBHs over cosmic time. Furthermore, the brightest AGNs are the most luminous quasi-steady compact sources of radiation in the universe and hence they are valuable probes of cosmic evolution up to very high redshifts.

In order to understand black hole growth across cosmic time and the connection between galaxies and black holes, we need to understand how AGNs work. We need to test the basic picture outlined above and, in particular, to be able to explain observations which presently challenge this picture and might force modifications of it. A beautiful artist's impression of an AGN is shown in Fig, 1.1.

1.1.1 Classification of AGNs

According to the properties of their spectra, AGNs are classified into Seyfert galaxies of type 1 and 2, quasars of type 1 and 2, blazars, LINERs, radio-galaxies with narrow lines and radio galaxies with broad lines (Antonucci, 2012).

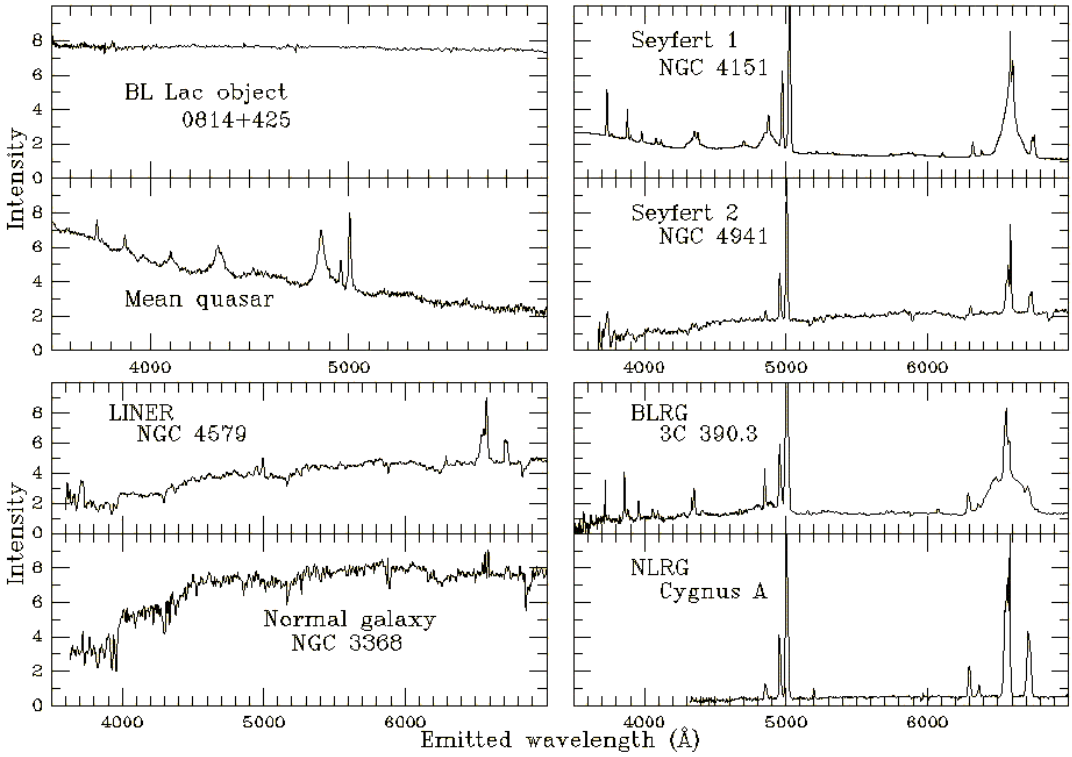

Figure 1.2 Characteristic spectra of different AGN types. Credit: W. C. Keel, `http://astronomy.ua.edu/keel/agn/spectra.html`

Seyfert galaxies This class of AGN are named after Carl Keenan Seyfert, who first identified the class (Seyfert, 1943). Seyfert 1 galaxies are showing both broad and narrow emission lines

in their spectra. Their absolute magnitudes are $M_{bol} \leqslant -21$. Seyfert 2 galaxies have only narrow emission lines in their spectra. They are usually of lower brightness ($M_{bol} \leqslant -20$) and their continuum is usually weaker than in Seyfert 1s. Depending on the strength ratios between broad and narrow lines, there are several intermediate types: Seyfert 1.5, 1.8, 1.9 (Osterbrock, 1989; Osterbrock & Ferrland, 2006).

Quasars Quasars are similar to Seyfert galaxies, but with much higher luminosities. Historically, the term *quasar* was associated with 'quasi-stellar radio sources' before their exact nature was known (Schmidt, 1963). Later on it was found that not more than 10% quasars have strong radio emission (are 'radio-loud'), so the term QSO (quasi-stellar object) was coined to refer to both the 'radio-loud' and the 'radio-quiet' objects. However, today the terms 'quasar' and 'QSO' are used virtually interchangeably, noting explicitly whether it is radio-loud or radio-quiet if needed (see Antonucci, 2012, for further discussion on the radio-loud and -quiet AGNs). Similarly as in Seyfert galaxies, we also distinguish two types of quasars: type 1 quasars, with both broad and narrow emission lines, and type 2 quasars, with narrow lines only. Type 2 quasars are only recently discovered and although there are many candidates, there are still only a few confirmed objects in this class (see Urrutia et al., 2012, and references therein). Owing to their extremely high brightness ($M_{bol} \leqslant -23$), the quasars can be observed at very high redshifts (to date $z = 7.085$, Mortlock et al., 2011)).

Blazars Blazars make up only a few percent of the entire AGN population. Two type of objects are classified as blazars: BL Lac objects (Schmitt, 1968) and Optically Violently Variable quasars - OVVs. BL Lac objects are characterized by a strong continuum and very weak or absent both emission and absorption lines. These are radio-loud objects, with strong, mostly non-thermal, highly polarized radiation, varying rapidly ($\sim$ 1 day) with large amplitudes. OVVs are similar to BL Lac objects, with the difference that their spectra are showing strong broad emission lines (Antonucci, 2012).

LINERs LINERs are the least luminous and the most common AGNs. Approximately one-third of all nearby galaxies may be classified as LINER galaxies (Ho et al., 1997). Most of these objects are assumed to have a nucleus similar to those in Seyfert galaxies, but with much lower luminosities. The narrow line spectrum of LINERs is clearly distinguished from that of Seyfert galaxies, in having a much lower degree of ionization. Their spectra typically include line emission from weakly ionized atoms, while line emission from strongly ionized atoms is relatively weak. Hence the name LINERs – Low-Ionization Nuclear Emission Line Regions. It is believed that such properties of LINERs are consequence of low accretion rate compared to other types of AGN. However, the exact nature of LINERs is still a matter of debate. Some authors advocate that LINER emission is powered by star forming regions (Ho et al., 1993).

Radio galaxies Radio galaxies are a class of active galaxies that are very strong radio sources (see Antonucci, 2012, and references therein). In these objects, the luminosity at radio wavelengths is dominated by the contribution from the material ejected perpendicular to the accretion disk – jets and the lobes they inflate. They are split in two groups, based on the properties of their optical spectra: Broad Line Radio-Galaxies (BLRGs) and Narrow Line Radio-galaxies (NLRGs). Radio galaxies, together with radio-loud quasars and blazars are referred to as the radio-loud family of AGNs; Seyfert galaxies, radio-quiet quasars and LINERs are radio-quiet. The main difference between these two classes is the presence/absence of the strong extended radio emission. Low-power radio galaxies are a plausible parent population for BL Lac objects, i.e. seen at small angles, they appear as BL Lac (Browne, 1983).

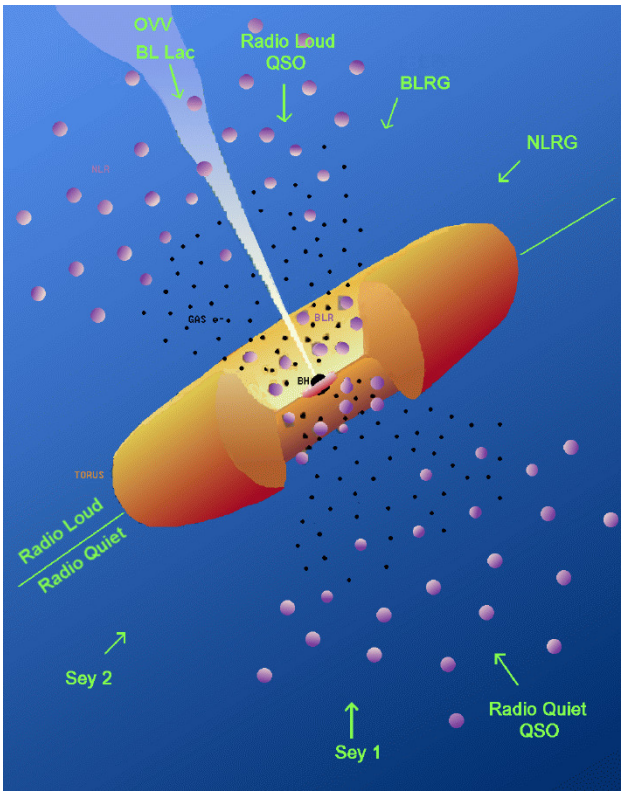

Figure 1.3 The standard AGN unification scheme. Depending on the orientation, an observer will see different emitting regions and thus, an intrinsically same objects would appear to him as a different type of AGN (M. Polletta, adapted from Urry & Padovani, 1995).

The AGN terminology can be confusing, since the distinctions between different types of AGNs sometimes reflect historical differences in how objects were discovered or initially classified, rather than real physical differences. For an in-depth discussion and overview of different AGN types, see review by Antonucci (2012).

Characteristic optical spectra of various kinds of AGNs are presented in Fig. 1.2. The BL Lac object has a virtually featureless spectrum, with a strong non-thermal continuum. In the spectrum of the Seyfert 1 galaxy, the mean quasar and the BLRG, both broad and narrow emission

lines are present, while the Seyfert 2 galaxy, the LINER and the NLRG have only narrow lines. In the bottom left panel, the spectrum of a normal galaxy is given for comparison. Its spectrum is characterized mostly by absorption lines from the atmospheres of individual stars, with weak emission lines from gas in star-forming regions ionized by hot young stars.

1.1.2 AGN unification model

Since the discovery by Keel (1980) that the orientation of Seyfert 1 galaxies is not random, it has been recognized that the appearance of an AGN in the optical and UV depends on the viewing angle. This has led to the picture of "orientation unification" (see Antonucci, 1993; Urry & Padovani, 1995) where the structure of AGNs is believed to be basically similar but what we see is a strong function of orientation. In this unified model, the central black hole is surrounded by a geometrically-thin and optically-thick accretion disk which is the source of the strong X-ray emission and UV/optical continuum (see Jovanović, 2012, and references therein). Above and below the disk is the broad-line region (BLR), a flattened distribution of turbulent, rapidly-moving and dense emission-line gas orbiting the black hole (see Gaskell, 2009, for a review). Both the accretion disk and the BLR are surrounded by a geometrically- and optically-thick, roughly toroidal structure of dust and gas (the "dusty torus "). In addition to these components, there is lower density, more slowly moving gas present on a scale similar to or significantly larger than that of the torus. This gas can be seen when it is illuminated by the cone of ionizing radiation emanating from inside the torus. It is a source of narrow emission lines and thus is know as the "narrow-line region" (NLR). The broad emission lines and the thermal continuum emission can only be seen when the torus is close to face-on and thus, such an object appears as a type 1 active galaxy. For close to edge-on orientations, the dusty torus blocks the radiation coming from the accretion disk and the BLR. In this case, the UV/optical bump and broad emission lines are absent in the observed spectrum and the object appears as a type 2 active galaxy. If a jet of matter, ejected perpendicular to the accretion disk is present, then viewing such an object along the jet would exhibit strong non-thermal, polarized and rapidly variable continuum, and thus it would be classified as a blazar. For the comprehensive overview of AGN phenomenon, see Krolik (1998).

However, rather than being separate isolated regions, as is commonly depicted in simplified cartoons of the unified model of AGNs (Fig. 1.3), the torus, broad-line region and accretion disk are intimately connected. The BLR is accreting material from the torus that has passed within the dust sublimation radius (Gaskell et al., 2007; Elitzur, 2007; Gaskell, 2009). The dust in the torus (and also, possibly, dust found in the outermost parts of the BLR) can affect BLR line profiles due to extinction and scattering. Furthermore, in recent studies it was found that, in contradiction with the simplest unification model, the classification of a Seyfert galaxy as a type 1 or type 2 depends more on the intrinsic properties of the material obscuring the central regions,

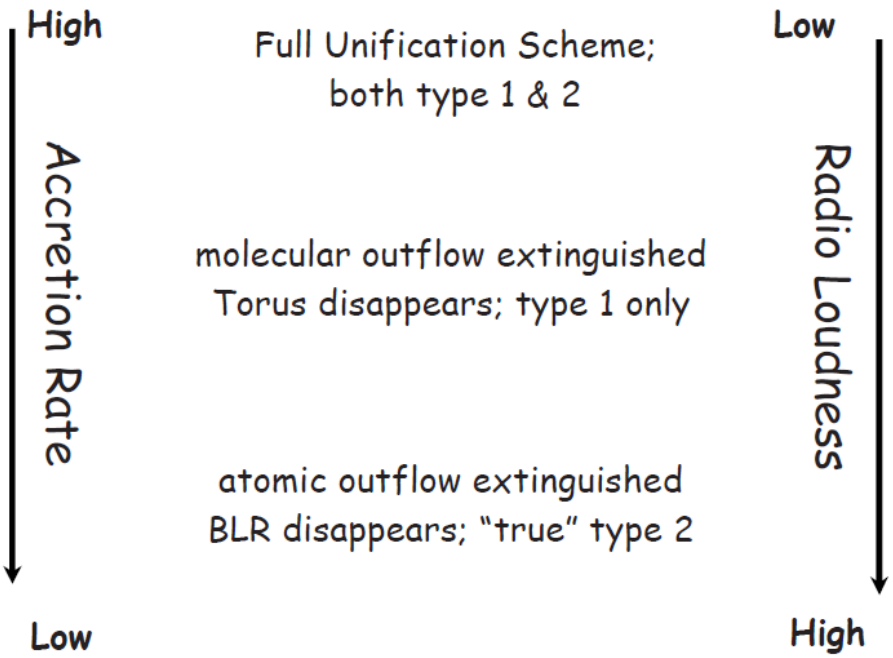

Figure 1.4 Scheme for AGN evolution with decreasing accretion rate (Elitzur, 2007).

rather than on its mere inclination towards an observer (Ramos Almeida et al., 2011; Ricci et al., 2011). In one possible scenario of a more realistic formulation of the unification scheme (Elitzur, 2007), the BLR and the dusty torus are, respectively, the inner and outer segments, across the dust sublimation radius, of a continuous cloud distribution. Obscuration of the X-ray continuum comes mostly from the inner, BLR clouds. All clouds are embedded in a disk wind, whose mass outflow rate is diminishing as the accretion rate (i.e. AGN luminosity) is decreasing. The torus disappears at lower luminosities because mass accretion can no longer sustain the required cloud outflow rate. With further luminosity decrease, the BLR disappears as well. This evolutionary scheme is sketched in Fig. 1.4.

As noted in the previous section, the dusty torus has a major effect on the appearance of an AGN. The dust surrounding the central regions of the AGN absorbs radiation from the accretion disk and re-emits it in the infrared (IR). Observations of the mid- to far-IR bump and of the silicate feature at 10 μm in the spectral energy distribution (SED) of AGNs are consistent with this picture. In type 1 sources, hot dust in the inner regions can be seen directly and the feature is expected to be detected in emission. Recent mid-infrared observations obtained with the *Spitzer* satellite confirm the silicate emission feature in type 1 AGNs (Siebenmorgen et al., 2005; Hao et al., 2005). In type 2 objects, the dust feature is observed in absorption (e.g., Jaffe et al., 2004) due to obscuration by the cold dust. Interferometric observations provide additional evidence for the presence of the dusty torus. Using speckle interferometry, the nucleus of NGC 1068 was successfully resolved in the *K*-band (Wittkowski et al., 1998) and in the *H*-band (Weigelt et al., 2004). This resolved core is interpreted as dust close to the sublimation radius. Tristram et al. (2007) reported VLTI interferometric observations with strong evidence of a parsec scale dust structure in the Circinus galaxy. Kishimoto et al. (2011) reported indications of a partial resolution of the dust sublimation region in several type 1 AGNs using the Keck interferometer. Observed polarized nuclear emission in type 2 sources, scattered by electrons and tenuous dust (Antonucci & Miller, 1985; Pier et al., 1994; Packham et al., 1997), supports the unification model. It proves that an active galactic nucleus is present, even though no direct emission from the accretion disk is observed. The toroidal geometry also explains several other observables such as, the presence of ionizing cones (Pogge, 1988, 1989; Tadhunter & Tsvetanov, 1989) and high hydrogen column densities in the X-ray domain, usually associated with type 2 sources (e.g. Shi et al., 2006).

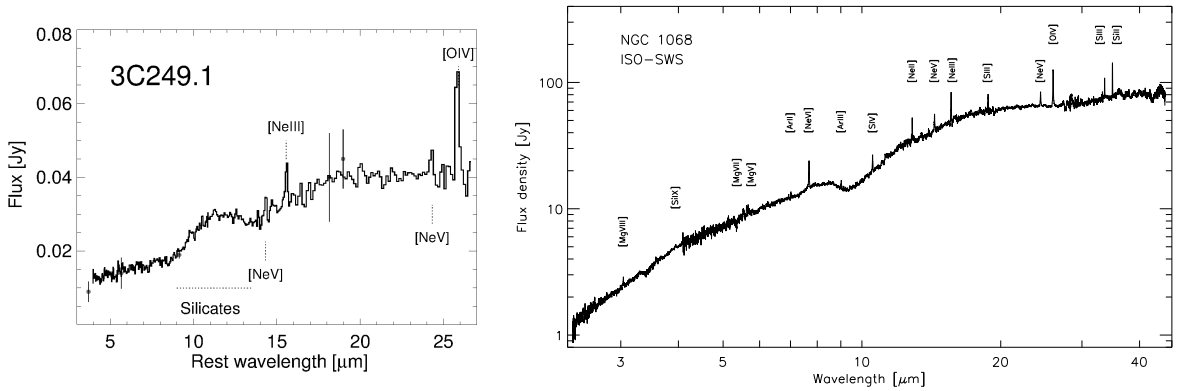

Figure 1.5 IR SEDs of two AGNs showing the 10 μm silicate feature in emission (left panel, Siebenmorgen et al., 2005) and absorption (right panel, Lutz et al., 2000).

There are, however, still many unresolved issues regarding the dusty torus. Among the most interesting ones are those related to the intensity and shape of the silicate features, at 10 and

18 μm, which represent a unique window into the dust distribution and chemical composition even in relatively distant quasars. Two issues are particularly puzzling, and are worth more investigation: the intensity of the feature as a function of the AGN type, and its shape. As for the intensity, this was one of the main reasons why clumpiness, opposed to a homogenous dust distribution, was advocated: a clumpy distribution of dust would naturally give rise to a less intense feature, both in emission and absorption. That the shape of the silicate feature was different from the theoretical expectations, had already been found from the very first detections (Siebenmorgen et al., 2005; Hao et al., 2005). Modeling this discrepancy has been attempted both with smooth (Fritz et al., 2006)) and clumpy (Nikutta et al., 2009) models, with poor results. Whether this different shape is to be attributed to the different chemical composition, different emissivity properties or to geometrical effects, is at present still completely unclear. Another common problem reported in a number of papers, is the lack of the near-IR emission when trying to apply state-of-the art clumpy models to the observed infrared SEDs of AGNs (Polletta et al., 2008; Mor et al., 2009; Ramos Almeida et al., 2009; Alonso-Herrero et al., 2011; Mor & Netzer, 2012; Deo et al., 2011). This issue could represent either a failure of the modeling or contamination by some other emission component. Although different solutions have been suggested in the literature, none of the studies so far have taken this into account to obtain consistent models.

The origin and formation of the torus (i.e., how material from the nuclear region of the galaxy enters the torus) is yet another unresolved question. The biggest theoretical challenge is the question how the required scale height of the torus is maintained. Both the ratios of type-1 (= face-on) and type-2 (= edge-on) AGNs (Maiolino & Rieke, 1995) and the amount of reprocessing in the IR (Maiolino et al., 2007) point to the scale height of the torus being luminosity dependent (the so-called "receding torus" Lawrence, 1991), but the reason for this is still unclear. We do not know whether the thickness of the torus is due to turbulent motion, or due to radiation pressure (see Wada, 2012). The covering factors of the BLR and torus are similar (Gaskell et al., 2007) and the BLR is certainly turbulent, but if the torus is turbulent then collisions between dust clouds must be inelastic. These questions are tightly related to the evolution of AGNs and related issues, such as, the disappearance of the torus at low Eddington ratios and the transition to "non-thermal" AGNs ("true" type-2 sources, without hidden BLR – see Antonucci (2012), Elitzur (2012) and references therein).

1.3 Gravitationally lensed quasars

Gravitational lensing is the phenomenon of light bending in the gravitational field of massive objects. The trajectories of photons from distant sources are perturbed by the inhomogeneous distribution of matter. Many sources appear to us slightly displaced and distorted in comparison with the way they would appear in a perfectly homogeneous and isotropic universe. This phenomenon is called weak gravitational lensing. Weak lensing shows up statistically as a preferred direction of stretching and orientation of background objects, so it can be detected only by statistically analyzing a large number of sources. Under some circumstances, the deflection caused by foreground mass overdensities such as galaxies, groups, and clusters is sufficiently large to create multiple images of a distant light source (Fig. 1.6). This phenomenon is called strong gravitational lensing. Depending on the mass of lensing object, strong lensing can produce different effects: multiple images in the case of galaxy lensing, giant arcs and large-separation lenses in the case of lensing by clusters of galaxies, and microlensing magnification in the case of lensing by stars. In the case of microlensing, the lensing object is a stellar-mass compact object (e.g. a normal star, a brown dwarf or a compact stellar remnant). Stellar mass microlenses also produce multiple images (Fig. 1.7). However, these micro-images are splitted only by microarcseconds, and therefore are not accessible to present-day instrumentation. But the change of magnification of images over time due to microlensing is observable. The perturbations of lensing effects introduced by substructure of a lens galaxy is referred to as millilensing.

Both strong and weak gravitational lensing have a wide range of applications, such as the detection of distant objects (Richard et al., 2011), constraining cosmological parameters (Oguri et al., 2012; Cao et al., 2012; Jovanović & Popovic, 2010), studies of dark and visible matter distribution (e.g. Massey et al., 2007; Zakharov et al., 2004), investigation of innermost regions of AGNs (see e.g. Jovanović et al., 2009c, and references therein), and the study of extrasolar planets, not only in our Galaxy, but even in nearby galaxies such as Andromeda and Magellanic Clouds (e.g. Ingrosso et al., 2009; Zakharov, 2009).

Gravitationally lensed quasars represent a particularly interesting case. In these systems, different lensing regimes can be present: multiple images of the quasar by a lens galaxy, microlensing magnification by stars in a lens galaxy, and millilensing due to cold dark matter (CDM) substructure in a lens galaxy. Lensed quasars with multiple images represent a powerful tool to study the structure of both the galaxy which acts as the lens and the background quasar. In a number of lensed systems in which a quasar is the source, the flux ratios between the lensed images deviate from those predicted by simple lens models (see e.g. Kochanek, 1991; Keeton et al., 2003; Goldberg et al., 2010). The fluxes, in different wavebands, can be contaminated by different effects such as microlensing by stars (e.g. Schneider & Wambsganss, 1990), millilensing by a massive structure in the lens galaxy (e.g. Mao & Schneider, 1998), dust extinction

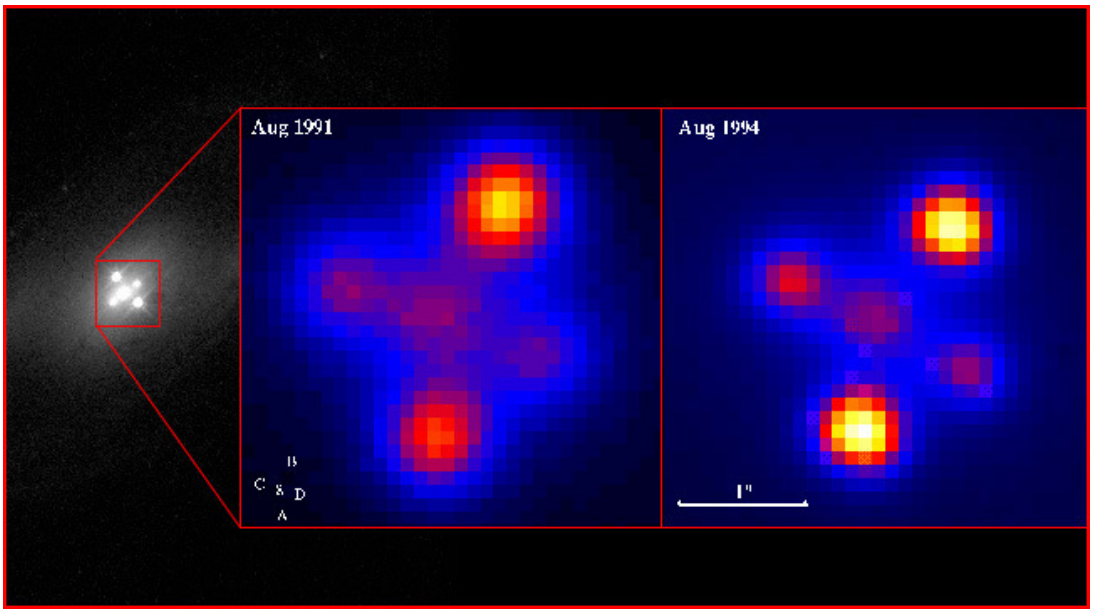

Figure 1.6 Quadruply imaged quasar Q2237+0305, also known as the "Einstein cross". The images in the two panels are taken three years apart; the noticable brightness change of the images relative to each other is due to microlensing (G. Lewis, M. Irwin).

(e.g. Elíasdóttir et al., 2006), and also by the time delay itself (e.g. Popović & Chartas, 2005). Consequently, the flux ratio anomaly observed in some lensed quasars can be caused by extinction and/or gravitational microlensing/millilensing (see e.g. Popović & Chartas, 2005; Yonehara et al., 2008).

The size of the source has a large effect on the fluctuations due to microlensing. As an extended source covers a larger area of a microlensing magnification pattern at any given time than a point source, its brightness varies less as it moves relative to the lens and observer (Mortonson et al., 2005). As a general rule, the variability of a lensed source is significantly affected by microlensing only if the source is smaller than the relevant microlensing length scale (Einstein ring radius – see section 3.2.1) (Courbin et al., 2002). Since the sizes of different emitting regions of quasars are wavelength-dependent, microlensing by the stars in the lens galaxy will lead to a wavelength-dependent magnification. The X-ray radiation is coming from a very compact region in the innermost part of the accretion disk, and therefore, it will be magnified more and its variations will be faster than for the radiation in the UV and optical bands, coming from outer, larger parts of the disk (Jovanović et al., 2008). Thus, although the phenomenon of gravitational lensing is achromatic, due to the complex structure of emission regions, "chromatic" effect may arise in a lensed quasar system (see e.g. Popović & Chartas, 2005; Popović et al., 2006; Jovanović et al., 2008; Mosquera et al., 2009, 2011). The "chromaticity" in lensing effect can be used to investigate both an unresolved structure of the innermost region of quasars (see e.g. Wyithe et al., 2002; Abajas et al., 2002; Popović et al., 2003, 2006; Bate et al., 2008; Mosquera et al., 2009; Dai et al., 2010; Blackburne et al., 2011; Garsden et al., 2011) and the structure

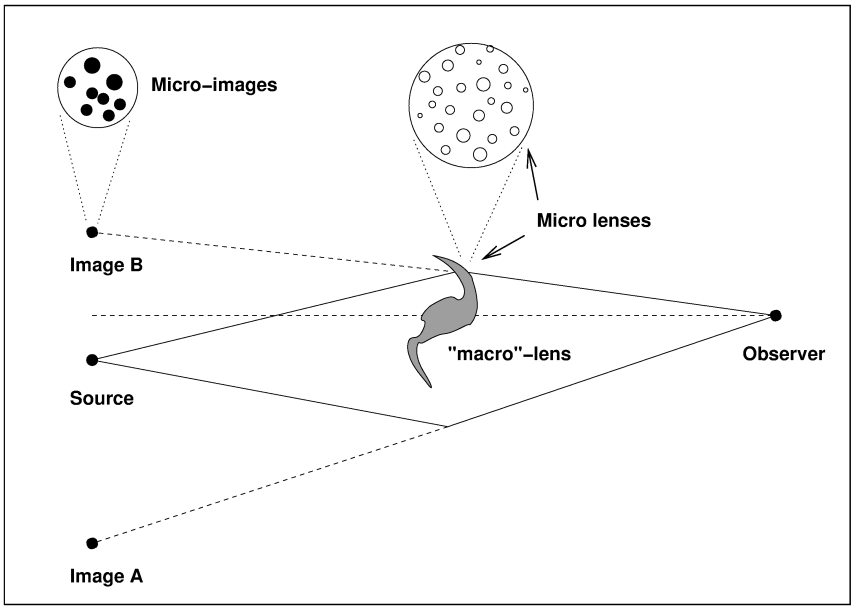

Figure 1.7 Schematic representation of microlensing by stars in a doubly imaged system. The unresolved stars in the lens galaxy are responsible for microlensing of one of the quasar images (Courbin et al., 2002).

of the lens galaxy (see e.g. Inoue & Chiba, 2005; Chiba et al., 2005; Xu et al., 2010). Moreover, comparing flux ratios at different wavelengths makes it possible to constrain the amount of micro- and milli-lensing present in the system, and the sizes of the perturbers (see e.g. Goldberg et al., 2010).

Since the X-ray and UV/optical radiation is coming from relatively compact regions (from several light days to a light month), the flux ratios in these waveband are sensitive to both microlensing by stars and millilensing by CDM substructure (see e.g. Metcalf & Madau, 2001; Zakharov et al., 2004; Popović & Chartas, 2005; Dobler & Keeton, 2006; Jovanović et al., 2008; Goldberg et al., 2010; Xu et al., 2010). On the other hand, the infrared emitting region of a quasar is assumed to be a toroidal structure of dust, with dimensions significantly larger than the projection of the Einstein radius of a microlens into the source plane. Therefore one would expect that the IR radiation of lensed quasars would only be affected by the relatively massive subhalos (millilensing) (see Inoue & Chiba, 2005; Chiba et al., 2005; Sluse et al., 2006; Yonehara et al., 2008; Minezaki et al., 2009; Xu et al., 2010; Fadely & Keeton, 2011). However, certain geometrical and physical properties of the dusty torus can conspire to allow non-negligible microlensing effects in even in the infrared domain.

1.4 The scope of this thesis

The aim of this thesis is to take a step forward towards a better understanding of the structure of AGNs. The main focus of the research reported in this thesis is the modeling and analysis of the dusty torus, with applications in studies of microlensing and photometric variability of quasars. In particular, we want to address the issues such as the intensity and shape of the silicate features, which represent a unique window into the dust distribution and chemical composition, and lack of near-IR emission when trying to apply the state-of-the art clumpy models to the observed IR SEDs of AGN. In order to make further advances, more detailed, physically-motivated models of dusty torus are needed. We introduce a new model of the dusty torus as a clumpy two-phase medium, with high-density clumps and low-density medium filling the space between them. We use a 3D Monte Carlo radiative transfer code to simulate SEDs and images of the torus at different wavelengths. We present a grid of models for different parameters, analyze the properties of IR emission and compare them to the properties of the corresponding sets of clumps-only models and models with a smooth dust distribution.

As noted in the previous section, microlensing by stars can be used to probe the size and structure of the different emitting regions of lensed quasars. Furthermore, when investigating the flux ratio anomaly of lensed quasar images, it is important to determine the true magnification ratios between the images, in the absence of microlensing. In principle, this could be done by looking at the emission-line, infrared, and radio-emitting regions of quasars, as they all should be large enough to safely disregard microlensing effects. However, none of the works presented in the literature so far has exploited a realistic torus model in microlensing studies. We use our two-phase models of the dusty torus as the source and generate magnification maps characteristic for lensed quasars to confirm whether, when investigating flux ratio anomaly in IR, one can safely disregard magnification due to the stars in the lens galaxy, or microlensing can contaminate flux ratios even in the IR.

Gaskell (2008) argued that, from physical considerations, the variability of the accretion disk has to be highly non-axisymmetric. He has proposed (Gaskell, 2010, 2011) that a wide range of AGN puzzles can be solved by non-axisymmetric variability. This represents a significant paradigm change from the normal assumption of axisymmetry. If off-axis variability is important, this has significant implications for using reverberation mapping to probe the structure of AGNs, and for searches for binary SMBHs. We model such non-axisymmetric emissivity perturbations of an AGN accretion disk, showing that it can explain variability of some double-peaked line profiles. The developed model is applied in the case of observed H_β line profiles of the quasar 3C 390.3.

Finally, we use both this non-axisymmetric accretion disk model and the dusty torus model to study variations of quasar photocenters, caused by an outburst of accretion disk luminosity

and changes in the dusty torus structure, in the context of the future Gaia mission. Gaia is a global astrometric interferometer mission that aims to determine high-precision astrometric parameters for one billion objects. It is foreseen that 500 000 quasars will be among these objects. These quasars will be used to construct a dense optical quasar-based celestial reference frame. We consider perturbations in the accretion disk and changes in the pattern of radiation scattered by the dust particles in the surrounding torus. We estimate how much these effects may contribute to the variability of the photocenter and the possibility of detecting this effect with Gaia mission.

This thesis is organized as follows:

In Chapter 2 we give an overview of the other works in literature on modeling of the dusty torus, present our new physically motivated model, and analyze and discuss properties of a grid of models we calculated. In Chapter 3 we use our dusty torus model to investigate microlensing effects in the case of lensed quasars in infrared. In Chapter 4 we present our model of off-axis emissivity perturbations of the accretion disk, and apply it in the case of observed line profiles of the quasar 3C 390.3. In Chapter 5 we present our study of variations of quasar photocenter due to perturbations in the accretion disk and changes in the structure of the dusty torus.

We used a flat cosmological model with the following parameters: $\Omega_{\mathrm{M}} = 0.27$, $\Omega_{\Lambda} = 0.73$ and $H_0 = 71$ km s^{-1} Mpc^{-1} (Jarosik et al., 2011).

2 The dusty torus as a clumpy two-phase medium

2.1 Introduction

As noted in Section 1.1.2, the AGN unification model requires a roughly toroidal structure of dust and gas that surrounds the central regions. In order to prevent the dust grains from being destroyed by the hot surrounding gas, Krolik & Begelman (1988) suggested that the dust in the torus is organized in a large number of optically thick clumps (Fig. 2.1). However, due to the difficulties in handling clumpy media and lack of computational power, early work was conducted by adopting a smooth dust distribution. Several authors explored different radial and vertical density profiles (Pier & Krolik, 1992, 1993; Granato & Danese, 1994; Efstathiou & Rowan-Robinson, 1995; van Bemmel & Dullemond, 2003; Schartmann et al., 2005; Fritz et al., 2006). The first effort of developing the formalism for the treatment of clumpy media was undertaken by Nenkova et al. (2002, 2008a, 2008b). They utilized a 1D radiative transfer code to compute the SED of a single irradiated clump. In a second step a statistical generalization is made to assemble the SED of the torus. They claim that only clumpy tori are able to reproduce the observed properties of the silicate feature. However, Dullemond & van Bemmel (2005) modeled the torus as a whole, using 2D radiative transfer calculations. They adopted a geometry with axial symmetry and modeled clumps in the form of rings around the polar axis. They made a direct comparison of models with clumps and corresponding smooth dust distributions and concluded that there is no evidence for a systematic suppression of the silicate emission feature in the clumpy models. Hönig et al. (2006), with an upgrade of their model in Hönig & Kishimoto (2010), adopted a similar method as Nenkova et al. (2002), but they employed a 2D radiative transfer code and took into account various illumination patterns of clumps. They reported that a suppression of the silicate emission feature strongly depends on the random distribution and density of the clumps in the innermost region. More recently, Schartmann et al. (2008) presented 3D radiative transfer models of clumpy tori. Their findings are in agreement with those by Hönig et al. (2006). On the other hand, Feltre et al. (2012), using the models developed by Fritz et al. (2006), found that a smooth distribution of dust is also capable of reproducing the observed variety of the silicate feature strength. A further study of the silicate feature and its properties, such as the unexpected appearance in emission in some type 2 objects and the apparent shifting toward long wavelengths in some objects, is presented in Nikutta et al. (2009).

A problem which the obscuring torus hypothesis faced from the beginning was formation of the dynamically stable structure and maintenance of the required scale-height. Krolik & Begelman (1988) presented a scenario according to which the scale-height is maintained through regular elastic collisions between the clumps (see also Beckert & Duschl, 2004). In the case of a continuous dust distribution, Pier & Krolik (1992), followed by Krolik (2007), suggested that radiation pressure within the torus may be enough to support the structure. Wada & Norman (2002), with model update in Wada et al. (2009) and (Wada, 2012), performed a 3D hydrody-

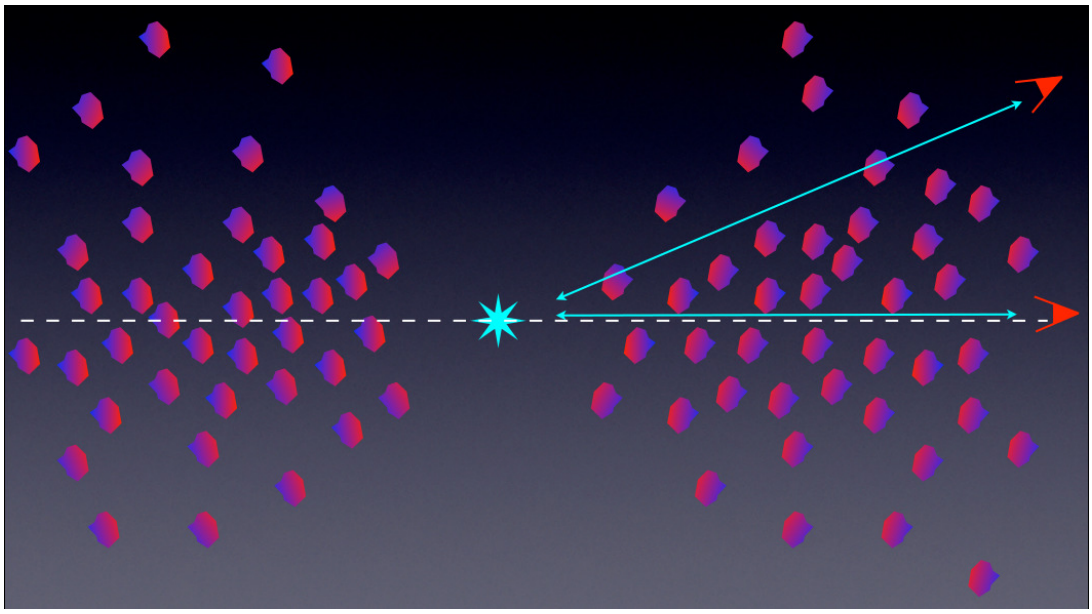

Figure 2.1 Schematic representation of clumpy torus model. An interesting consequence of clumpiness is that the difference between the type 1 and 2 objects is not truly an issue of orientation, but rather a matter of probability of directly viewing the central regions. Credit: Jacopo Fritz.

namical simulations, taking into account self-gravity of the gas, radiative cooling and heating due to supernovae. They found that such a turbulent medium would produce a multiphase filamentary (sponge-like) structure, rather then isolated clumps (see Fig. 2.2). A scenario where the effects of stellar feedback from a nuclear cluster play a major role is discussed in Schartmann et al. (2009).

In this chapter, we present our modeling of AGN dusty tori. We model the torus as the whole, using the 3D Monte Carlo radiative transfer code SKIRT. We take a step further toward a more realistic model by treating the dusty torus as a two-phase medium, with high density clumps and low density medium filling the space between them. We calculated SEDs and images of the torus for a grid of parameters. This approach allows us to, for each two-phase model, generate a clumps-only model (with dust distributed to the clumps exclusively, without any dust between them) and a smooth model with the same global physical parameters. Our aims are: (a) to investigate the influence of different parameters on model SEDs and their observable properties, (b) to put to a test reports that the observed SEDs in the mid-infrared domain unambiguously point to a clumpy structure of dusty tori; if that is indeed the case, a comparison of clumpy and smooth models should show a systematic difference of their observable properties, such as the strength of the silicate feature.

In this chapter, we first provide a general overview of the continuum radiative transfer problem and the code we used for modeling (Section 2.2). The details of our model are presented in Section 2.3. In Section 2.4 we discuss how different parameters affect modeled SEDs, analyze

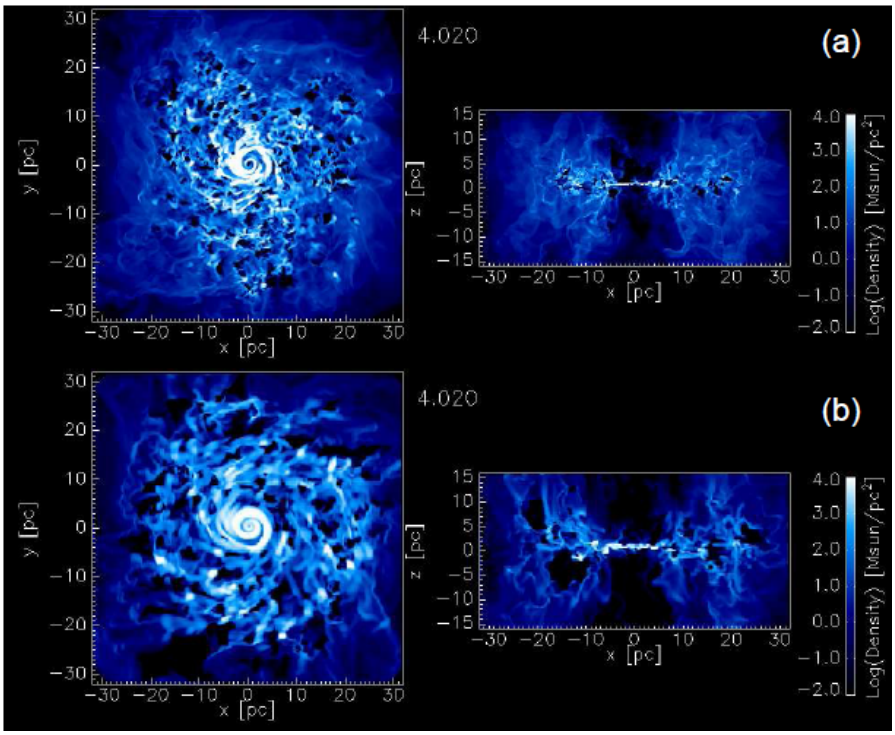

Figure 2.2 Face-on and edge-on views of cross sections of gas density distributions resulting from the hydrodynamical simulations by Wada et al. (2009). The resulting medium is not a collection of isolated clumps, but a multiphase filamentary structure.

their observable properties and compare two-phase, clumps-only and smooth models. Finally, in Section 2.5 we outline our conclusions. The results presented in this chapter have been published in Stalevski et al. (2011) and Stalevski et al. (2012a).

We have used the radiative transfer code SKIRT (Baes et al., 2003, 2011) for the modeling of AGN dusty tori. SKIRT is a 3D continuum radiative transfer code based on the Monte Carlo algorithm (Cashwell & Everett, 1959; Witt, 1977), initially developed to study the effect of dust absorption and scattering on the observed kinematics of dusty galaxies (Baes & Dejonghe, 2001, 2002; Baes et al., 2003). It has been extended with a module to self-consistently calculate the dust emission spectrum under the assumption of local thermal equilibrium – LTE (Baes et al., 2005a). This LTE version of SKIRT has been used to model the dust extinction and emission of galaxies and circumstellar disks (Baes et al., 2010; de Looze et al., 2010; Vidal & Baes, 2007). Recently, the code was adapted to include the emission from very small grains and polycyclic aromatic hydrocarbon molecules (Baes et al., 2011).

Similar to most modern Monte Carlo codes (e.g. Gordon et al., 2001; Wolf, 2003; Niccolini, Woitke, & Lopez, 2003; Bianchi, 2008), the SKIRT code contains many deterministic elements which makes the Monte Carlo technique orders of magnitude more efficient than the naive Monte Carlo recipe. These include the peeling-off technique (Yusef-Zadeh, Morris, & White, 1984), continuous absorption (Lucy, 1999; Niccolini, Woitke, & Lopez, 2003), forced scattering (Cashwell & Everett, 1959; Witt, 1977) and smart detectors (Baes, 2008). For the simulations presented in this thesis, we used the technique of frequency distribution adjustment presented by Bjorkman & Wood (2001) and critically discussed by Baes et al. (2005b). This technique ensures that at each moment during the simulation, the wavelength distribution from the photon packages emitted from the cell are in agreement with the cell's current temperature. The main advantage of this technique is that no iteration is necessary.

2.2.1 The continuum radiative transfer problem

The continuum radiative transfer equation we consider here describes how the radiation field varies as a result of interactions with a medium filled with sources and sinks (typically a multi-population dust medium). The physical processes we take into account are emission by sources and absorption, multiple anisotropic scattering and re-emission by dust grains. We consider a dusty medium consisting of N_{pop} populations of different dust species. Each population contains spherical dust grains of different radii a. The number of dust grains of population j of a particular size is characterized by a size distribution function $\mathrm{d}n_j = f(a)\mathrm{d}a$, which we define as the total number of dust grains per unit dust mass of type j with size between a and $a + \mathrm{d}a$. The absorption and scattering cross sections are denoted as $C^{\mathrm{abs}}_{\lambda,j}(a)$ and $C^{\mathrm{sca}}_{\lambda,j}(a)$. When we assume that the optical properties of the dust are independent of the location in the system, the general LTE radiative transfer equation can be written as

$$
\begin{aligned}
\frac{\mathrm{d}I_\lambda}{\mathrm{d}s}(\boldsymbol{r},\boldsymbol{k}) &= j^*_\lambda(\boldsymbol{r}) \\
&- \rho(\boldsymbol{r}) \sum_{j=1}^{N_{pop}} \int_{a_{min,j}}^{max,j} \frac{\mathrm{d}n_j}{\mathrm{d}a}(a)\, C^{\mathrm{abs}}_{\lambda,j}(a)\, I_\lambda(\boldsymbol{r},\boldsymbol{k})\, \mathrm{d}a \\
&- \rho(\boldsymbol{r}) \sum_{j=1}^{N_{pop}} \int_{a_{min,j}}^{max,j} \frac{\mathrm{d}n_j}{\mathrm{d}a}(a)\, C^{\mathrm{sca}}_{\lambda,j}(a)\, I_\lambda(\boldsymbol{r},\boldsymbol{k})\, \mathrm{d}a \\
&+ \rho(\boldsymbol{r}) \sum_{j=1}^{N_{pop}} \int_{a_{min,j}}^{max,j} \frac{\mathrm{d}n_j}{\mathrm{d}a}(a)\, C^{\mathrm{sca}}_{\lambda,j}(a) \times \left[\int_{4\pi} I_\lambda(\boldsymbol{r},\boldsymbol{k}')\, \Phi_{\lambda,j}(\boldsymbol{k},\boldsymbol{k}')\, \mathrm{d}\Omega' \right] \mathrm{d}a \\
&+ \rho(\boldsymbol{r}) \sum_{j=1}^{N_{pop}} \int_{a_{min,j}}^{max,j} \frac{\mathrm{d}n_j}{\mathrm{d}a}(a)\, C^{\mathrm{abs}}_{\lambda,j}(a)\, B_\lambda\left(T_j(\boldsymbol{r},a)\right)\, \mathrm{d}a.
\end{aligned}
\tag{2.1}
$$

The left-hand side of this equation represents the change of the intensity $I_\lambda(\boldsymbol{r},\boldsymbol{k})$ of the radiation field over an infinitesimal pathlength $\mathrm{d}s$ along the path determined by the position $\boldsymbol{r}$ and the propagation direction $\boldsymbol{k}$. The right-hand side contains the three source terms and two sink terms that are responsible for this change. The first term, with $j^*_\lambda(\boldsymbol{r})$ represents the primary source of radiation. The second and third terms, with $\rho(\boldsymbol{r})$ the dust density and $C^{\mathrm{abs}}_{\lambda,j}(a)$ and $C^{\mathrm{sca}}_{\lambda,j}(a)$ represent the attenuation due to absorption and scattering respectively, for dust grains of type j and radius a. In the fourth term, $\Phi_{\lambda,j}(\boldsymbol{k},\boldsymbol{k'})$ represent the scattering phase function for dust grains of the j'th family with size a. It is defined as the probability that a photon which comes from the direction $\boldsymbol{k'}$ will have $\boldsymbol{k}$ as its new direction. By convention it is normalized as

$$
\int_{4\pi} \Phi(\boldsymbol{k},\boldsymbol{k}',a)\, \mathrm{d}\Omega' = \int_{4\pi} \Phi(\boldsymbol{k},\boldsymbol{k}',a)\, \mathrm{d}\Omega \tag{2.2}
$$

where $\mathrm{d}\Omega$ is element of solid angle.

The fourth term represents the gain in radiation that is due to scattering into the line of sight. Finally, the last term on the right-hand side represents the contribution to the radiation field due to thermal emission of the dust grains; in this formula, $B_\lambda\left(T_j(\boldsymbol{r},a)\right)$ represents the spectral radiance for the equilibrium temperature of dust grains of type j with size a at the position $\boldsymbol{r}$. Whereas the absorption and scattering cross sections and the scattering phase functions are fundamental properties of the dust grains (for spherical grains, they can be obtained using Mie theory, Mie, 1908), the equilibrium temperatures of the dust grains must be determined from the condition of thermal equilibrium,

$$
\int_0^\infty C^{\mathrm{abs}}_{\lambda,j}(a)\, B_\lambda\left(T_j(\boldsymbol{r},a)\right)\, \mathrm{d}\lambda = \int_0^\infty C^{\mathrm{abs}}_{\lambda,j}(a)\, J_\lambda(\boldsymbol{r})\, \mathrm{d}\lambda, \tag{2.3}
$$

where $J_\lambda(\boldsymbol{r})$ is the mean intensity of the radiation field,

$$J_\lambda(\boldsymbol{x}) = \frac{1}{4\pi} \int_{4\pi} I_\lambda(\boldsymbol{r}, \boldsymbol{k})\, \mathrm{d}\Omega. \tag{2.4}$$

The direct radiative transfer problem comes down to solving this integro-differential equation for the intensity $I_\lambda(\boldsymbol{r}, \boldsymbol{k})$ and the dust temperature distribution $T_i(\boldsymbol{r})$ when the spectral and spatial distribution of the primary source emission and the spatial distribution, the size distribution and the optical properties of the various dust populations are known.

2.2.2 Monte Carlo radiative transfer

The key principle in Monte Carlo radiative transfer simulations is that the radiation field is treated as a flow of a finite number of photon packages. A simulation consists of consecutively following the individual path of each single photon package through the dusty medium. The journey or lifetime of a single photon package can be thought of as a loop: at each moment in the simulation, a photon package is characterized by a number of properties, which are generally updated when the photon package moves to a different stage on its trajectory. The trajectory of the photon package is governed by various events such as emission, absorption and scattering events. Each of these events is determined statistically by random numbers, generated from the appropriate probability distribution $p(x)\,\mathrm{d}x$. Typically, a photon emitted by a primary source, undergoes a number of scattering events and its journey ultimately ends when it is either absorbed by the dust or it leaves the system. A Monte Carlo simulation repeats this same loop for every single one of the photon packages and analyzes the results afterwards.

The mathematical details and practical implementation of Monte Carlo radiative transfer have both been described in detail by various authors (e.g. Cashwell & Everett, 1959; Mattila, 1970; Witt, 1977; Fischer et al., 1994; Bianchi et al., 1996; Gordon et al., 2001; Niccolini, Woitke, & Lopez, 2003; Wolf, 2003; Stamatellos & Whitworth, 2003; Juvela, 2005; Jonsson, 2006; Bianchi, 2008) and will not be repeated here in full detail. The overall approach in SKIRT is comparable to the DIRTY (Gordon et al., 2001; Misselt et al., 2001) and TRADING (Bianchi, 2008) radiative transfer codes and we refer the interested reader to these papers for more details. We will only give a compact description of the general characteristics of the SKIRT code and not describe all the details.

2.2.3 General overview of a SKIRT simulation

Each SKIRT simulation consists of three phases: the initialization phase, the emission phase and the clean-up phase.

The initialization phase consists of adopting the correct unit system, setting up the random

number generator, computing the optical properties of the various dust populations, constructing the dust grid, setting up the source geometry and setting up the instruments of the various observers. Once this initialization is finished, the actual simulation can start.

In the emission phase, we consider the transfer of the primary source of radiation (in our case AGN emission, but it can also include stellar emission or nebular line emission) through the dusty medium. The total bolometric luminosity of the primary source is divided into a very large number of photon packages (typically around 10^8), which are launched one by one through the dusty medium in random propagation directions. The entire routine is basically a single loop over all these photon packages. Once a photon package is launched into the dusty medium (either after an emission event or following a scattering event), it can be absorbed by a dust grain, it can be scattered by a dust grain, or it can travel through the system without any interaction. In a naive Monte Carlo routine, these three outcomes are possible and it is randomly determined which of them will happen. This is generally an inefficient procedure, though, which leads to poor signal-to-noise both in the absorption rates in the different cells and in the scattered light images. To overcome these problems, SKIRT employs a combination of the peeling-off technique (Yusef-Zadeh, Morris, & White, 1984), continuous absorption (Lucy, 1999; Niccolini, Woitke, & Lopez, 2003), forced scattering (Cashwell & Everett, 1959; Witt, 1977) and partly polychromatic photon packages (Baes et al., 2005a).

For the simulations presented in this thesis, we used the Bjorkman-Wood Monte Carlo approach with frequency distribution adjustment technique, presented by Bjorkman & Wood (2001) and critically discussed by Baes et al. (2005b). Contrary to the iterative Monte Carlo simulations, simulations based on the Bjorkman & Wood technique do not use separate phases for the primary source emission, dust self-absorption and dust emission, but it uses one single loop without iteration to handle both the primary source and dust emission. Bjorkman & Wood (2001) proposed a scheme in which, immediately after each individual absorption event, the dust temperature of the absorbing cell is recalculated and a new photon package is re-emitted at the position of the absorption. A mechanism called frequency distribution adjustment is included to ensure that the wavelength of each re-emitted photon package is chosen in such a way that it accounts for the incorrect wavelength distribution of the photon packages that have been emitted before from this cell (they were emitted with an incorrect wavelength distribution because the cell had a wrong temperature then). This technique ensures that at each moment during the simulation, the wavelength distribution from the photon packages emitted from the cell are in agreement with the cell's current temperature. As a result, no iteration is necessary at all.

The life cycle of a photon package ends when it either leaves the system or when the package contains virtually no more luminosity. The last phase of the Monte Carlo simulation starts when the last of the photon packages has lost 99.99% of its initial luminosity. It simply consists of calibrating and reading out the instruments (all output is written to FITS files) and other useful information, such as 3D absorption rate maps and dust temperature distributions.

2.2.4 Setup of the dust grid

A critical aspect in Monte Carlo radiative transfer simulations is the choice of the dust grid. The dust grid consists of tiny cells, each of which have a number of characteristics that fully describe the physical properties of the dust at the location of the cell. The choice of the grid has a significant impact on both the run time and the memory requirement of the simulation. Indeed, each photon package typically requires several integrations through the dust (i.e. the determination of the optical depth along the path and the conversion of a given optical depth to a physical path length), and the calculation time of a single optical depth typically scales with the number of grid cells crossed. Different kinds of dust grids can be applied in the SKIRT code. The most general grid is a 3D cartesian grid in which each dust cell is a rectangular cuboid. For simulations with a spherical or axial symmetry, we also have 1D spherical and 2D cylindrical grids (the elementary dust cells being shells or tori respectively). The distribution of the grid points (in 1D spherical, 2D cylindrical or 3D cartesian grids) can be chosen arbitrarily; linear, logarithmic, or power-law cell distributions have been pre-programmed, but any user-supplied grid cell distribution is possible.

2.3.1 Dust distribution and properties

We approximate the spatial dust distribution around the primary continuum source with a conical torus (i.e. a flared disk). Its characteristics are defined by (a) the half opening angle Θ, which also defines the maximum height extent to which the dust is distributed, (b) the inner and outer radius, $R_{\rm in}$ and $R_{\rm out}$ respectively, and (c) the parameters describing dust density distribution, p and q (see below). A schematic representation of the adopted geometry is given in Fig. 2.3. For the inner radius of the dusty torus we adopted the value of 0.5 pc, at wich the dust grains are heated to the temperature of $\sim$ 1180 K, according to the prescription given by Barvainis (1987):

$$R_{\rm in} \simeq 1.3 \cdot \sqrt{L_{46}^{AGN}} \cdot T_{1500}^{-2.8} \qquad [\rm pc], \tag{2.5}$$

where L_{46}^{AGN} is the bolometric ultraviolet/optical luminosity emitted by the central source, expressed in units of 10^{46} erg s^{-1} and T_{1500} is the sublimation temperature of the dust grains given in units of 1500 K.

We describe the spatial distribution of the dust density with a law that allows a density gradient along the radial direction and with polar angle, as the one adopted by Granato & Danese (1994):

$$\rho\,(r,\theta) \propto r^{-p} e^{-q|cos(\theta)|}, \tag{2.6}$$

where r and θ are coordinates in the adopted coordinate system (see Fig. 2.3).

The dust mixture consists of separate populations of graphite and silicate dust grains with a classical MRN size distribution (Mathis, Rumpl & Nordsieck, 1977):

$$dn(a) = Ca^{-3.5}da, \tag{2.7}$$

where the size of grains, a, varies from 0.005 to 0.25 μm for both graphite and silicate. The normalization factors for size distribution are $C = 10^{-15.13}$ and $C = 10^{-15.11}$ cm$^{2.5}$ for graphite and silicate, respectively (Weingartner & Draine, 2001). Optical properties are taken from Laor & Draine (1993) and Li & Draine (2001).

The dust is distributed on a 3D cartesian grid composed of a large number of cubic cells. The dust density is constant within each cell. The standard resolution for our simulations is 200 cells along each axis (8×10^6 cells in total). However, to properly sample the dust properties, an increase in the torus size requires an increase of the resolution of the computational grid as well. Thus, to simulate a torus twice the size of the 'standard model', one needs to employ a grid with 400 cells along each axis, that is, 64×10^6 cells in total.

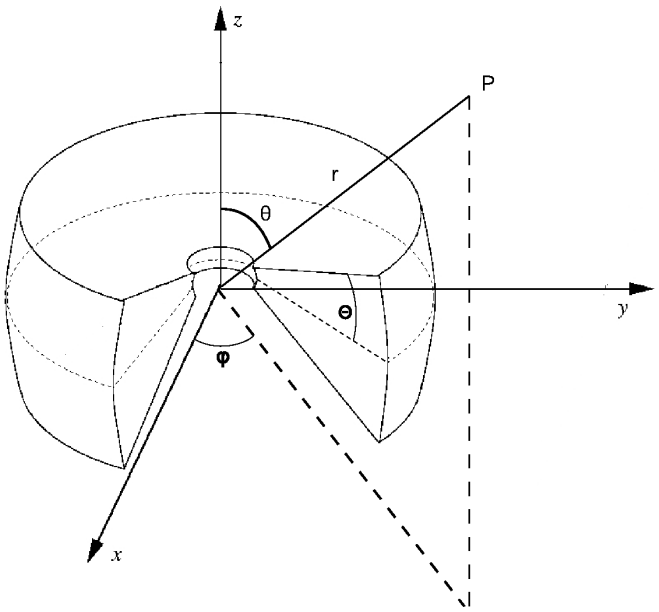

Figure 2.3 Schematic representation of the adopted model geometry and coordinate system. The dust distribution is approximated with a conical torus (i.e. a flared disk)

In the case of a smooth density distribution, the axial symmetry in our model reduces the 3D radiative transfer computations to a 2D problem, with a significant gain both on the computational time and the memory usage. However, the prescription we use for generating clumpy models demands a 3D cartesian grid. Therefore, such a grid was used throughout all our simulations, in order to avoid any possible differences due to the adoption of different grids. To ensure that the adopted resolution is sufficient to properly sample the dust, for each simulation we compare the actual and expected values of (a) the face-on and edge-on central surface density and (b) the total dust mass.

The emission for all models was calculated on an equally spaced logarithmic wavelength grid ranging from 0.001 to 1000 μm. A finer wavelength sampling was adopted between 5 and 35 μm, in order to better resolve the shape of 10 and 18 μm silicate features. Each simulation is calculated using 10^8 photon packages.

2.3.2 Spectral energy distribution of the primary source

The primary continuum source of dust heating is the intense UV-optical continuum coming from the accretion disk. A very good approximation of its emission is a central, point-like energy source, emitting isotropically. Its SED is very well approximated by a composition of power laws with different spectral indices in different spectral ranges. The adopted values

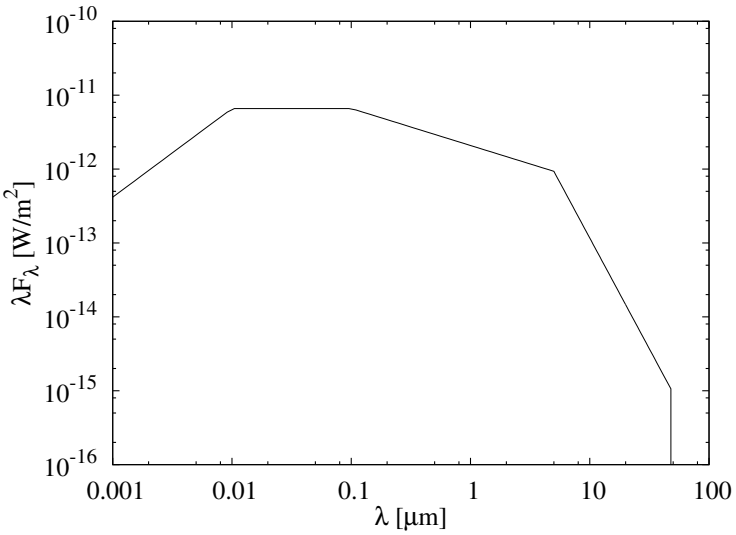

Figure 2.4 The SED of the primary source, i.e. the accretion disk, which we assume to irradiate as a composition of power laws, with different indices for different wavelengths ranges (see text for details).

are:

$$\lambda L(\lambda) \propto \begin{cases} \lambda^{1.2} & 0.001 \leqslant \lambda <\leqslant 0.01 \quad [\mu\mathrm{m}] \\ \lambda^{0} & 0.01 < \lambda \leqslant 0.1 \quad [\mu\mathrm{m}] \\ \lambda^{-0.5} & 0.1 < \lambda \leqslant 5 \quad [\mu\mathrm{m}] \\ \lambda^{-3} & 5 < \lambda \leqslant 50 \quad [\mu\mathrm{m}] \end{cases} \tag{2.8}$$

and the resulting SED is plotted on Fig. 2.4. These values have been quite commonly adopted in the literature, and come from both observational and theoretical arguments (see e.g., Schartmann et al., 2005). We have anyway verified that changes in the shape of the primary source SED affect only very marginally the infrared re-emission. For the bolometric luminosity of the primary source we adopted the value of $10^{11}\ L_{\odot}$ (see e.g., Davis & Laor, 2011).

As mentioned above, an isotropic emission of the central source is commonly adopted in the literature (e.g. Schartmann et al., 2005; Hönig et al., 2006; Nenkova et al., 2008a). However, the disk emission is inevitably anisotropic (see, for example, Kawaguchi & Mori, 2011, and references therein). Therefore, we have performed additional calculations assuming anisotropic radiation of the central source, in order to investigate the resulting influence on the model SEDs. Radiation flux (F) from a unit surface area of an optically thick disk toward a unit solid angle at the polar angle of θ decreases with an increasing θ according to the formula given by Netzer (1987):

$$F = F_0 \cos\theta(1 + 2\cos\theta), \tag{2.9}$$

where F_0 represents the flux along the z axis ($\theta = 0^{\circ}$), the first term represents the change in the projected surface area, and the the latter represents the limb darkening effect. For simplicity, in

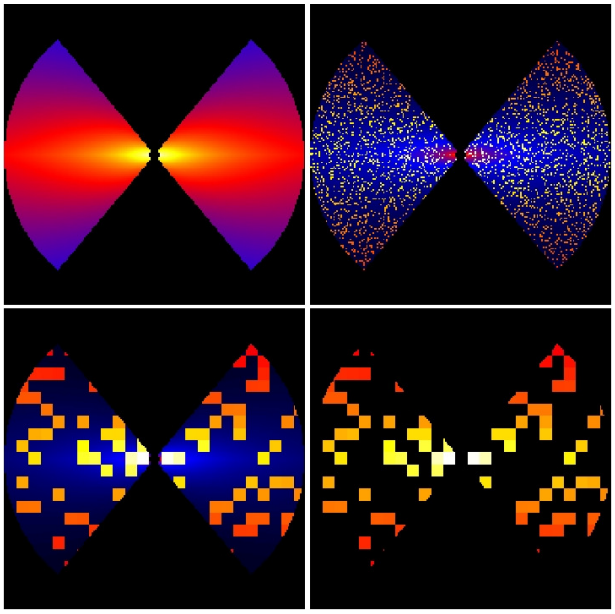

Figure 2.5 Dust density distribution at the meridional plane, given in logarithmic color scale. Density law parameters are $p = 1$ and $q = 2$. The smooth dust distribution is presented in the top left panel. The top right and bottom left panel present two-phase dust distribution for two different sizes of clumps: each clump is composed of one cubic grid cell (top right) and $8 \times 8 \times 8$ grid cells (bottom left). In the bottom right panel, a clumps-only dust distribution is presented. The contrast parameter between high- and low-density phases in the two-phase and clumps-only models is 100 and 10^9, respectively.

our calculations we take into account only the first term. As the accretion disk radiation varies with θ, the dust sublimation radius also depends on it:

$$R_{in} = R_{in,0}(2|\cos\theta|)^{0.5}, \tag{2.10}$$

where $R_{in,0}$ is the dust sublimation radius estimated assuming isotropic emission. As a result, the inner edge of the torus is (a) closer to the central source than suggested by the Eq. 2.5 and (b) the structure of the edge is concave (Kawaguchi & Mori, 2010, 2011). Also, Kawaguchi & Mori (2010) found that the dust sublimation radius can decrease down to $0.1R_{in,0}$, all the way to the outermost radius of the accretion disk. However, due to the numerical constraints, that is, the minumum size of the dust cell in the computational grid we are currently limited to, we cannot allow the dust to be placed all the way to the primary source. Instead, we are forced to put a limit on the minimum allowed dust sublimation radius at 0.225 pc ($0.45R_{in,0}$). We discuss the influence of the anisotropic central source radiation on the dusty tori model SEDs in the Sec. 2.4.4; throughout the rest of this work, the isotropic emission is assumed.

2.3.3 Two-phase medium: the approach

Models of emission in which the dust is uniformly, smoothly distributed within the toroidal region are obtained starting from Eq. 2.6. The density gradient is determined by the two parameters, p and q. The total amount of dust is fixed based on the equatorial optical depth at 9.7 μm ($\tau_{9.7}$). While for the smooth models distributing the dust is straightforward, for the clumpy model this process is non-trivial. As hydrodynamical simulations of Wada & Norman (2002) demonstrated, dust in tori is expected to take the form of a multiphase structure, rather than isolated clumps. Therefore, we adopted the approach which allows us to generate such a medium. We start from the corresponding smooth models, i.e. the one with the same global parameters, and then apply the algorithm described by Witt & Gordon (1996) to generate a two-phase clumpy medium. According to this algorithm, each individual cell in the grid is assigned randomly to either a high- or low-density state by a Monte Carlo process. The medium created in such a way is statistically homogeneous, but clumpy. The filling factor determines the statistical frequency of the cells in the high-density state and can take values between 0 and 1. For example, a filling factor of 0.01 represents a case of rare, single high-density clumps in an extended low-density medium. The process for the clump generation is random with respect to the spatial coordinates of the individual clumps themselves. Thus, as the filling factor is allowed to increase, the likelihood that adjoining cells are occupied by clumps increases as well. This leads to the appearance of complex structures formed by several merged clumps. For filling factor values $\gtrsim 0.25$, clumps start to form an interconnected sponge-like structure, with low-density medium filling the voids. We form larger clumps by forcing high-density state into several adjoining cells.

To tune the density of the clumps and the inter-clump medium, we use the 'contrast parameter', defined as the ratio of the dust density in the high- and low-density phase. This parameter can be assigned any positive value. For example, setting the contrast to one would result in a smooth model. Setting extremely high value of contrast (> 1000) effectively puts all the dust into the clumps, without low-density medium between them. An example of dust density distributions at the meridional plane for smooth, two-phase and clumps-only models is given in Fig. 2.5.

2.3.4 Parameter grid

In this section we present the adopted values of parameters used to calculate a grid of models for our analysis.

For the inner and outer radius of the torus we adopted the values 0.5 and 15 pc, respectively. The half opening angle of the torus – Θ – is fixed to 50° for all of our model realizations. All models are calculated at 7 different line-of-sight inclinations, namely 0°, 40°, 50°, 60°, 70°, 80° and 90°, where $i = 0°$ represents a face-on (type 1) AGN and $i = 90°$ an edge-on (type 2) AGN. Inclinations between 0° and 40° (dust-free lines of sight) were omitted since their SEDs

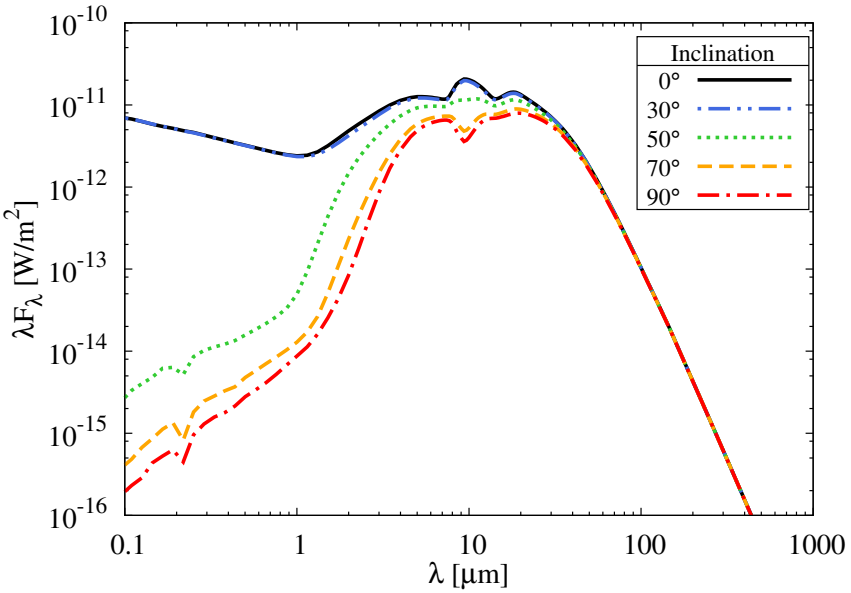

Figure 2.6 Dependence of the modeled SED on the viewing angle: $i = 0°$ (solid line), $i = 30°$ (dash-double-dotted), $i = 50°$ (dotted), $i = 70°$ (dashed), $i = 90°$ (dash-dotted). The first two, almost identical (in fact, they lay upon each other) are associated with dust-free paths. The inner and outer radii of the torus are 0.5 and 15 pc, respectively, the half opening angle of the torus, Θ, is 50°, the optical depth is $\tau_{9.7} = 5$, the parameters of the dust density distribution are $p = 1$ and $q = 2$, the clump size is 1.2 pc (or $\sigma = 12.5$), the filling factor 0.25 and the contrast parameter 100.

show no appreciable difference with respect to the full face-on view. The equatorial optical depth $\tau_{9.7}$ takes the values 0.1, 1.0, 5.0, 10.0. We note here that this is the optical depth of the initial smooth model, before the dust is redistributed to make the clumpy one (see Sec. 2.3.3). Thus, the exact value along the given line of sight will vary due to the random distribution of clumps. The parameters defining the spatial distribution of the dust density (Eq. 2.6) are $p = 0$, 1 and $q = 0$, 2, 4, 6.

Defining the relative clump size, σ, as the ratio of the outer radius of the torus over the clump size:

$$\sigma = R_{out} / D_{clump} \tag{2.11}$$

we explored the clumpy models for two different clump sizes, 0.15 pc and 1.2 pc, that is, $\sigma = 100$ and $\sigma = 12.5$, respectively. The number of clumps in the former case is 9×10^5, and each clump occupies one grid cell. In the latter case there are $\sim$ 3000 clumps, each one being composed of $8 \times 8 \times 8$ grid cells. The adopted filling factor values are 0.15 in the case $\sigma = 100$, and 0.25 in the case $\sigma = 12.5$ models. Both values allow us to have single, as well as clusters of high-density clumps immersed into a low-density medium. The contrast between high- and low-density phases is fixed at 100.

Table 2.1 The grid of parameters for which the models have been computed.

Parameter	Adopted values
L	$10^{11}\ L_{\odot}$
R_{in}	0.5 pc
R_{out}	15 pc
$\tau_{9.7}$	0.1, 1.0, 5.0, 10.0
p	0, 1
q	0, 2, 4, 6
Θ	50°
Filling factor	0.15, 0.25
Contrast	100 , 10^9
Size of clumps	0.15 pc, 1.2 pc
Inclination	0°, 40°, 50°, 60°, 70°, 80°, 90°

We generated three sets of models with the same global physical parameters: (a) models with the dust distributed smoothly, (b) models with the dust as a two-phase medium and (c) models with a contrast parameter set to an extremely high value (10^9), effectively putting all the dust into the high-density clumps. We will refer to these models as 'smooth', 'two-phase' and 'clumps-only', respectively. For clumpy models (both two-phase and clumps-only) we generated another set of models with the same parameters, but with a different random distribution of clumps.

For each model we calculated SEDs and images of torus for all the points in the wavelength grid. Calculated flux is scaled for the torus distance of 10 Mpc from the observer. The parameter grid is summarized in Table 2.1.

2.4 Properties of the IR emission: analysis and discussion

In this section we discuss the influence of different parameters on the general shape of the SEDs of the two-phase models and analyze their observable properties. The following analysis refers to the two-phase models with $\sigma = 12.5$. We will address how the properties of these models compare to properties of models with $\sigma = 100$, clumps-only, and smooth models in Sections 2.4.9 and 2.4.10.

2.4.1 SED dependence on the viewing angle

As it was demonstrated in early works (e.g. Granato & Danese, 1994), the SED of a dusty torus depends on the viewing angle. In Fig. 2.6 we show the SED dependence on the inclination of the torus. There is a clear distinction between cases of dust-free lines of sight ($i = 0°, 30°$) and those that pass through the torus ($i = 50°, 70°, 90°$). For the adopted value of half opening angle ($\Theta = 50°$), this transition occurs at inclination $i = 40°$. The most notable difference is found shortward of 1 μm. In the case of dust-free lines of sight, we directly see the radiation coming from the accretion disk, while in the case of dust-intercepting paths most of the radiation is absorbed and scattered at different wavelengths. This is especially pronounced in those systems where the density remains constant with the polar angle. In the case of a non-constant density, the transition from face-on to edge-on view is smoother. An exception is the case of very low optical depths, where it is possible to directly 'see' the central source even when viewed edge-on. Another important difference between dust-free and dust-intercepting lines of sight is the 10 μm silicate feature, which is expected to appear in the emission in the former case and in the absorption in the latter. The properties of this feature is discussed in detail in Section 2.4.5. Images of the torus at different wavelengths, for the type 1 and type 2 lines of sight are shown in Fig. 2.7. From the figure it is clear that, at shorter wavelengths, it is the radiation from the inner (and hotter) region that dominates. At longer wavelengths, the emission arises from the dust placed further away. Thus, the size of the torus is wavelength dependent. In Fig. 2.8 we present the total SED and its thermal and scattered components, along with the primary source emission, for the face-on and edge-on views. As it can be seen from this figure, the thermal component is dominant in the mid- and far-infrared part of the SED and its shape is similar for both type 1 and type 2 orientations. The shape and amount of the scattered component is quite different; in the edge-on view it determines the total SED at shorter wavelengths, while in the face-on view it is negligible compared to the primary source emission.

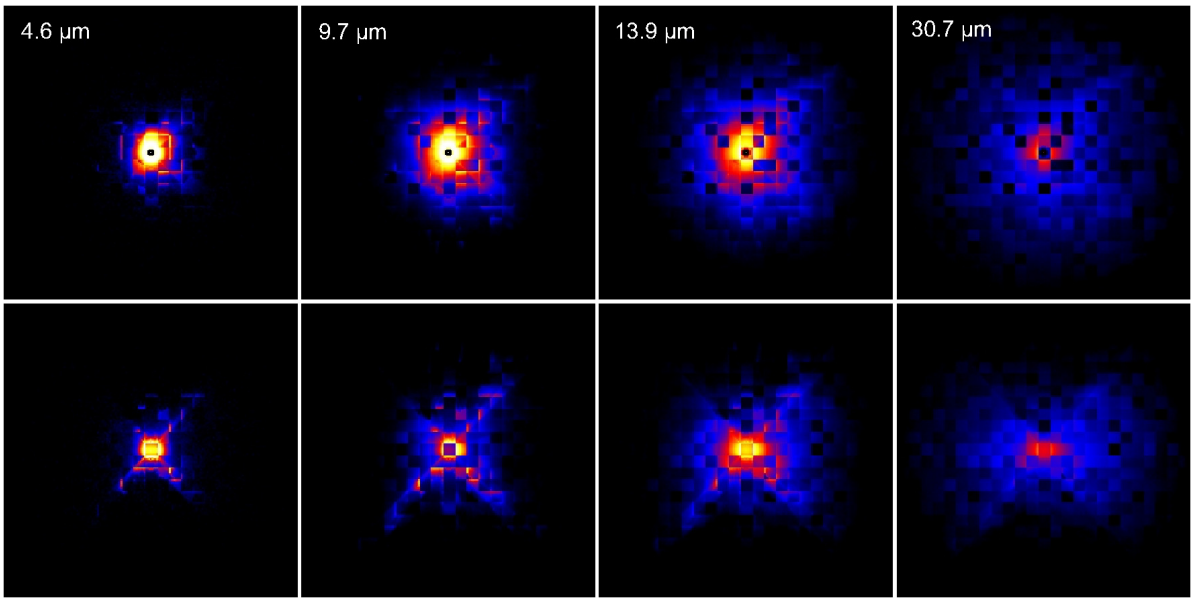

Figure 2.7 Images of the torus at different wavelengths. Top row is the face-on view, bottom row edge-on view. From left to right, panels represent images at 4.6, 9.7, 13.9, and 30.7 μm. Images are given in logarithmic color scale. The parameters are the same as in Fig. 2.6. The visible squared structure is due to clumps which in the model are in the form of cubes.

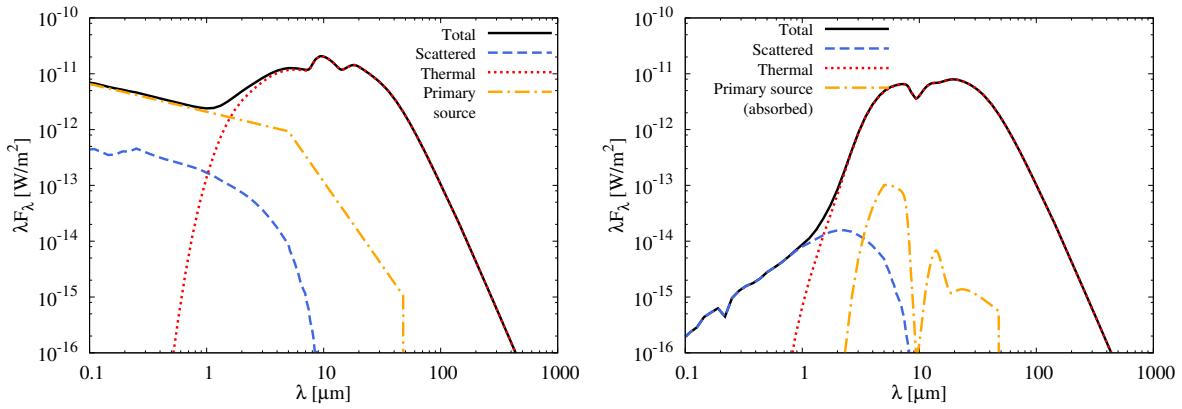

Figure 2.8 The total (solid line), thermal (dotted line), scattered (dashed line) and primary source (dash-dotted line) emission are plotted. Left panel: face-on view; right panel: edge-on view. The parameters are the same as in Fig. 2.6.

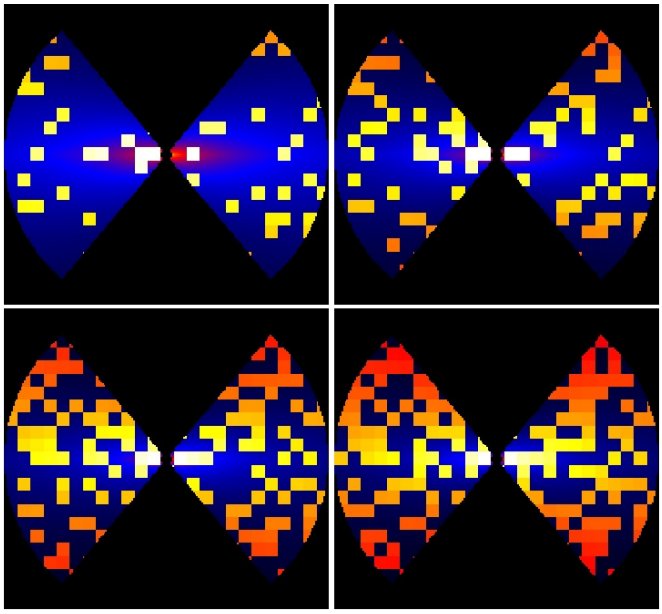

Figure 2.9 Dust density distribution at the meridional plane for different filling factors, in logarithmic color scale. The filling factors are: 0.15 (top left panel), 0.25 (top right), 0.35 (bottom left), and 0.45 (bottom right). All other parameters are the same as in Fig. 2.6.

2.4.2 SED dependence on the filling factor and contrast

As described in Section 2.3.3, the two parameters that determine the characteristics of the two-phase medium are the filling factor and the contrast. The filling factor determines the percentage of grid cells in a high-density state. Models with low values for the filling factor (e.g. < 0.1) represent systems with rare, single high-density clumps in extended low-density medium. As the filling factor increases, the number of clumps will increase as well, forming clusters of clumps, or even single, interconnected sponge-like structure. This is illustrated in Fig. 2.9, where we show dust density distributions at the meridional plane for different filling factors. Fig. 2.10 shows SEDs of models for different filling factors, compared with SED of the corresponding smooth model. From this figure one can see that, as the filling factor increases, the overall mid-infrared emission increases as well. For filling factor value of ~ 0.25, in the face-on view, the silicate feature is attenuated. As the filling factor increases, clumps start to form sponge-like structures, more and more resembling a smooth dust distribution, and the strength of the silicate feature approaches the strength in the corresponding smooth model. In the edge-on, a filling factor value of ~ 0.25 produces silicate features in weaker absorption than in the corresponding smooth model. As the filling factor increases, the strength of the silicate feature approaches the strength of the feature in the smooth models.

The 'contrast' parameter sets the density ratio between the high- and low-density phases. Fig. 2.11 shows the model SED dependence on this parameter. In the face-on view, for increasing contrast, both the hot dust emission ($\sim 1 - 6\ \mu$m) and the strength of the silicate feature de-

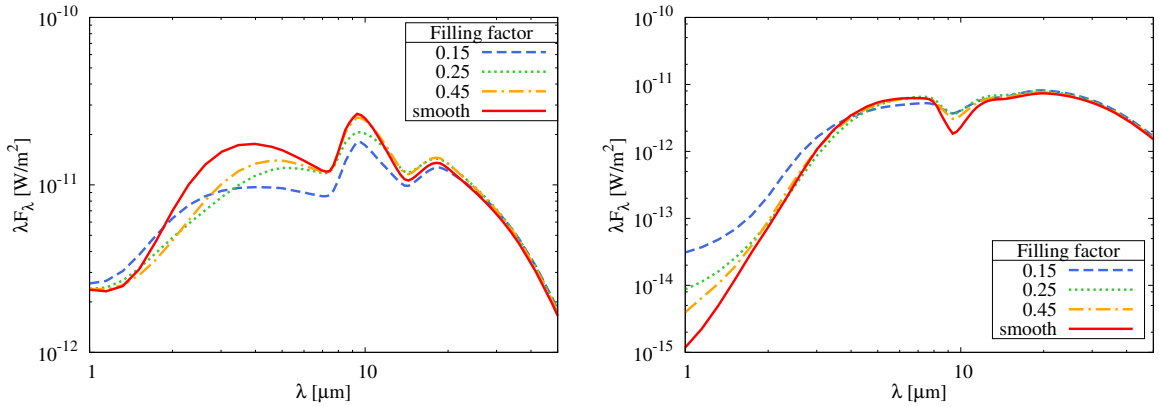

Figure 2.10 Model SEDs for different filling factors: dashed line: 0.15; dotted line: 0.25; dash-dotted line: 0.45. For comparison purposes, the SED of a corresponding smooth model is also plotted (solid line). All other parameters are the same as in Fig. 2.6. Left panel: face-on view; right panel: edge-on view.

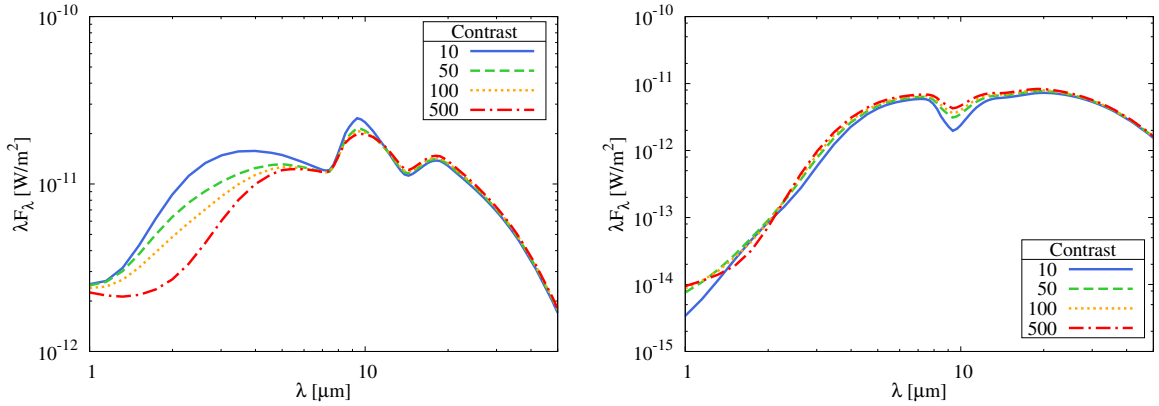

Figure 2.11 Model SEDs for different values of contrast parameter. Contrast have values of 10 for solid line, 50 for dashed, 100 for dotted, and 500 for dash-dotted. All other parameters are the same as in Fig. 2.6. Left panel: face-on view; right panel: edge-on view.

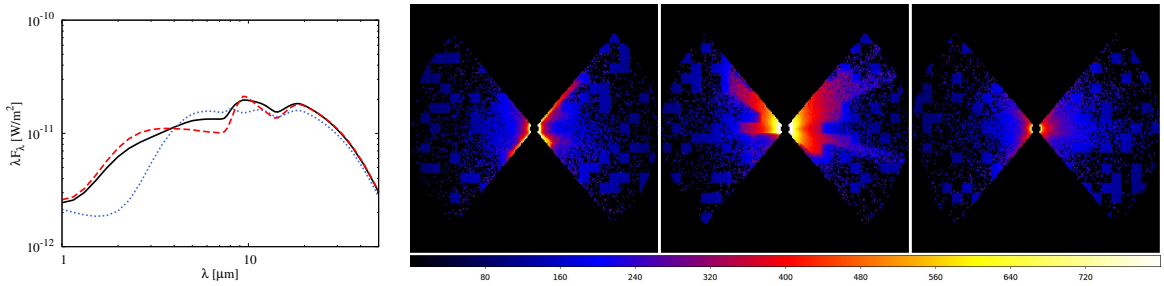

Figure 2.12 Temperature distribution at the meridional plane for the three different random distributions of clumps (three rightmost panels) and corresponding SEDs for face-on view (left panel). The solid line corresponds to the left panel, the dashed to the middle, and the dotted to the right. The parameters are the same as in Fig. 2.6. Temperature images are shown in a logarithmic color scale, which is for clarity of the images cut off at 800 K.

crease. From the same figure we also see that, for higher contrast values, the peak of the silicate feature is slightly shifted toward longer wavelengths. In the edge-on view, the silicate feature in absorption gets weaker with increasing contrast.

2.4.3 SED dependence on the random distribution of clumps

The shape and overall near- and mid-infrared emission strongly depend on the distribution of dust in the innermost region. Changing the random arrangement of clumps, along with choosing a particular line of sight, can affect the resulting SED significantly, as illustrated in Fig. 2.12. As described in Section 2.3.3, the process for clump generation is random with respect to the spatial coordinates of the individual clumps. As a consequence, adjoining cells can be occupied by individual clumps, forming complex structures of several connected clumps. In models with a higher concentration of clumps in the innermost region, due to the shadowing effect, the absorption is increased and silicate feature is suppressed.

This characteristic imports a degree of the degeneracy in the features of the SEDs, which will be less directly dependent on the physical input parameters. Even though the spatial position of the clumps is not related to the physical properties of dusty tori, their re-arrangement has a clear impact on the infrared emission. It is, in some way, mimicking a change in the optical depth, which might appear either to increase or decrease, depending on the clumps re-arrangement, especially in the innermost regions.

Some random arrangements of clumps have interesting repercussions. Because of clumpiness, the difference between the SED of type 1 and 2 objects is not truly an issue of orientation; it is rather a matter of probability of directly viewing the main energy source of the AGN (Nenkova et al., 2008b). As a result, type 1 sources can be detected even from what are typically considered as type 2 orientations (see Fig. 2.1). Such a scenario provides an explanation for the few Seyfert galaxies with type 1-like optical spectra whose $0.4 - 16$ μm SED resembles that

of a type 2 AGN (Alonso-Herrero et al., 2003). Conversely, if a clump happens to obscure the central engine from an observer, that object would be classified as type 2 irrespective of the viewing angle. In such cases, the clump may move out of the line-of-sight, creating a clear path to the nucleus and a transition to a type 1 spectrum. Such transitions between type 1 and type 2 line spectra have been observed in a few sources (see Aretxaga et al., 1999, and references therein).

2.4.4 Anisotropy of the primary source radiation

As described in Sec. 2.3.2, an isotropic source emission is commonly adopted in the radiative transfer modeling of dusty tori; however, the accretion disk emission is actually anisotropic (Netzer, 1987; Kawaguchi & Mori, 2011). In this section, we discuss the influence of anisotropic source radiation on the model SEDs. Dependence of the accretion disk radiation on the direction is taken according to Eq. 2.9 and the corresponding change of the dust sublimation radius according to Eq. 2.10. In Fig. 2.13 we present the resulting model SEDs if the anisotropic radiation of the primary source is assumed (dotted line) and compare them to the corresponding SEDs obtained in the case of the isotropic source (solid line) for different inclinations. SEDs were calculated for the inclinations between 0° and 90° with the step of 10°; for the clarity of the figure, only SEDs for three inclinations, 0°, 50° and 90° are shown.

We found that, when anisotropy of the central source is assumed, the IR SED can indeed change, resulting in a lower emission, though roughly keeping the same shape. This is a logical consequence coming from the fact that, for a given bolometric luminosity of the accretion disk, an anisotropic source whose characteristics are those as described above, is emitting more power in the dust-free region: the overall result is a less luminous torus. The excess of emission shortward of $\sim 3\,\mu$m is seen in the dust-free lines of sight, because, at these wavelengths the primary source contribution is still significant. Again, as expected from the properties of radiative transfer (Ivezić & Elitzur, 1997), we found that the shape and the features of the SED (e.g. the $10\,\mu$m feature) are not affected. Therefore we conclude that our analysis in the rest of the chapter is not affected by the isotropic approximation for the central source radiation.

2.4.5 The silicate feature strength

As it was mentioned above, an important characteristic in the infrared part of an AGN SED is the so-called silicate feature. This silicate feature is caused by stretching modes of Si-O molecules, giving rise to either emission or absorption band, peaking at $\sim 10\,\mu$m. All of the early models were dealing with the following issue: while they were properly predicting it in the absorption in type 2 objects –in agreement with what was indeed observed–, observations from that period were not supporting the models' prediction of a silicate feature in emission in type 1 AGN. In fact, one of the main issues driving the development of clumpy models, aimed

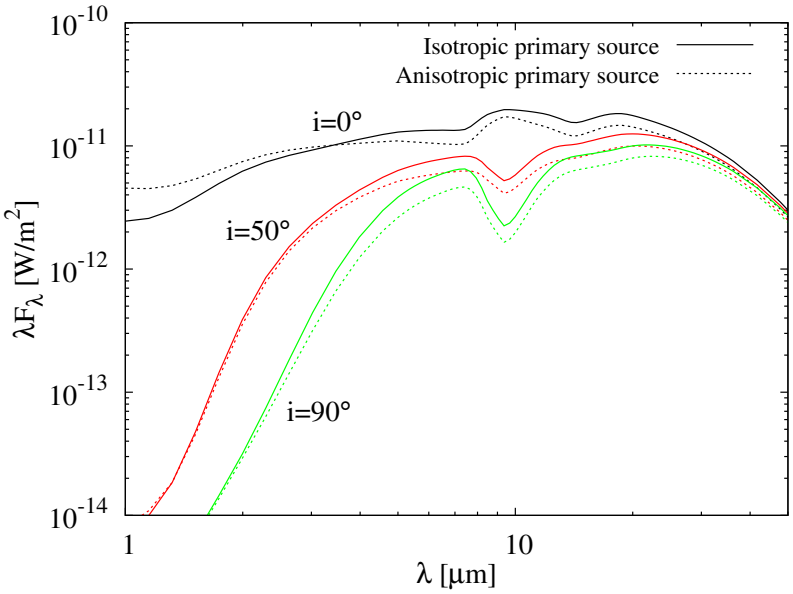

Figure 2.13 Model SEDs assuming isotropic (solid line) and anisotropic (dotted line) accretion disk radiation. Inclinations are indicated in the plot. All the torus parameters are the same as in Fig. 2.6, except for the q parameter which here takes the value of 0.

at addressing this discrepancy between models and observations. Later observations performed by *Spitzer* with its infrared spectrometer IRS, showed that for a number of type 1 objects this feature is indeed observed in the emission, partially solving this issue. Recently, Hony et al. (2011) reported the detection of a very strong 10 μm feature in emission. On the other hand, Fritz et al. (2006) showed that smooth models are also able to properly reproduce the observed emission in this range. Furthermore, the comparative study performed by Feltre et al. (2012) showed that clumpy and smooth dust distributions are equally able to reproduce both observed broad-band SEDs and mid-infrared *Spitzer* spectra.

The strength of the 10 μm feature can be characterized by the dimensionless parameter S, the natural logarithm of the peak-over-continuum ratio (Pier & Krolik, 1992; Granato & Danese, 1994). The continuum is defined by a power law connecting the fluxes at 6.8 and 13.9 μm. S assumes positive values for a feature in the emission and negative ones if it is in the absorption.

In a face-on view, S takes values in the range $\sim 0.1 - 1$. The silicate feature is present in a strong emission in the models with lower optical depths ($\tau_{9.7} = 0.1, 1$). Models with an optical depth of $\tau_{9.7} = 5$ are showing a wider range of intensities, most of them of moderate strength, with a few cases of strong or weak emission. The strength of the feature in models with high optical depth ($\tau_{9.7} = 10$) is also showing a wide range of intensities, but with overall lower values, and is significantly attenuated in some cases.

For the majority of the edge-on models with optical depths of $\tau_{9.7} = 5$ and 10 the silicate

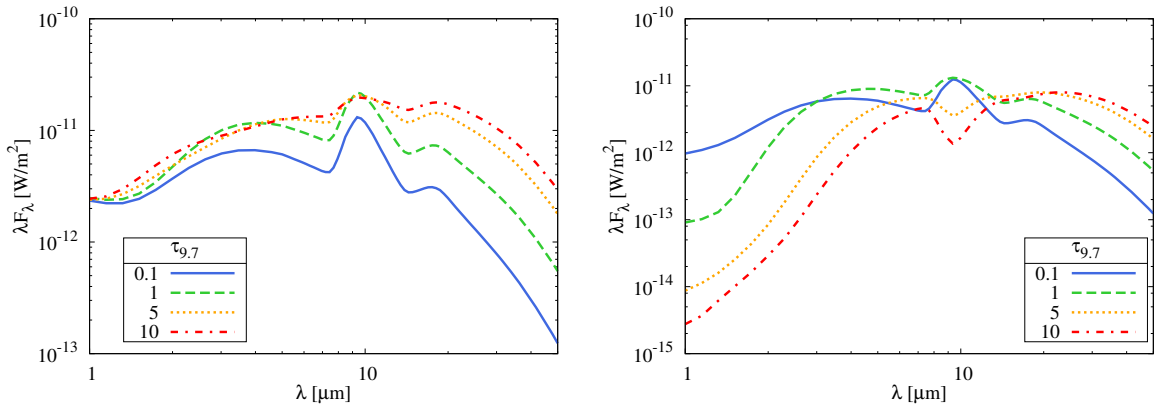

Figure 2.14 Model SEDs for different optical depths. The solid line represents the case of an optical depth of $\tau_{9.7} = 0.1$, the dashed of $\tau_{9.7} = 1.0$, the dotted of $\tau_{9.7} = 5.0$, and the dash-dotted of $\tau_{9.7} = 10.0$. All other parameters are the same as in Fig. 2.6. Left panel: face-on view; right panel: an edge-on view.

feature is in the absorption, with $-2.2 \leq S \leq -0.2$. Models with low optical depths ($\tau_{9.7} = 0.1$ and 1) do not provide enough dust to absorb the silicate feature and, in this case, it is present in emission even in the edge-on view. Fig. 2.14 shows SED dependence on the optical depth. To further illustrate dependence of the strength of the silicate feature on different parameters, in Fig. 2.15 we plot its intensity, S, as a function of the optical depth ($\tau_{9.7}$), of the dust distribution parameters (p and q) and of the clumps size σ. For these calculations, the following values of the parameters were chosen: $\tau_{9.7} = 10$, $p = 1$, $q = 0$, $\sigma = 12.5$ and then each of these parameters was varied while all the others were kept constant.

2.4.6 SED width

Following Pier & Krolik (1992) and Granato & Danese (1994), SED width, W, is defined as the logarithmic wavelength interval in which the power λF_λ emitted in the infrared is more than one third of the peak value. For a black body this parameter has a value of ~ 0.7, while in the observed spectra its value is always larger than 1.3. The vast majority of model SEDs, both in the face-on and edge-on views, have a width spanning the $1.2 \leq W \leq 1.7$ range. SEDs with widths $W > 1.55$ are produced by models with optical depths of 5 and 10 because (a) these are the models with the larger amounts of dust and (b) the high values of the optical depth provide a better shielding of the primary source, allowing colder dust temperatures causing, in turn, the broadening of the SED. A small fraction of model SEDs have $W < 1.15$. These widths are almost exclusive to models with the optical depth of 0.1 and the density law parameter $p = 1$, which produce the silicate feature in the very strong emission. Since the maximum of the infrared emission often coincides with the peak of the silicate feature, such models produce lower W values.

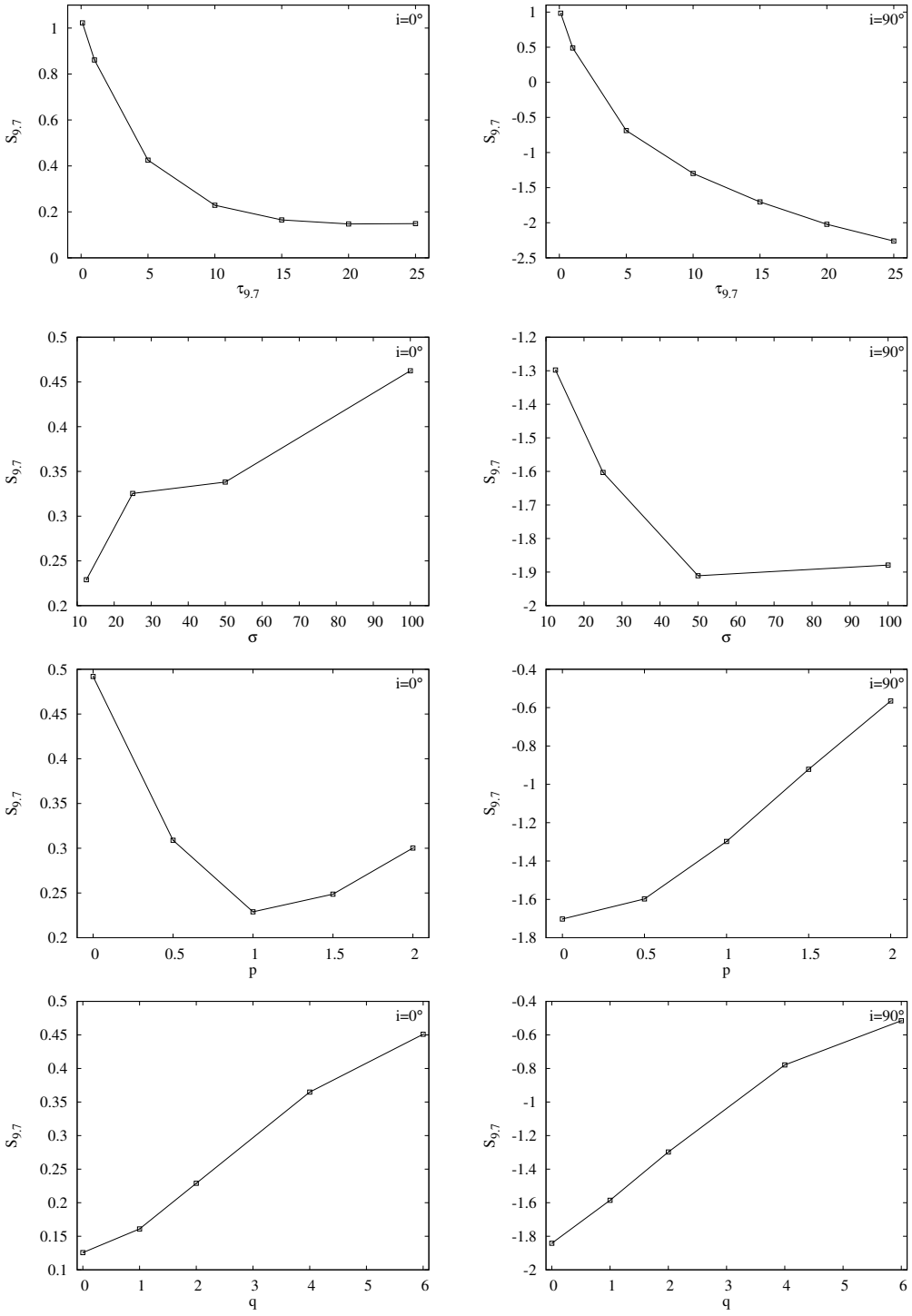

Figure 2.15 Dependence of the strength of the silicate feature (S) on the different parameters. From top to bottom, panels illustrate dependence on the optical depth ($\tau_{9.7}$), clump size (σ) and dust distribution parameters (p and q). Panels on the left present values for the face-on view, panels on the right for the edge-on view.

Another parameter that affects the SED width is the size of the torus. Increasing the radius, while keeping the optical depth constant, means that the amount of dust in the outer (and colder) regions increases. As these regions emit in the far-infrared, an increase in the radius makes the SED wider. For the same reason (amount of cold dust) W increases with the total amount of dust, that is, with the optical depth (see Fig. 2.14).

The edge-on orientations produce wider SEDs than the face-on ones, with almost 50% of them having $W > 1.6$. This is because in the edge-on view the silicate feature is usually in absorption. As a result, the peak of the infrared emission decreases, leading to wider SEDs. Furthermore, in the edge-on view the received radiation is mainly coming from the outer regions that contribute to the far-infrared emission.

2.4.7 Isotropy of the infrared emission

Following Dullemond & van Bemmel (2005) we define the isotropy parameter, I, as the ratio of the total integrated infrared flux in an edge-on view over the total integrated infrared flux in a face-on view. A larger value of I implies there is more isotropy.

Anisotropy in the infrared emission is expected in all systems with the torus-like geometry. This is because in the face-on view the observer has a direct view of the primary source and the inner, hotter region of the torus, while in the edge-on view they are obscured. The values of I strongly depend on the optical depth. Models with a low optical depth are almost perfectly isotropic: models with $\tau_{9.7} = 0.1$ produce $I > 0.95$ and in models with $\tau_{9.7} = 1$, I takes values around ~ 0.75. Models with a higher optical depth have an anisotropic emission, with most I values being around ~ 0.50 and ~ 0.40 for optical depths of 5 and 10, respectively. The lowest I value in our models is ~ 0.37.

2.4.8 The peak of the infrared emission

Another important feature characterizing the infrared SED of AGNs is the wavelength at which it peaks. We measure this quantity in our model SEDs expressed in λF_λ. The majority of the models in our grid peak around $\sim 9.4\,\mu$m, more or less corresponding to centre of the silicate band. A small fraction of models has its maximum in the ~ 20 to $\sim 29\,\mu$m range: all of these models have a high optical depth (either 5 or 10). In the face-on view, almost all models peak at $\lambda = 9.4\,\mu$m. In the edge-on view, models exhibiting the silicate feature in emission (i.e. models with low optical depths of $\tau_{9.7} = 0.1, 1$) also peak at $9.4\,\mu$m, due to the prominence of the $10\,\mu$m feature in emission in low-optical depth systems and lower dust content. Edge-on models with higher optical depths peak beyond $\sim 20\,\mu$m.

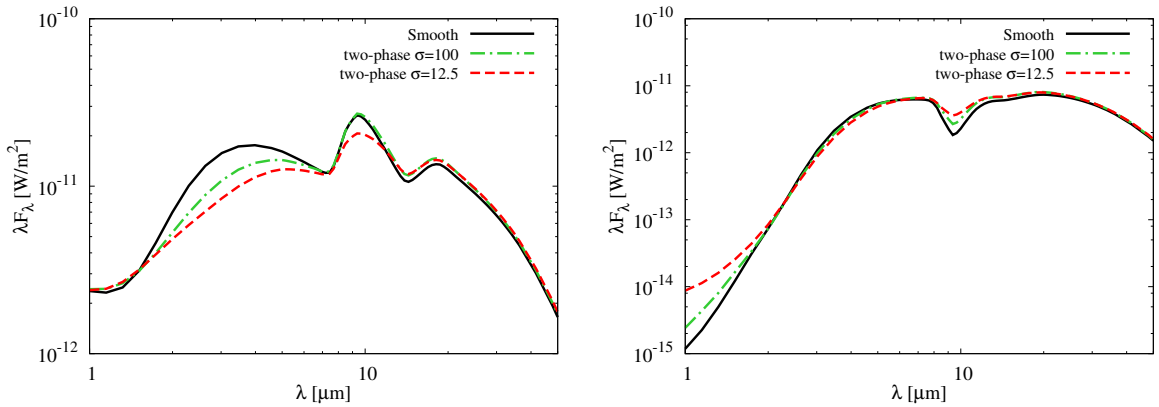

Figure 2.16 Comparison of smooth and clumpy model SEDs. Full solid line represents smooth model, dotted line two-phase model with $\sigma = 100$, dashed two-phase model with $\sigma = 12.5$ and dashed-dotted clumps-only model with $\sigma = 12.5$. All other parameters are the same as in Fig. 2.6. Left panel: face-on view; right panel: edge-on view.

2.4.9 Comparison between two-phase and smooth models

In this section we present investigation of differences between models with homogeneous dust distribution (smooth models) and models with dust as a two-phase medium. In order for this comparison to be as consistent as possible, for each two-phase model we have generated its corresponding smooth configuration, using the same global physical parameters. Furthermore, we have generated two different sets of two-phase models using a relative clump size (see Eq. 2.11) value of $\sigma = 100$ and $\sigma = 12.5$, respectively: in the latter case, the clumps are eight times bigger than in the former.

We found that two-phase models with $\sigma = 100$ (small clumps) tend to have a less pronounced emission in the $1 - 6\,\mu$m range, when compared to the smooth ones. If we compare the intensity of the $10\,\mu$m silicate feature, we find virtually no difference in type 1 view, while slightly lower absorption is measured in two-phase SEDs for the type 2 lines of sight. As expected, the dust distributed in a large number of small clumps, embedded in a smooth, homogeneous medium, will closely resemble the characteristics of a smooth SED.

Two-phase models with bigger clumps ($\sigma = 12.5$) are showing more difference compared to both smooth and $\sigma = 100$ models. In the face-on view, they tend to have even less pronounced emission and also a different, flatter, slope in the $1 - 6\,\mu$m range. Depending on the parameters of the dust distribution and on the optical depth, the silicate feature is in general less pronounced. This behavior can be attributed to the shadowing effect caused by the clumps in the innermost region, where the dust is hotter and the feature is produced. In the edge-on view, the silicate band absorption is less deep compared to both smooth and $\sigma = 100$-models because we are able to see between clumps deeper in the torus. Fig. 2.16 presents a comparison of SEDs of typical models with the smooth and the two-phase dust distributions for the two sizes of clumps.

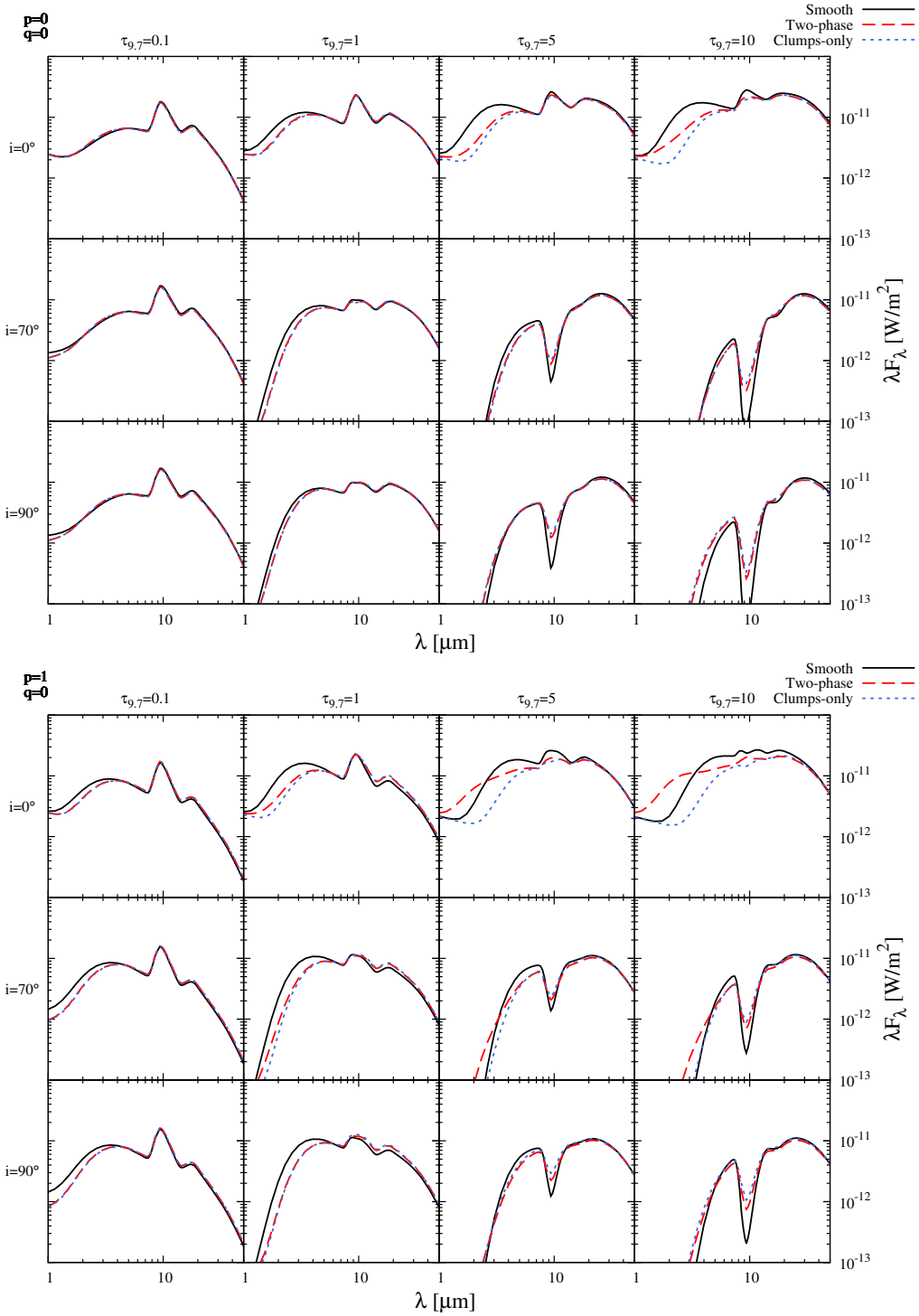

Figure 2.17 SEDs of our standard model grid, in the $1-50$ μm wavelength range. Solid line: smooth models; dashed line: two-phase models; dotted line: clumps-only models. The columns correspond to optical depths of $\tau_{9.7} = 0.1, 1, 5, 10.0$, from left to right. The rows correspond to inclinations of $i = 0, 70, 90°$, from top to bottom. The dust distribution parameters (p and q) are given in the top left corner of each panel.

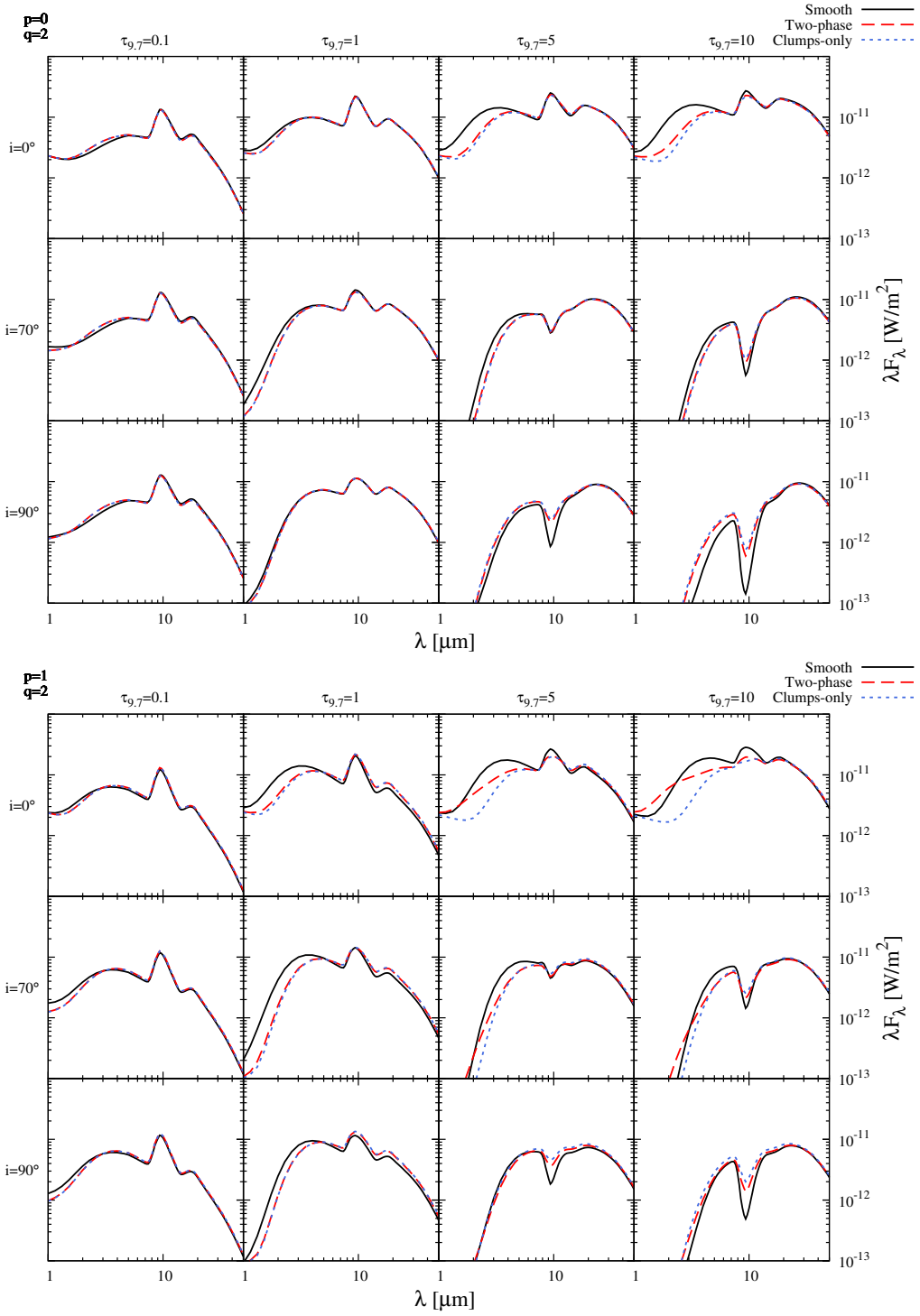

Figure 2.17 - *continued*

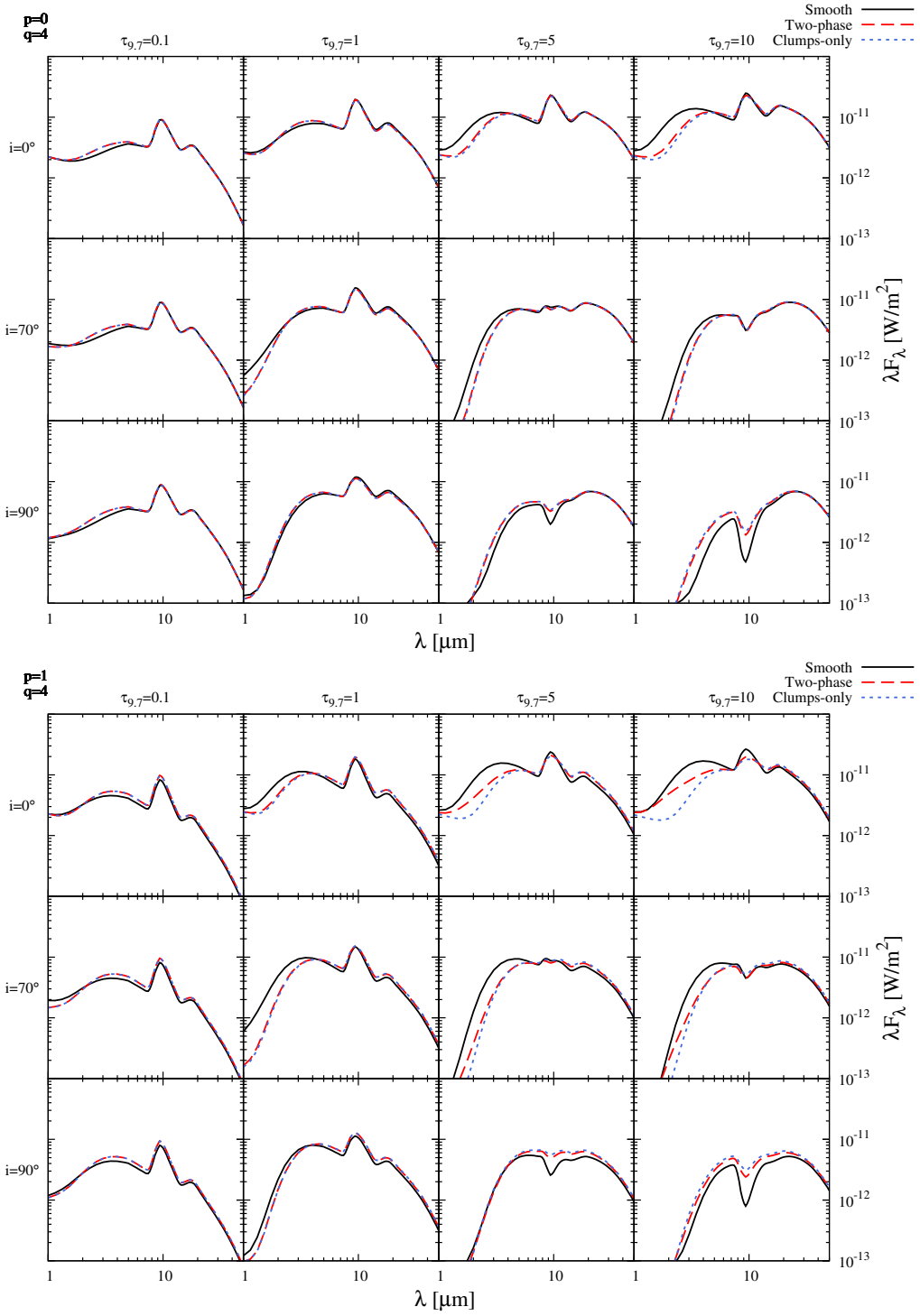

Figure 2.17 - *continued*

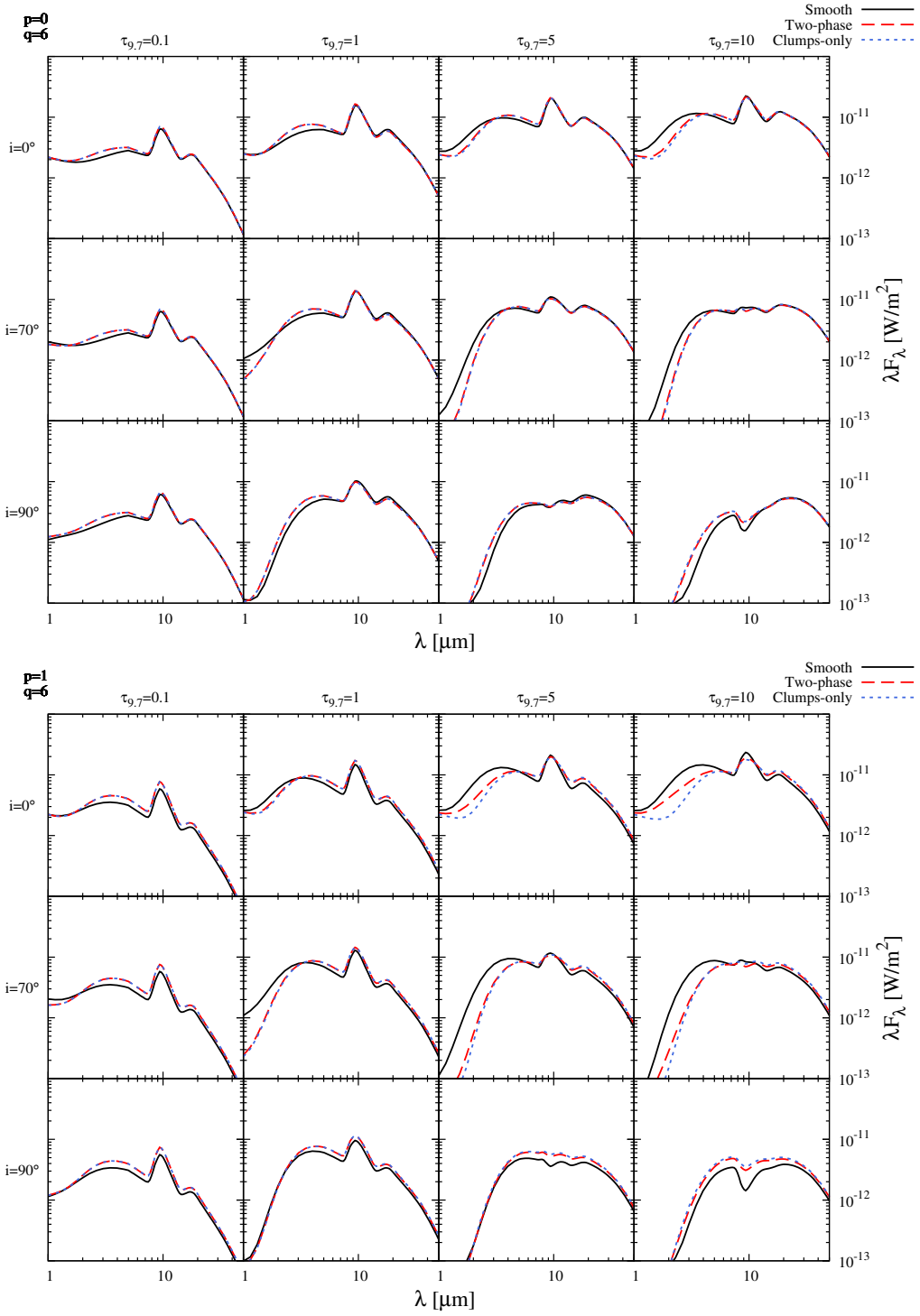

Figure 2.17 - *continued*

For the face-on view, although both smooth and two-phase models are able to produce almost the same range of values of the silicate feature strength, two-phase models tend in general to produce an attenuated emission compared to those produced by the corresponding smooth models. The majority of both smooth and two-phase model SEDs have their infrared emission maximum around $\sim 9.4\,\mu$m. However, while no smooth model peaks beyond $12\,\mu$m, there are several two-phase models that peak around $\sim 20\,\mu$m. This is because the two-phase models tend to produce an attenuated silicate emission feature, and when it is very weak or absent, the peak of the emission is shifted toward the longer wavelengths. In the edge-on view, the two-phase models produce a weaker silicate absorption feature, with the lowest strength around -2.4. The smooth models produce a deeper silicate feature, with the strength value reaching a minimum of -4.4.

Two more characteristics which are of interest when comparing smooth and two-phase models, are the isotropy of the infrared emission and the SED width (see sec. 2.4.7 and 2.4.6 for definitions). Both two-phase and smooth models produce a similar range of values of the isotropy parameter I. However, compared individually, two-phase models are more isotropic than the smooth ones. Regarding the SED width, W, we found that clumpiness does not have a profound effect on this parameter.

In Fig. 2.17 we present plots of SEDs covering our standard parameter grid, for three characteristic inclinations (0°, 70°, 90°). This figure illustrates how SEDs of smooth, two-phase and clumps-only models compare to each other and evolve with the different parameters, i.e. inclination, optical depth and the two parameters determining the dust distribution. In models with a low optical depth, the silicate feature appears in a strong emission and the difference between smooth and clumpy models is marginal. With increasing optical depth the difference is increasing as well. Also, the difference between smooth and clumpy models is greater in the cases of the constant dust density along the polar angle ($q = 0$ in Eq. 2.6), and non-constant dust density in the radial direction ($p = 1$).

2.4.10 Comparison between two-phase and clumps-only models

As it can be seen from Fig. 2.17, the major difference between SEDs of two-phase and clumps-only models arises in the near-infrared range and mainly for the face-on view. At these wavelengths, the most of the two-phase models with the type 1 inclination have a flatter SED when compared to the corresponding clumps-only models. This difference is caused by the presence of the smooth component in which the clumps are embedded. Dust in this component, exposed to the radiation field of the central source, can reach high temperatures and will give rise to the higher luminosity in the $2-6\,\mu$m range.

Regarding the 10 μm silicate feature, we do not find any significant difference between the two dust configurations: depending on parameters, in clumps-only models it could be slightly

attenuated compared to the one in the two-phase models, but the difference is in the most cases marginal. A similar behaviour can be observed in SEDs of edge-on views, in which the smooth low density component is responsible for an additional absorption, so the silicate feature is slightly deeper in the two-phase models. The dissimilarities between SEDs in these two dust configurations increase as the optical depth increases: from models with the lowest value ($\tau_{9.7} = 0.1$), where SEDs are identical, to models with the highest value ($\tau_{9.7} = 10$) which display the most evident differences. The difference is the most pronounced in the cases of the constant dust density with the polar angle ($q = 0$), and non-constant dust density in the radial direction ($p = 1$).

It is very interesting to note that such a behaviour of the near- and mid-infrared SED of the two-phase dust distribution, would overcome an issue that seems to be common to the most clumpy models currently available in the literature. Exploiting the model of Nenkova et al. (2008b), Mor et al. (2009) fited a sample of mid-infrared spectra of 26 luminous quasar, finding the need of an extra hot-dust component, which they add to the clumpy torus SED, in order to properly reproduce the shorter wavelengths part of the *Spitzer* spectrum. The addition of this hot dust, whose emission is represented by a black-body with a temperature of about the sublimation limit of graphite, is required by the lack of emission from the adopted clumpy model at these wavelengths. More recently Deo et al. (2011), adopted the same clumpy model to reproduce a combination of the observed broad-band photometry and mid-infrared spectrum of 26 high redshift type-1 quasars. Similarly to Mor et al. (2009), the adopted clumpy models are not able to simultaneously reproduce the intensity of the silicate feature and the near-infrared continuum emission: models that would properly fit the continuum were overestimating the silicate feature emission. An analogous problem was also spotted by Vignali et al. (2011), when using the same clumpy models to fit the observed photometry and IRS spectrum of a $z \sim 0.44$ type-2 quasar. Adopting the clumpy models developed by Hönig et al. (2006), to fit both photometry and mid-infrared spectroscopy data, Polletta et al. (2008) reached similar conclusions.

As we have shown, a torus model with the dust distributed in a two-phase medium, has a more pronounced ('hotter') emission in the $2 - 6$ μm range while displaying, at the same time, a silicate feature whose intensity is almost identical to that of the corresponding clumps-only model. This is further validated by Roseboom et al. (2012). They considered the optical to mid-IR properties of a sample of quasars selected from a combination of the WISE, UKIDSS and SDSS datasets. They estimated a number of quasar properties, including the IR SED shape characterised by the ratio of near-IR ($1 - 5$ μm) to total IR luminosity. The typical ratio of the near-IR to the total IR luminosity in their sample is $\sim$ 40 %. They found that this ratio is achievable within Nenkova et al. (2008a) models only in a limited range of parameter values. On the other hand, in our set of models, they found that near-IR to total IR luminosity ratios similar to that in their observed sample are easily achievable.

2.4.11 Other results in the literature

Making a detailed comparison of our modeling approach with models previously developed in the literature and their results, is quite a tricky task, and is beyond the scope of our work. Furthermore, what we describe in this work is a model which would ideally put itself in between smooth and clumpy models approach, and it is hence not directly comparable to any of formerly published work. In this section we give a very brief description, which is by no means meant to be exhaustive, of some of the aforementioned works, limiting ourselves to models that consider a clumpy dust distribution.

The exploitation of radiative transfer codes to model the AGN IR emission, taking into account the clumpy nature of the dust surrounding the central source, includes at present only few works: Nenkova et al. (2002, 2008a,b), Dullemond & van Bemmel (2005), Hönig et al. (2006); Hönig & Kishimoto (2010), Schartmann et al. (2008) and Kawaguchi & Mori (2011). Each of these works exploits different techniques and approximations.

In their series of works, Nenkova et al. used the radiative transfer code `DUSTY` (Ivezić & Elitzur, 1997) to solve the radiative transfer equation for the single clouds, that where modeled as an 1-D dust slab. The final torus SED was obtained by adding the emission from different slabs at different viewing (phase) angles, after statistically weighting them. They find that 5 to 15 clumps in an equatorial line of sight, each with an optical depth in the range $\tau_V \sim 30 - 100$, are successful in reproducing the observed characteristics of AGNs. Models in which clouds are more concentrated at shorter distances from the central source, i.e. with a radial distribution following a power low, are favoured.

Another approach was followed by Dullemond & van Bemmel (2005), who exploit a 2-D Monte-Carlo code, in which clumps where modeled as concentrical rings. Once the temperature of the dust is known throughout all cells, the torus SED is calculated by means of ray tracing techniques. Starting from models with dust continuously distributed, they calculate the respective clumpy models, finding that it is not possible to use observed infrared data to distinguish between the effects due to the two different distributions.

The model developed by Hönig et al. (2006) and its further development (Hönig & Kishimoto, 2010), also adopts a Monte-Carlo technique to solve the radiative transfer problem, calculating the SEDs for various phase angles, for each cloud, setting up in this way a database of the clump emission. They consider that both the clouds optical depth and their size (radius) are related to their distance from the central source. The clouds are then randomly displaced, according to a spatial distribution function, and the torus SED is calculated by summing the emission of directly and non-directly illuminated clumps. This approach also allows them to study the dependence of the dust SED on the arrangement of the clouds: relevant differences are found especially for intermediate angle line of sights.

Monte-Carlo, coupled to ray tracing techniques, was used by Schartmann et al. (2008). They

were not using any prescription for the dust distribution which is instead computed from the equilibrium between the gravitational potential and pressure forces. They explore the effect of the filling factor, of changing the dust mass, of the clump size and their positions. Again, their analysis of the SED for different arrangements of the clumps, shows non-negligible differences which tend to be the highest for the edge-on views. The case of a non–isotropically emitting central source, whose emission is varying according to a $|\cos(\theta)|$ law, was also studied by Schartmann et al. (2005), but their results are not directly comparable to ours since in their case the dust was continuously distributed.

2.5 Conclusions

In this chapter we presented our investigation of the infrared emission of AGN dusty tori. Following theoretical predictions coming from hydrodynamical simulations, we modeled the dusty torus as a 3D two-phase medium with high-density clumps and low-density medium filling the space between the clumps. We employed a 3D radiative transfer code based on the Monte Carlo technique to calculate SEDs and images of torus at different wavelengths. We calculated a grid of models for different parameters and analyzed the properties of the resulting SEDs. For each two-phase model we have calculated two corresponding models with the same global physical parameters: a clumps-only model and a model with a smooth dust distribution. For both two-phase and clumps-only models, another set is generated keeping all the parameters constant but varying the random distribution of the clumps. From the analysis of the SED properties and comparison of the corresponding models, we conclude the following (Stalevski et al., 2011, 2012a):

(i) The SED at the near- and mid-infrared wavelengths is determined by the conditions of dust in the innermost region of the torus: different random distributions of the clumps may result in the very different SEDs in otherwise identical models.

(ii) The shape of the silicate feature is not only a function of the torus inclination. Optical depth, dust distribution parameters, clump size and actual arrangement of clumps, all have an impact on the appearance of the silicate feature. Low optical depth tori produce silicate feature in a strong emission. Models with high-density clumps occupying the innermost region will have the emission feature attenuated due to the shadowing effects.

(iii) The clump size has a major impact on the SED properties. SEDs of the clumpy models with small clumps ($\sigma = 100$ or clump size of 0.15 pc) are very similar to the ones obtained by a homogeneous distribution of the dust. The silicate feature in absorption in these models is shallower and they tend to have less near-infrared emission than the corresponding smooth models. However, the silicate feature in emission is not suppressed. Clumpy models with bigger clumps ($\sigma = 12.5$ or clump size of 1.2 pc) are showing more differences compared to both small clump and smooth models. The silicate feature in absorption in these models is even less deep and they have less near-infrared emission than the small clump and smooth models. The silicate feature in emission is in general less pronounced. We stress that suppression strongly depends on the dust distribution parameters. The effect is the most notable in the case of a non-constant density in the radial direction and constant density in the polar direction ($p = 1$, $q = 0$); as q is allowed to increase the effect is weaker or even absent.

(iv) Although the silicate emission feature could be suppressed in the clumpy models for certain parameters, the smooth models are able to reproduce almost the same range of the

silicate feature strength. Our analysis shows that, overall, when considering characteristics of the silicate feature, models with the three dust configurations (smooth, two-phase, clumps-only) are not distinguishable.

(v) The low density dust, smoothly distributed between the clumps in the two-phase model, significantly contributes to the near-infrared emission in the type 1 view. This is the main difference with respect to the clumps-only models that typically show a deficiency in this range. This peculiar characteristic of the two-phase models might represent a possible solution to a similar issue found when fitting observed SED with currently available clumpy models from the literature.

A grid of model SEDs calculated for this study, in the form of `ascii` files are available on the following address (see Stalevski, 2012c, for more details): `https://sites.google.com/site/skirtorus/` . Images, in the form of `fits` files are available upon request.

3 Gravitational microlensing of AGN dusty tori

3.1 Introduction

Infrared spectra of most quasars are dominated by thermal emission from hot dust in their tori, with possible addition of non-thermal synchrotron emission from the regions near their central black holes (Agol et al., 2000). Variability in the infrared band due to gravitational microlensing could be used to constrain the size and structure of the infrared emission region, and hence to distinguish between the thermal and synchrotron mechanisms. If the infrared radiation varies on timescales shorter than decades, then its emission region is smaller, located closer to the central black hole, and its emission is non-thermal, while longer time-scales indicate a larger, thermal region (Neugebauer & Matthews, 1999). Additionally, chromatic effects in the infrared band have been observed in some of the lensed quasars, where the color differences between their multiple images were detected (Yonehara et al., 2008). The most realistic scenario that can explain the observed color differences is gravitational microlensing, in contrast to the dust extinction and the intrinsic variability of quasars (Yonehara et al., 2008).

Some previous theoretical and observational studies suggested that the infrared emission of quasars is not significantly affected by microlensing, implying that it is most likely produced in their dusty tori. For instance, Agol et al. (2000) studied the mid-IR emission of Q2237+0305 observed by Keck and found that it was not affected by microlensing, which ruled out the synchrotron mechanism and supported the model with hot dust extended on a length scale of more than 0.03 pc. Wyithe et al. (2002) used mid-IR and V-band flux ratios for images A and B of Q2237+0305 to infer the size of the mid-IR emission region and found that it was comparable to or larger than the Einstein Ring Radius (ERR) of the microlens, and hence at least two orders of magnitude larger than the optical emission region. They used simple Gaussian and annular intensity profiles of the dusty torus and found that the results were dependent on the assumed source profile (Wyithe et al., 2002). Recent Spitzer observations of the same gravitationally lensed quasar (Agol et al., 2009) showed that a dusty torus model with a small opening angle could satisfactorily explain the shape of the observed infrared SED, excluding an offset in wavelength of the silicate feature. However, the same authors found that the near-IR fluxes are increasingly affected by microlensing toward shorter wavelengths and that this wavelength dependence is consistent with a model in which a dusty torus and an accretion disk both contribute to the infrared radiation near 1 μm (Agol et al., 2009).

In this chapter we present simulations of gravitational microlensing of AGN dusty tori in the infrared domain. We consider microlensing by stars in the lens galaxies, in the case of lensed quasars. For generating microlensing magnification maps, a ray-shooting method was used (Kayser et al., 1986; Schneider & Weiss, 1986, 1987; Wambsganss et al., 1990). We simulated microlensing magnification events for different configurations of the lensed system and different values of the torus parameters. The aims of this investigation are to estimate: (a) amplitudes

and timescales of high magnification events, and (b) the influence of geometrical and physical properties of dusty tori on microlensing light curves in the infrared domain.

In this chapter, in Section 3.2 we first provide a description of the method we used to calculate microlensing magnification map and the parameters we adopted in this study. We present and discuss the results of simulated microlensing light curves of the dusty torus in Section 3.3. In Section 3.4 we outline our conclusions. The work presented in this chapter has been published in Stalevski et al. (2012b).

3.2.1 Microlensing magnification map

Different mirolensing models can be used for explaining the observed microlensing phenomena in quasars, such as microlensing by an isolated compact object (Chang & Refsdal, 1979, 1984), or by a number of microdeflectors located within an extended object – the model called "straight-fold caustic" (Schneider, Ehlers & Falco, 1992). However, the most realistic model is the so-called microlensing map (pattern) or caustic network which is usually applied in order to obtain a spatial distribution of magnifications in the source plane (where the dusty torus of quasar is located), produced by randomly distributed stars in the lensing galaxy (for more details see e.g. Schneider, Ehlers & Falco, 1992). The lensing galaxy can be assumed as thin when compared with the whole light path, since its extent in the direction of the optical axis is much smaller than the angular diameter distances between observer and lens, observer and source and lens and source. In such case the dimensionless lens equation reads (Schneider, Ehlers & Falco, 1992):

$$\boldsymbol{y} = \boldsymbol{x} - \boldsymbol{\alpha}\left(\boldsymbol{x}\right), \tag{3.1}$$

where $\boldsymbol{x}$ and $\boldsymbol{y}$ are normalized image and source positions, respectively, and $\boldsymbol{\alpha}\left(\boldsymbol{x}\right)$ is the deflection angle due to light banding in the gravitational field of the lens. The deflection potential is then given by:

$$\psi\left(\boldsymbol{x}\right) = \frac{1}{\pi}\int \kappa\left(\boldsymbol{x}'\right)\ln|\boldsymbol{x}-\boldsymbol{x}'|d^2x', \tag{3.2}$$

and it is related to the deflection angle by: $\vec{\alpha}\left(\boldsymbol{x}\right) = \nabla\psi\left(\boldsymbol{x}\right)$ and to the dimensionless surface mass density κ by the 2-dimensional Poisson equation: $\nabla^2\psi = 2\kappa$. For a field of point masses with an external shear γ and a smooth mass distribution κ_c, the normalized lens equation (3.1) is usually written as (Kayser et al., 1986):

$$\boldsymbol{y} = \sum_{i=1}^{N} m_i \frac{\boldsymbol{x}-\boldsymbol{x}_i}{|\boldsymbol{x}-\boldsymbol{x}_i|^2} + \begin{bmatrix} 1-\kappa_c+\gamma & 0 \\ 0 & 1-\kappa_c-\gamma \end{bmatrix}\boldsymbol{x}, \tag{3.3}$$

where the sum describes light deflection by stars with masses m_i and the last term is a quadrupole contribution from the lensing galaxy. The total surface mass density or convergence can be written as $\kappa = \kappa_* + \kappa_c$, where κ_* represents the contribution from the compact microlenses. The magnification map for some specific microlensing event can be generated if the following two parameters are known: the convergence – κ, and the shear due to the external mass – γ.

For generating microlensing magnification maps we used a ray-shooting method (Kayser et al., 1986; Schneider & Weiss, 1986, 1987; Wambsganss et al., 1990; Shalyapin, 1995). In this method, rays are followed backwards from the observer through the lens plane, to the source

plane. First, a random star field in the lens plane based on the parameter κ is generated. After that, the Poisson equation $\nabla^2\psi = 2\kappa$ is solved in the lens plane numerically, so the the lens potential ψ can be determined in every point of the grid in the lens plane. To solve the Poisson equation numerically one has to write its finite difference form:

$$\psi_{i+1,j} + \psi_{i-1,j} + \psi_{i,j+1} + \psi_{i,j-1} - 4\psi_{i,j} = 2\kappa_{i,j}. \tag{3.4}$$

Here we used the standard 5-point formula for the two-dimensional Laplacian. The next step is the inversion of equation (3.4) using Fourier transforms. After some transformations we obtain:

$$\hat{\psi} = \frac{\hat{\kappa}_{mn}}{2(\cos\frac{m\pi}{N_1} + \cos\frac{n\pi}{N_2} - 2)}, \tag{3.5}$$

where N_1 and N_2 are dimensions of the grid in the lens plane. Now, using the finite difference technique, we can compute the deflection angle $\vec{\alpha} = \nabla\psi$ in each point of the grid in the lens plane. After computing the deflection angle, we can map the regular grid of points in the lens plane, via lens equation, onto the source plane. These light rays are then collected in pixels in the source plane, and the number of rays in one pixel is proportional to the magnification due to microlensing at this point in the source plane. Due to the relative motion between the observer, lens and source, the magnification over time will change, and a light curve for a small, pointlike source can be found by tracing a path across the magnification map.

Apart from the convergence κ and shear γ, another input parameter is size of the microlensing magnification map expressed in units of the Einstein ring radius in the source plane. The Einstein ring radius in the lens plane It is defined as

$$\mathrm{ERR} = \sqrt{\frac{4Gm}{c^2}\frac{D_\mathrm{l}D_\mathrm{ls}}{D_\mathrm{s}}}, \tag{3.6}$$

and its projection in the source plane is:

$$R_\mathrm{E} = \frac{D_\mathrm{s}}{D_\mathrm{l}}\mathrm{ERR} = \sqrt{\frac{4Gm}{c^2}\frac{D_\mathrm{s}D_\mathrm{ls}}{D_\mathrm{l}}}, \tag{3.7}$$

where G is the gravitational constant, c is the speed of light, m is the microlens mass and D_l, D_s and D_ls are the cosmological angular diameter distances between observer and lens, observer and source and lens and source, respectively.

3.2.2 Parameters

Microlensing magnification map

The microlensing magnification map is calculated for typical values of average surface mass density and shear, $\kappa = \gamma = 0.4$. The map has 1156 $R_{\rm E}$ on a side. For a source fixed at redshift of $z_{\rm s} = 2$, and for the lens at $z_{\rm l} = 0.05$ and 0.5, this is equal to 61.42 and 19.99 pc in the source plane, respectively. The size of the map is chosen because of the large dimensons of the dusty torus compared to $R_{\rm E}$. But this particular value is also chosen for numerical reasons – the pixel size has to be the same in the images of the torus and the magnification map. Thus, the size and resolution of the images of the torus and the magnification map cannot be choosen independently. The mass of microlens is taken to be $1 M_{\odot}$ in all simulations.

The dusty torus

The details of the dusty torus model are given in Chapter 2. Here we will only provide an overview of the adopted values of the parameters we used in the study of microlensing.

For the bolometric luminosity of the primary source (accretion disk) we adopted the value typical for quasars, 10^{12} $L_{\odot}$ (e.g. Davis & Laor, 2011). According to the Eq. (2.5), assuming a dust sublimation temperature of 1500 K, the corresponding value of the inner radius of the torus is $R_{\rm in} = 0.8$ pc. Recent observations of nearby AGN suggest that the size of tori is likely restricted to several parsecs (Alonso-Herrero et al., 2011; Ramos Almeida et al., 2011). It is arguable whether this holds also for the tori in AGNs at much larger redshifts (i.e. quasars). Preliminary results from a recent study of high redshift quasars by Leipski & Meisenheimer (2012) suggest that hot dust properties do not change significantly with either redshift or luminosity. Therefore, for the outer radius of torus we adopted the values of 3 and 10 pc. The half opening angle of the torus takes values of 30°, 50° and 70°. For the dust density distribution parameters we adopted the following values: $p = 0, 0.5, 1$ and $q = 0, 1, 2$. The relative clump size, defined as the ratio of the outer radius of the torus over the clump size, is $\xi = 12.5$. The equatorial optical depth (determining also the total amount of dust) is fixed at $\tau_{9.7} = 5$. We calculated each model at three inclinations, $i = 0°, 70°, 90°$, where $i = 0°$ corresponds to the face-on view (type 1 AGN), and $i = 90°$ to the edge-on view (type 2 AGN). The emission for all models is calculated on an equally spaced logarithmic wavelength grid ranging from 0.001 to 1000 μm.

3.3 Results and discussion

In this section, we first present the microlensing magnification map used in this study and demonstrate the wavelength dependency of the AGN dusty torus size. Then, the size of the torus is taken into account by convolving the magnification map with images of torus at different wavelengths. Finally, we discuss light curves of simulated magnification events, the amplitudes and timescales of these events, and the influence of different torus parameters. Note that we always refer to the rest-frame wavelengths.

We calculated microlensing light curves for a source fixed at a redshift of $z_s = 2$, while the lens galaxy redshift takes values of $z_l = 0.05$ and 0.5. The former value of lens galaxy redshift ($z_l = 0.05$) roughly replicates the well-known lensed system Q2237+0305 (also known as the "Einstein cross"), which is particularly susceptible to microlensing. The redshift of the lens in this system ($z_l = 0.04$) is so low that the apparent angular velocity of the microlenses, in projection on the plane of the sky, is much higher than in other systems. Moreover, the Einstein rings of these microlenses have a larger angular diameter, making it more likely that they are larger than the source (Courbin et al., 2002). The second value chosen for calculation of magnification map ($z_l = 0.5$) represents a more typical value of lens galaxy redshift in lensed systems.

The microlensing magnification map shown in Fig. 3.1 is calculated for the case of $z_l = 0.05$ (and other parameters as described in Section 3.2.2). The left panel represents the whole map, with $\sim$ 61.42 pc (1156 R_E) on a side; for comparison, the sizes of the tori used in this study ($R_{out} = 3$ and 10 pc) are indicated with two white circles. The right panel is a zoom-in of the region with a side of 12 pc, from which the light curve of the microlensing events is extracted (vertical white line). The distribution of magnification is highly non-liner, with regions of low and high magnification and with a maximum magnification along the sharp caustic lines. Magnification pattern is color coded, with blue, cyan, yellow, orange and red regions corresponding to increasingly higher magnification. When a source crosses a caustic, a large change in magnification is expected.

3.3.1 Wavelength dependence of the torus size

In the top row of Fig. 3.2 we present images of the torus at different wavelengths. At shorter wavelengths, it is the radiation from the inner (and hotter) region that dominates. Thus, at the near-infrared wavelenghts, the torus appears much more compact compared to its physical outer radius. On the other hand, at longer wavelengths, the emission arises from the colder dust. As this colder dust is placed further from the centre, all the way to the outer radius, the torus will appear larger at longer wavelenghts. Therefore, the size of torus is wavelength dependent, as seen in the top row Fig. 3.2.

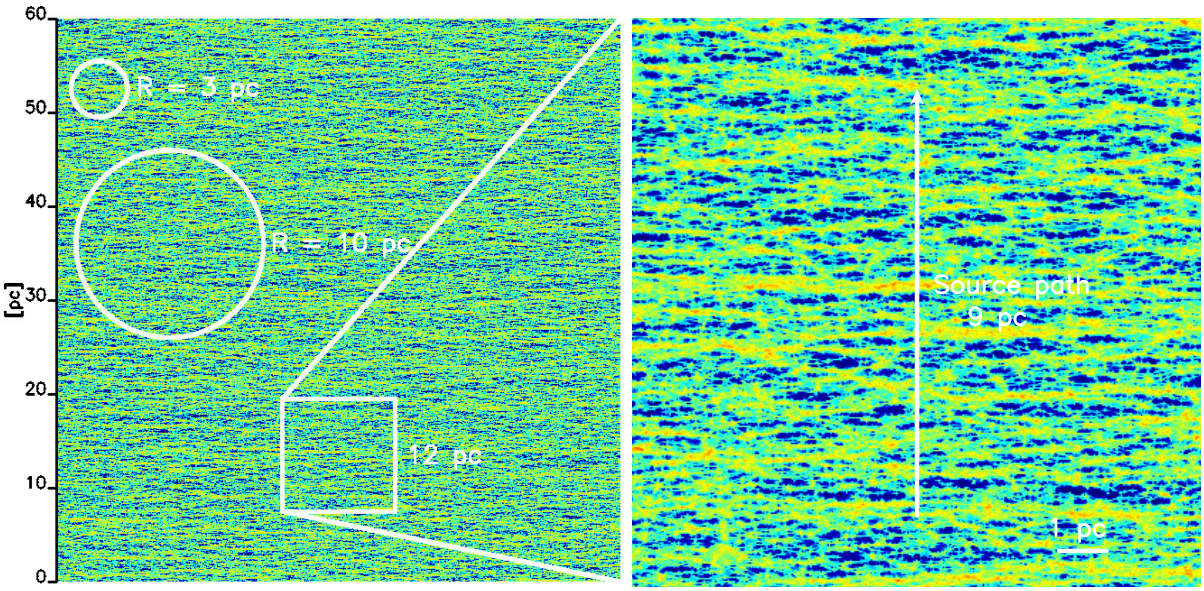

Figure 3.1 *Left panel:* Microlensing magnification map, with 61.42 pc (1156 $R_{\rm E}$) on a side. The average surface mass density and shear take value of $\kappa = \gamma = 0.4$. White circles indicate sizes of torus used in this study ($R_{\rm out} = 3$ and 10 pc). *Right panel:* zoom-in on the square with 12 pc on a side, from which the light curve of microlensing event is extracted (vertical white line).

The microlensing magnification maps are calculated for point sources. As the dusty torus is larger than the typical size of microlens $R_{\rm E}$, they have to be treated as extended sources. To take this into account, the magnification map shown in Fig. 3.1 is convolved with the images of the torus at the different wavelenghts. The bottom row of Fig. 3.2 shows the magnification maps after convolution with the corresponding torus images from the top row.

3.3.2 Simulated microlensing light curves

Wavelength dependence

In Fig. 3.3 we present light curves of magnification events at different wavelengths. The light curves are extracted from the magnification maps convolved with the corresponding images of the torus, along the path shown in the right panel of Fig. 3.1 (starting from bottom, going to the top). The parameters of the torus are the same as taken in Fig. 3.2. The left panel of Fig. 3.4 illustrates the dependence of the absolute magnification amplitude on wavelength, for the prominent high magnification events (HMEs), peaking at ~ 3.3 and ~ 2.3 pc (indicated with a dotted line in the left and right panel of Fig. 3.3, respectively). From these figures we see that, as a consequence of the wavelength dependency of the torus size, the magnification amplitude of the microlensing events is also wavelength dependent. The magnification is highest at near-infrared wavelengths, decreasing toward the mid-infrared range, and remains almost constant in the far-infrared part of the SED. Note that, as the torus size is larger than the typical size of

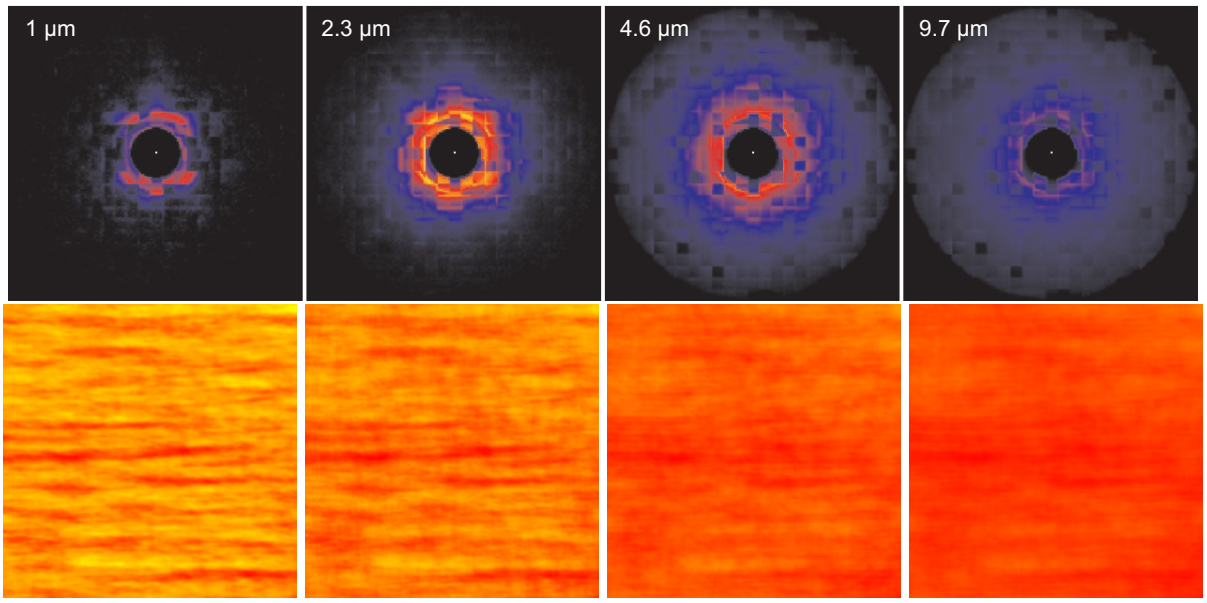

Figure 3.2 *Top row:* images of torus at different wavelengths, face-on view. From left to right, panels represent model images at 1, 2.3, 4.6, and 9.7 μm. All images are given in the same, logarithmic color scale. The visible squared structure is due to clumps which in our model are in the form of cubes. The adopted values of torus model parameters are: optical depth $\tau_{9.7} = 5$, dust distribution parameters $p = 1$ and $q = 2$, the half opening angle $\Theta = 50°$, the relative clump size $\xi = 12.5$, the inner and outer radius $R_{\rm in} = 0.8$ and $R_{\rm out} = 3$ pc, respectively. *Bottom row:* microlensing magnification maps after convolution with the corresponding images of the torus from the top row. Maps correspond to the region shown in the right panel of Fig. 3.1. For clarity, a different scale of coloring for each map is adopted, so that the details of each image are visible.

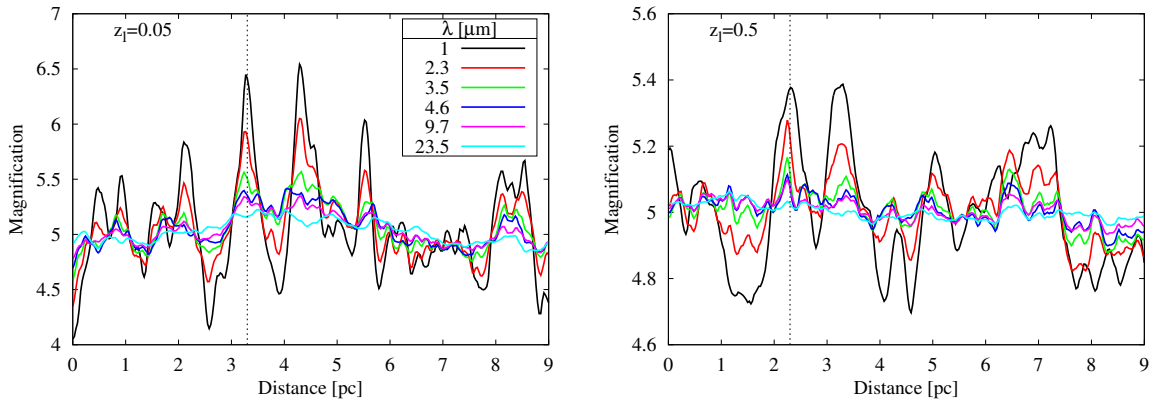

Figure 3.3 Light curves of magnification events at different rest-frame wavelengths (indicated in the legend), extracted from magnification maps convolved with the corresponding images of the torus. *Left panel:* $z_l = 0.05$. *Right panel:* $z_l = 0.5$. Note the different range of y axis shown in the two panels. The dotted line in both panels indicates two HMEs referenced throughout the text. The distance given in the x axis represents the distance crossed by the source, relative to the caustics, for the given values of the source and lens redshifts. The value "0" corresponds to the beginning of the path from which the lightcurve was extracted.

microlens $R_{\rm E}$, its radiation will always be magnified by a certain factor. Therefore, in the right panel of Fig. 3.4 we also illustrate the amplitudes relative to the minimum, i.e. to the beginning of a HME.

We note here that, at the near-infrared wavelengths, the accretion disk radiation may still have a significant contribution to the SED. As the accretion disk is much smaller than the typical size of $R_{\rm E}$, it can lead to microlensing events of much higher amplitudes and shorter timescales. However, in this work we investigate only the long-term variations caused by microlensing of the dusty torus; microlensing of the accretion disk has been throughly studied in the literature (e.g Jovanović et al., 2008; Blackburne & Kochanek, 2010; Morgan et al., 2010; Dexter & Agol, 2011)

Dependence on the torus parameters

The parameters that determine the viewing angle, the torus size, the dust distribution and the primary source luminosity, directly or indirectly, all contribute to the pattern of the torus IR emission and its apparent size at the given wavelength (Stalevski et al., 2012a). Therefore, each of these parameters could affect the shape and amplitudes of microlensing light curves. We adopted a set of parameter values as the standard ($p = 1, q = 2, \Theta = 50°, R_{\rm out} = 3$ pc, $L = 10^{12}\ L_{\odot}$) and then we varied each of these parameters, while keeping the others constant. The resulting microlensing light curves for simulated magnification events at 1 μm are shown in Fig. 3.5.

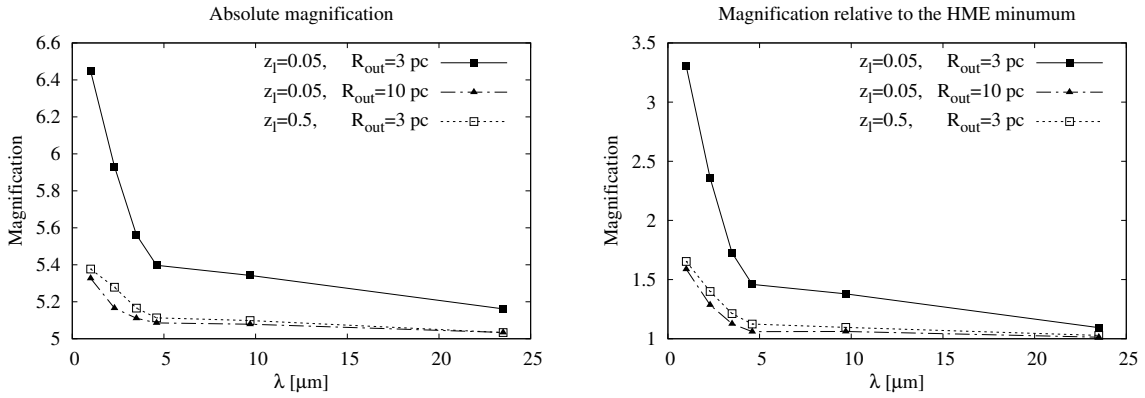

Figure 3.4 Magnification amplitude as a function of rest-frame wavelength, for prominent HMEs seen in Fig. 3.3. Full squares: HME peaking at $\sim$ 3.3 pc in left panel of Fig. 3.3 ($z_{\rm l} = 0.05$). Triangles: HME peaking at $\sim$ 2.3 pc in the right panel of Fig. 3.3 ($z_{\rm l} = 0.5$). Empty squares: the same as for the full squares, but for larger value of torus outer radius. *Left panel:* absolute magnification amplitude. *Right panel:* magnification amplitude relative to the minimum (beginning of the HME).

The outer radius of the torus has the largest impact on the magnification amplitude (see Fig. 3.4). Obviously, for smaller torus sizes, the magnification will be higher. The half opening angle (Θ) is another parameter which defines the size of torus, especially when seen edge-on. As expected, the tori with smaller opening angle will show larger variations under influence of microlensing.

It is evident that the viewing angle (inclination i) also has a significant influence. The dust-free lines of sight (corresponding to the type 1 AGN; $i = 0°$) provide a direct view of the innermost region of very hot dust, which is obscured in the case of dust-intercepting lines of sight (type 2 AGN; $i = 70, 90°$). Thus, in the former case, the larger part of the emission we see is originating from a more compact region than in the latter case. As a result, the amplitudes of magnification events will be higher in the case of type 1 objects (note that most of the lensed quasars are of type 1).

The parameters p and q define the spatial distribution of the dust density (see Eq. 2.6). The larger values correspond to the more compact distribution of the dust. However, from the panels in the bottom row of Fig. 3.5 we see that, although more compact dust configuration tend to have higher amplitudes, these parameters do not significantly influence microlensing light curves. This is because, for the adopted value of the primary source luminosity ($L = 10^{12}\ L_{\odot}$, typical for quasars), radiation is able to penetrate further into the dust, and thus diminish the difference between the compact and extended dust distributions. In the case of $\sim$ 10 times smaller primary source luminosities, we found that the dust distribution parameters do have a noticeable impact.

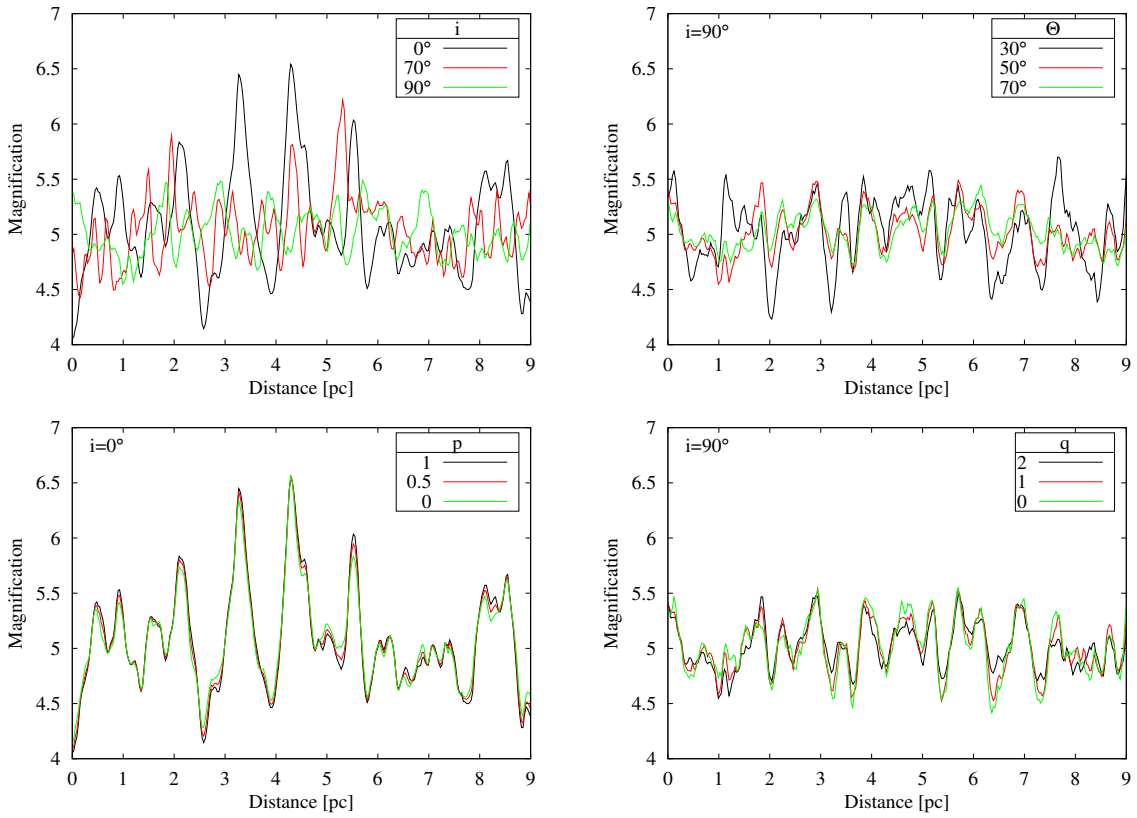

Figure 3.5 Microlensing light curves at 1 μm for the different parameters of the torus model. Upper left panel shows dependance on inclination, upper right panel on half opening angle, bottom panels on dust density distribution parameters. In all panels the black line corresponds to the most compact dust configuration, green line for the largest, and the red line for the intermediate.

Timescales of microlensing events

To characterize timescales of high magnification events, we use the rise time – the time interval between the beginning and the peak of a microlensing event. We estimate the rise time by measuring the distance traveled by the source, relative to the caustics, from the beginning to the peak of HME, and divide it by the effective source velocity. The effective source velocity V, i. e. the velocity of the source relative to the caustics with time measured by the observer is given by the expression (Kayser et al., 1986)

$$\mathbf{V} = \frac{1}{1+z_{\rm l}}\frac{D_{\rm ls}}{D_{\rm l}}\mathbf{v}_o - \frac{1}{1+z_{\rm l}}\frac{D_{\rm s}}{D_{\rm l}}\mathbf{v}_{\rm l} + \frac{1}{1+z_{\rm s}}\mathbf{v}_{\rm s}. \tag{3.8}$$

The source velocity $\mathbf{v}_{\rm s}$ and the lens velocity $\mathbf{v}_{\rm l}$ are measured in the source and lens plane, respectively, they are distance weighted, and, due to the redshifts, translated into the observer's frame. The transverse velocity of the observer $\mathbf{v}_o$ can be determined from the dipole term in the microwave background radiation. With an amplitude of 387 km/s (e.g., Kogut et al., 1993), the observer's motion will be important for some lenses and unimportant for others, depending on the direction towards the source. For simplicity, we will assume here that the direction of the observer's motion is parallel to the direction towards the source, so the first term in the Eq. (3.8) can be neglected. Assuming that the peculiar velocities of the source and lens, in their own planes, are of the same order, the last term can be neglected as well. With these approximations, the effective source velocity is reduced to the expression

$$V \simeq \frac{1}{1+z_{\rm l}}\frac{D_{\rm s}}{D_{\rm l}}v_{\rm l}. \tag{3.9}$$

In the case of lensed system Q2237+0305, several studies found the transverse velocity of the lens to be in the range between approximately 500 and 2000 km/s (Wyithe et al., 1999; Kochanek, 2004; Gil-Merino et al., 2005). We adopted three values in this range and calculated the corresponding effective source velocity and rise times of HMEs. In the Table 3.1, we present estimated rise times, in years, for the two prominent HMEs indicated in the Fig. 3.3 with a dotted line, for different values of lens redshift and transverse velocity of the lens. Depending on these parameters, the obtained rise times are in range from several decades to several hundreds of years.

Influence on the entire IR SED

In Fig. 3.6 we illustrate the influence of microlensing on the entire dusty torus SED in the 1–50 μm range. From this figure one can see that there is a significant difference in the amount of overall flux between the SEDs when microlensing is absent (solid line) and those under the influence of microlensing (dashed and dotted lines). However, due to the large size, the torus

Table 3.1 Rise times for HMEs, in years, calculated for different values of lens redshift and transverse velocity of the lens. Source is fixed at redshift $z_s = 2$.

	v_l [km/s]		
z_l	500	1000	2000
0.05	164	82	41
0.5	364	182	91

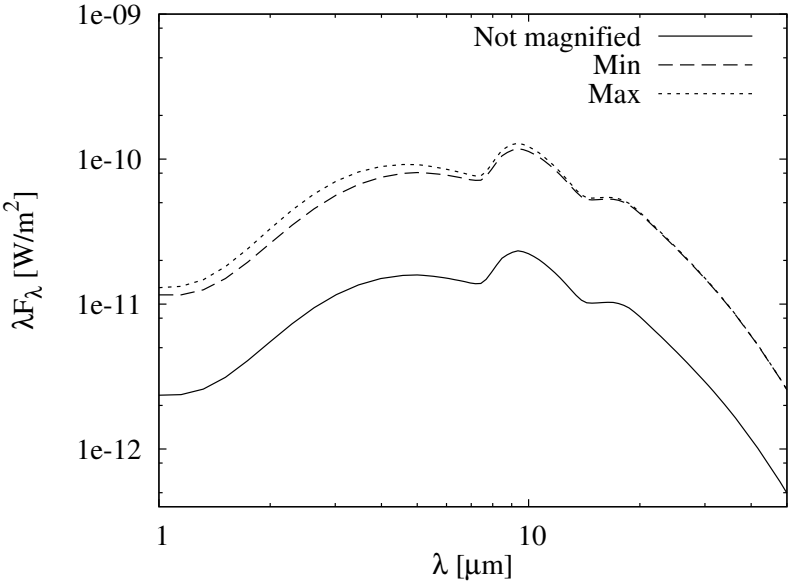

Figure 3.6 Dusty tori SEDs in 1–50 μm range. Solid line: not magnified. Dashed line: at the minumum of HME (at $\sim$ 2.6 pc in the left panel Fig. 3.3). Dotted line: at the maximum of HME (at $\sim$ 3.3 pc in the left panel Fig. 3.3). The parameters of the torus are the same as taken in Fig. 3.2.

will always cover a large area of a microlensing magnification pattern and it will always be magnified by a certain factor, so the difference between SEDs at the beginning (dashed line) and the peak (dotted line) of HME is marginal. Also, it is evident that microlensing does not change the shape of SED significantly.

3.4 Conclusions

We investigated gravitational microlensing of AGN dusty tori in the case of lensed quasars. We used our previously developed model of the dusty torus as a clumpy two-phase medium (see Sec. 2.3). The ray-shooting technique has been used to calculate microlensing magnification maps. Due to the large dimensions of dusty tori (compared to the Einstein ring radius of the microlens in the source plane), they must be treated as extended sources. Thus, images of the tori were convolved with the magnification maps. We simulated microlensing by stars in the lens galaxy, in the case of lensed quasars, for different configurations of the lensed system and different values of the torus parameters, in order to estimate (a) amplitudes and timescales of high magnification events, and (b) the influence of geometrical and physical properties of dusty tori on light curves in the infrared domain. From our investigation, we conclude the following (Stalevski et al., 2012b).

(i) Despite their large size, we found that AGNs dusty tori could be significantly magnified by microlensing in some cases. The amplitude of magnification depends on wavelenght, torus parameters, and configuration of the lensed system.

(ii) The size of torus is wavelength dependent. As a consequence, the magnification amplitude of microlensing events is also wavelength dependent. The magnification is the highest in the near-infrared, decreases rapidly towards the mid-infrared range, and stays almost constant in the far-infrared part of SED.

(iii) As microlensing is sensitive to the size of the source, parameters determining the geometry and apparent size of the torus, have a very important role. Tori with $R_{\rm out} \lesssim 10$ pc could be appreciably microlensed.

More compact dust configurations (e.g. steeper radial density profiles) result in smaller tori and thus in higher magnification amplitudes. However, for primary source (accretion disk) luminosites typical for quasars ($10^{12}\ L_{\odot}$), the influence of dust distribution parameters is diminished, because the radiation is able to penetrate deeper into the dust.

Tori seen at type 1 (dust-free) inclinations, which provide a direct view of the innermost, hottest region, are more magnified than those at type 2 (dust-intercepting) inclinations.

(iv) Lensed quasar systems with the lens galaxy closer to the observer, will have higher magnification amplitudes, owing to their larger Einstein ring radius projection on the source plane.

(v) Estimated rise times, between the beginning and the peak of HMEs, are in the range from several decades to several hundreds of years.

Given such long time-scales, microlensing would hardly prove to be a practical tool to study and constrain the properties of dusty tori, as it is in the case of AGN accretion disks. However,

the results presented above should be kept in mind when investigating the flux ratio anomaly of lensed quasar images in different wavelength bands. In such studies, it is important to determine the true flux ratios between the images, in the absence of microlensing. In principle, this could be done by looking at the emission-line, infrared, and radio-emitting regions of quasars, as they all should be large enough to safely disregard microlensing effects. However, we have shown that the infrared emission of the dusty tori could be significantly microlensed in some cases, and thus, it is a less reliable tool for determining the "intrinsic" flux ratios.

4 Non-axisymmetric perturbations of the accretion disk emissivity

4.1 Introduction

A huge amount of AGN energy is released through accretion onto a super-massive black hole in the center of AGN. The emission of the accretion disk is not only in the continuum, but also in the emission lines, such as Fe Kα line (see e.g. Jovanović, 2012), and in low ionization lines, as e.g. broad Balmer emission lines. The profiles of the broad emission lines are shaped by the kinematics and dynamics of the line-emitting gas. Sometimes, broad lines appear as double-peaked, what is regarded as the dynamical signature of an accretion disk, Namely, the line splits into two peaks because of the doppler shifting, as one side of the disk is approaching while the other is receding from an observer at a very high velocity (see examples in Fig. 4.1). DP Balmer lines are found in around 20% of radio loud AGNs at $z < 0.4$ (Eracleous & Halpern, 1994, 2003) and 4% of the Sloan digital Sky Survey (SDSS) quasars at $z < 0.33$ (Strateva et al., 2003).

Broad, double-peaked emission lines of AGNs provide dynamical evidence for presence of an accretion disk feeding a supermassive black hole in the center of AGN. But in some cases, the variability of these lines shows certain irregularities which could not be explained solely by standard model of accretion disk.

The DP line profiles are often used to extract the disk parameters (see e.g. Chen et al., 1989; Chen & Halpern, 1990; Eracleous & Halpern, 1994, 2003; Strateva et al., 2008; Eracleous et al., 2009). In a series of papers Dumont & Collin-Souffrin (see Collin-Souffrin, 1987; Collin-Souffrin & Dumont, 1990; Dumont & Collin-Souffrin, 1990a,b,c, and references therein) investigated the radial structure and emission of the outer regions of the optically thin accretion disks in AGNs and calculated detailed grid of photoionisation models in order to predict the relative strengths of low-ionization lines emitted from the disk. They obtained integrated line intensities and line profiles emitted at each radius of the disk, for its different physical parameters. They also studied the influence of the external illumination on the structure of the disk, considering the point source model, where a compact source of non-thermal radiation located at a given height illuminates the disk and the diffusion model, where the radiation of a central source is scattered back towards the disk by a hot diffusing medium. One of the first methods for calculating profiles of optical emission lines from a relativistic accretion disk was proposed by Chen et al. (1989). The limitation to this method is that the accretion disk structure required to explain the variability of the line profiles cannot be axisymmetric because very often it is observed that the red peak is higher than the blue. This cannot be explained by the circular disk model, since in this model the blue peak is always Doppler boosted to be stronger than the red peak. Therefore, Eracleous et al. (1995) adapted the circular accretion disk model to elliptical disks in order to fit the profiles of double-peaked emitters with a red peak stronger than the blue one. This model introduced eccentricity and phase angle parameters to the circular model described

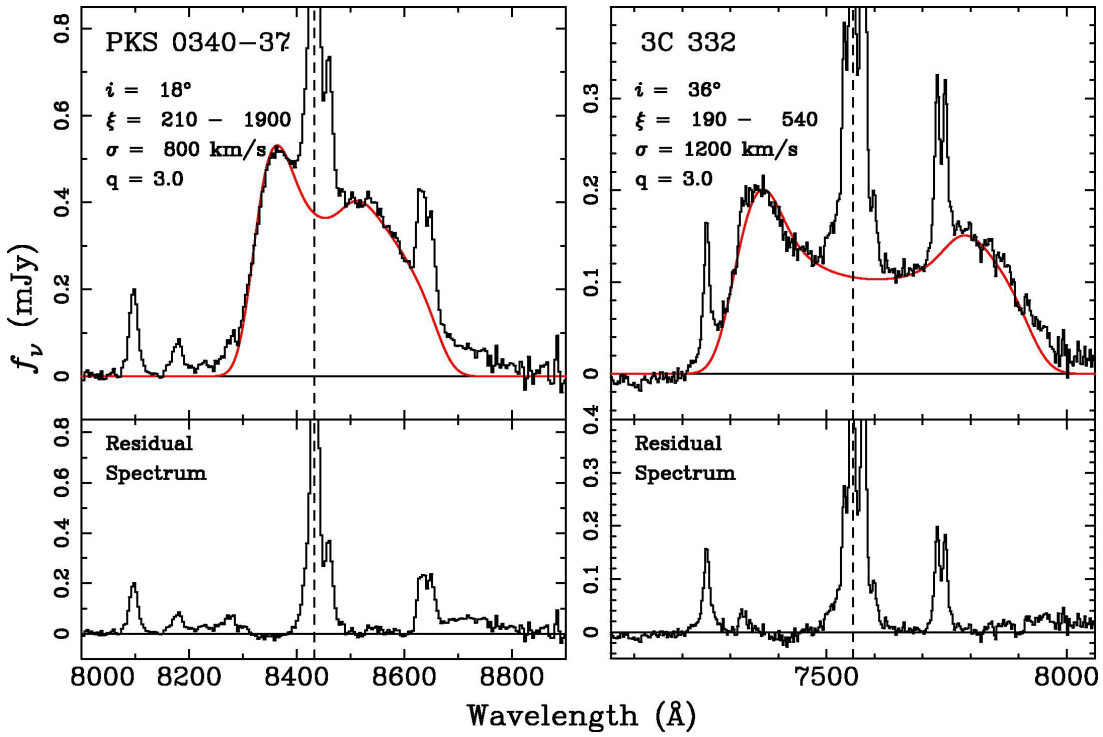

Figure 4.1 Examples of double-peaked emission line profiles (black line) with disk model fits (red line) superposed (Eracleous & Halpern, 1994).

above, and the pericenter distance of the elliptical orbits (see Eracleous et al., 1995).

Spectroscopic monitoring of double-peaked emitters (see e.g. Shapovalova et al., 2001; Gezari et al., 2007; Shapovalova et al., 2009, 2010) has revealed that an ubiquitous property of the double-peaked broad emission lines is variability of their profile shapes on the timescales of months to years. DP line profiles are observed to vary on timescales of months to years, i.e. on timescales of the order of the dynamical time or longer (e.g. Veilleux & Zheng, 1991; Zheng et al., 1991; Marziani et al., 1993; Romano et al., 1998; Sergeev et al., 2000; Shapovalova et al., 2001; Storchi-Bergmann et al., 2003; Gezari et al., 2007).

This slow, systematic variability of the line profile is on the timescale of dynamical changes in an accretion disk, and has been shown to be unrelated to the shorter timescale variability seen in the overall flux in the line, due to reverberation of the variable ionizing continuum. Patterns in the variability of the broad Balmer lines are often a gradual change and reversal of the relative strengths of the blue-shifted and red-shifted peaks (see e.g. Newman et al., 1997).

Periodic variability of the red and blue peak strengths has also been attributed to a precessing elliptical disk, a precessing single-armed spiral (as e.g. 3C 332, 3C 390.3: Gilbert et al., 1999; NGC 1097: Storchi-Bergmann et al., 2003), and a precessing warp in the disk. For instance, Wu et al. (2008) computed the profiles of Balmer emission lines from a relativistic, warped accretion disk in order to explore the certain asymmetries in the double-peaked emission line

profiles which cannot be explained by a circular Keplerian disk. Elliptical disks and spiral waves have been detected in cataclysmic variables (Steeghs et al., 1997; Baptista & Catalán, 2000), and a radiation induced warp has been detected in the large-scale disk of the AGN NGC 4258 (Maloney et al., 1996).

Spiral waves are a physically desirable model since they can be produced by instability in the vicinity of a black hole. They can play an important role in accretion disks, because they provide a mechanism for transporting angular momentum outward in the disk, allowing the gas to flow inwards, towards the central black hole. Long-term profile variability is thus a useful tool for extracting information about the structure and dynamics of the accretion disk most likely producing the double-peaked emission lines.

In this chapter, we present an investigation of the disk line variations due to instability in accretion disk. First we developed a model of emissivity perturbations in a form of a bright spot, assuming that instability in the accretion disk affects the disk emissivity. This model and some simulations of expected line profile variability are presented in Section 4.2. In Section 4.3 we compare the model with observations taken from long-term monitoring of 3C 390.3 (Shapovalova et al., 2001) in order to obtain parameters of perturbations. In Section 4.4 we discuss our results in the light of possible physical mechanisms which could cause such perturbations, and finally, in Section 4.3 we outline our conclusions. The work presented in this chapter has been published in Jovanović et al. (2010); Stalevski et al. (2010)

4.2 The model of the perturbation in the accretion disk

Here we introduce the model and some approximations used in the simulations of accretion disk perturbation.

4.2.1 Long term variation of double-peaked line profiles: some assumptions and problems

As we mentioned above, the DP line profile variability does not appear to correlate with changes in the line and/or continuum flux, and consequently one can assume that the changes in line profile are likely caused by changes in the accretion disk structure. There are several examples of the long-term variability (on timescales of several years) of the DP line profile of some objects that has been successfully modeled by the precession of a non-axisymmetric accretion disk, such as an elliptical disk or a disk with a spiral arm (Gezari et al., 2007; Storchi-Bergmann et al., 2003; Shapovalova et al., 2001; Gilbert et al., 1999, and references therein). These models, however, fail to explain the long-term variability of some objects and the short-term variability (on timescales from several months to a year) of all objects (Lewis, 2005; Lewis et al., 2010). For instance, Lewis et al. (2010) found that the two simple models, an elliptical accretion disk and a circular disk with a spiral arm, are unable to reproduce all aspects of the observed variability, although both account for some of the observed behaviors. Therefore, these authors suggested that many of the observed variability patterns could be reproduced assuming a disk with one or more fragmented spiral arms.

Other attempts to explain the DP line profile variability through perturbations of the disk structure introduced bright spots over an axisymmetric accretion disk. As an example Newman et al. (1997) successfully modeled the variation of the Hα peak intensity ratio of Arp 102B with a single spot rotating within the disk, but Gezari et al. (2007) were not able to apply the same model to the same object at a different time period (but see also Popović et al., 2001 for the discussion on possibility that the observed variations in Arp 102B are due to gravitational lensing).

In the case of Fe Kα variability Turner et al. (2006) used the spot model to explain the variability of the iron line profile of Mrk 766 in the X-ray band. Also, Dovčiak et al. (2008) studied variations of the iron line due to an orbiting spot which arises by reflection on the surface of an accretion disk, following its illumination by an X-ray flare in the form of an off-axis point-like source just above the accretion disk. Besides spots in the accretion disk, the Fe Kα line of some AGN could be also significantly affected by highly-ionized fast accretion disk outflows. For instance, Sim et al. (2010) found that major features in the observed 2 – 10 keV spectrum of the bright quasar PG1211+143 can be well reproduced by their Monte Carlo radiative transfer simulations which include a variety of disk wind (outflow) models.

To explain the short-timescale variability of the DP line profiles Flohic & Eracleous (2008) constructed stochastically perturbed accretion disk models and calculated Hα line profile series as the bright spots rotate, shear and decay. They ruled out spot production by star/disk collisions and favor a scenario where the radius of marginal self-gravity is within the line emitting region, creating a sharp increase in the radial spot distribution in the outer parts.

4.2.2 The model of a bright spot–like perturbing region

In the standard model of an AGN accretion disk, accretion occurs via an optically thick and geometrically thin disk. The effective optical depth in the disk is very high and photons are close to thermal equilibrium with electrons (Jovanović & Popović, 2009a). The spectrum of thermal radiation emitted from the accretion disk surface depends on its structure and temperature, hence on the distance to the black hole.

An accretion disk around a supermassive black hole at the center of an AGN extends from the radius of a marginally stable orbit R_{ms} to several thousands of gravitational radii (R_g). On the basis of radiation emitted in different spectral bands, it can be stratified in several parts (Jovanović & Popović, 2009a): a) an innermost part close to the central black hole that emits X-rays and extends from the radius of marginally stable orbit R_{ms} to several tens of gravitational radii; b) a central part ranging from $\sim 100\ R_g$ to $\sim 1000\ R_g$, which emits UV radiation; and c) an outer part extending from several hundreds to several thousands R_g, from which the optical emission orriginates (Eracleous & Halpern, 1994, 2003). Here we consider an optical emission disk.

We model the emission from an accretion disk using numerical simulations based on ray-tracing method in Kerr metric (Bao et al., 1994; Bromley et al., 1997; Fanton et al., 1997; Čadež et al., 1998), taking into account only photon trajectories reaching the observer's sky plane. In this method the image of the disk on the observer's sky is divided into a number of small elements (pixels). For each pixel, the photon trajectory is traced backward from the observer by following the geodesics in a Kerr space-time, until it crosses the plane of the disk (see Fig. 4.2). Then, the flux density of the radiation emitted by the disk at that point, as well as the redshift factor of the photon are calculated. In that way, one can obtain the color images of the accretion disk which a distant observer would see by a high resolution telescope. The simulated line profiles can be calculated taking into account intensities and received photon energies of all pixels of the corresponding disk image. For more details see Jovanović & Popović (2009a) and references therein. Although this method was developed for studying the X-ray radiation which originates from the inner parts of the disk close to the central black hole (see e.g. Jovanović & Popović, 2008a), it can be also successfully applied for modelling the UV/optical emission which originates from the outer regions of the disk[1].

[1] As shown in Jovanović & Popović (2008a), the effects of strong gravitational field and angular momentum of rotat-

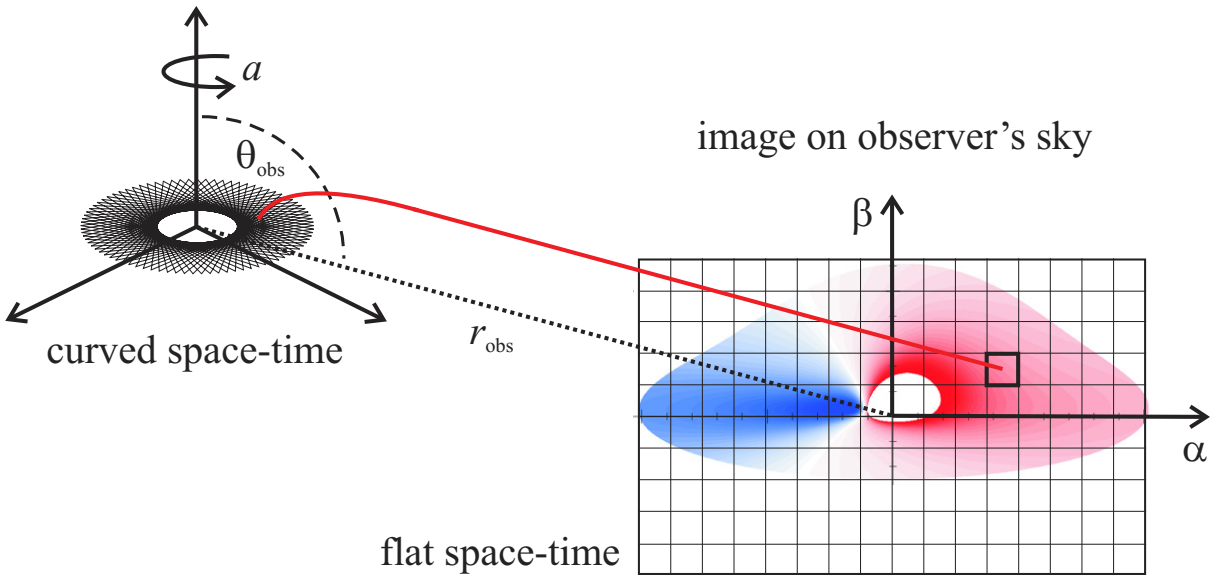

Figure 4.2 Schematic illustration of the ray-tracing method in the Kerr metric, showing a light ray emitted from a certain radius of the accretion disk and observed at a pixel on the disk image in the observer's reference frame (Jovanović & Popović, 2009a).

Surface emissivity of the disk is usually assumed to vary with radius as a power law (e.g. Popović et al., 2003): $\varepsilon(r) = \varepsilon_0 \cdot r^a$, where ε_0 is emissivity constant and a – emissivity index. Total observed flux is then given by:

$$F_{obs}(E_{obs}) = \int_{image} \varepsilon(r) \cdot g^4 e^{-\frac{1}{2}\left(\frac{E_{obs} - gE_0}{\sigma}\right)^2} d\Xi, \tag{4.1}$$

where g is the energy shift due to the relativistic effects: $g = \frac{\nu_{obs}}{\nu_{em}}$, E_0 is the rest energy of the line, σ is the local turbulent broadening and $d\Xi$ is the solid angle subtended by the disk in the observer's sky.

We adopted the following modification of the power-law disk emissivity, in order to introduce a bright spot–like perturbing region in the disk (Jovanović & Popović, 2008b, 2009a,b; Stalevski et al., 2008):

$$\begin{aligned} \varepsilon_1(x,y) &= \varepsilon(r(x,y)) \\ &\cdot \left(1 + \varepsilon_p \cdot e^{-\left(\left(\frac{x-x_p}{w_x}\right)^2 + \left(\frac{y-y_p}{w_y}\right)^2\right)}\right), \end{aligned} \tag{4.2}$$

where $\varepsilon_1(x,y)$ is the modified disk emissivity at the given position (x,y) expressed in gravitational radii R_g, $\varepsilon(r(x,y))$ is the ordinary power-law disk emissivity at the same position, ε_p is

ing black hole are significant only in the innermost parts of accretion disk, in vicinity of the central supermassive black hole, up to the several dozens of gravitational radii. In the outer parts of the disk, such as those where the Hβ line originates, these effects are negligible and Kerr metric with zero angular momentum, i.e. Schwarzschild metric, is a very good approximation.

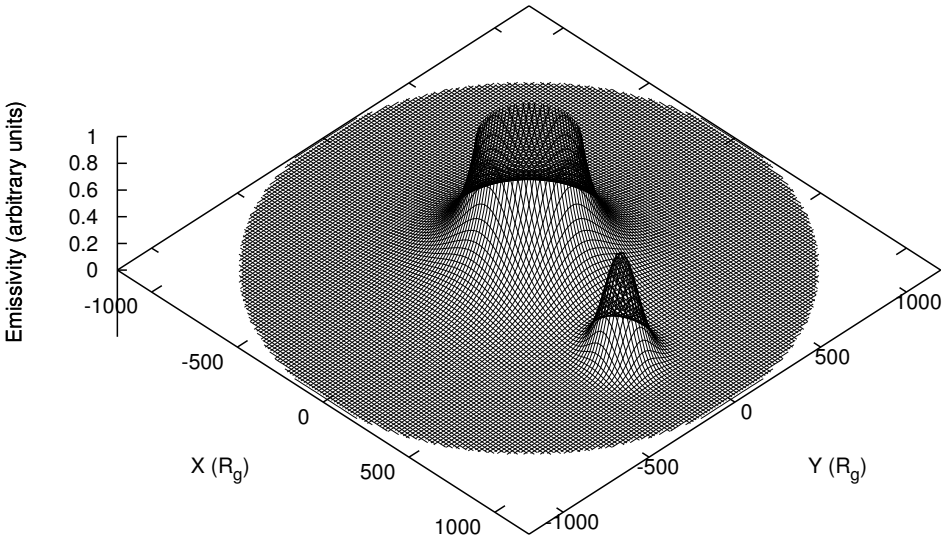

Figure 4.3 A 3D plot of modified disk emissivity given by Eq. (4.2) for 200 $R_g \leq r(x,y) \leq$ 1200 R_g, $a = -2.5$ and for the following parameters of the perturbing region: $\varepsilon_p = 5$, $x_p =$ 700 R_g, $y_p = -150$ R_g and $w_x = w_y = 100$ R_g.

emissivity of the perturbing region (i.e. amplitude of the bright spot), (x_p, y_p) is the position of perturbing region with respect to the disk center (in R_g) and (w_x, w_y) are its widths (also in R_g). A 3D plot of above expression for modified emissivity law is given in Fig. 4.3. This simple model is suitable for our purpose because it allows us to change amplitude, width and location of bright spot in respect to the disk center. In that way we are able to simulate displacement of a bright spot along the disk, its widening and amplitude decrease with time (decay). Moreover, the above bright spot model can be successfully applied for studying variations of accretion disk emission in different spectral bands, from X-rays to optical band (see e.g. Jovanović & Popović, 2008b, 2009b; Stalevski et al., 2008).

4.3.1 Perturbation in the accretion disk: modeled profiles

In order to test how this model with a bright spot affects the Hβ line profile, we performed several numerical simulations of perturbed emission of an accretion disk in Kerr metric for different positions of a bright spot along x and y-axes. For these simulations we adopted the following parameters of the disk: inclination $i = 30^o$, inner and outer radii $R_{in} = 200$ and $R_{out} = 1200\ R_g$, power law emissivity with index $a = -1$, local turbulent broadening $\sigma = 2000$ km s^{-1} and normalized angular momentum of black hole with value of 0.5. The corresponding results are presented in Fig. 4.4. As it can be seen from this figure, when the bright spot moves along the positive direction of x-axis (receding side of the disk) it affects only "red" wing of the line (Fig. 4.4, top right), but when it moves along the negative direction of x-axis (approaching side of the disk) it affects only "blue" wing of the line (Fig. 4.4, top left). In both cases, the other wing and the line core stay nearly constant, and therefore almost unaffected by the bright spot. The situation is quite opposite when the bright spot moves in both directions along the y-axis, because then it affects only the line core, while the both of its wings stay almost intact (see the bottom panels of Fig. 4.4).

We also performed the corresponding simulations for different positions of a bright spot which moves from the inner radius of the accretion disk towards its outer parts along the $y = x$ direction, and found similar behavior of the simulated line profiles (see Fig. 4.5). As one can see from Fig. 4.5, for certain positions of the perturbing region along $y = x$ direction we obtained the line profile with almost symmetrical wings, while in other cases either the "blue" peak is brighter than the "red" one, or the "red" peak is stronger than the "blue" one.

The next step in our analysis was to use our numerical simulations for fitting the observed spectra of 3C 390.3 in order to study the variability of its Hβ spectral line due to emissivity perturbations in the accretion disk.

4.3.2 A case study of 3C 390.3

Observations

To test the model, we used 22 spectra of 3C 390.3 observed from November 1995 until June 1999 (see Fig. 8 in Shapovalova et al., 2001).

Spectra of 3C 390.3 were taken with the 6 m and 1 m telescopes of the SAO RAS (Russia, 1995–2001) and at INAOE's 2.1 m telescope of the "Guillermo Haro Observatory" (GHO) at Cananea, Sonora, México (1998–1999) in the monitoring regime in 1995-1999. They were obtained with long slit spectrographs, equipped with CCD detector arrays. The typical wavelength interval

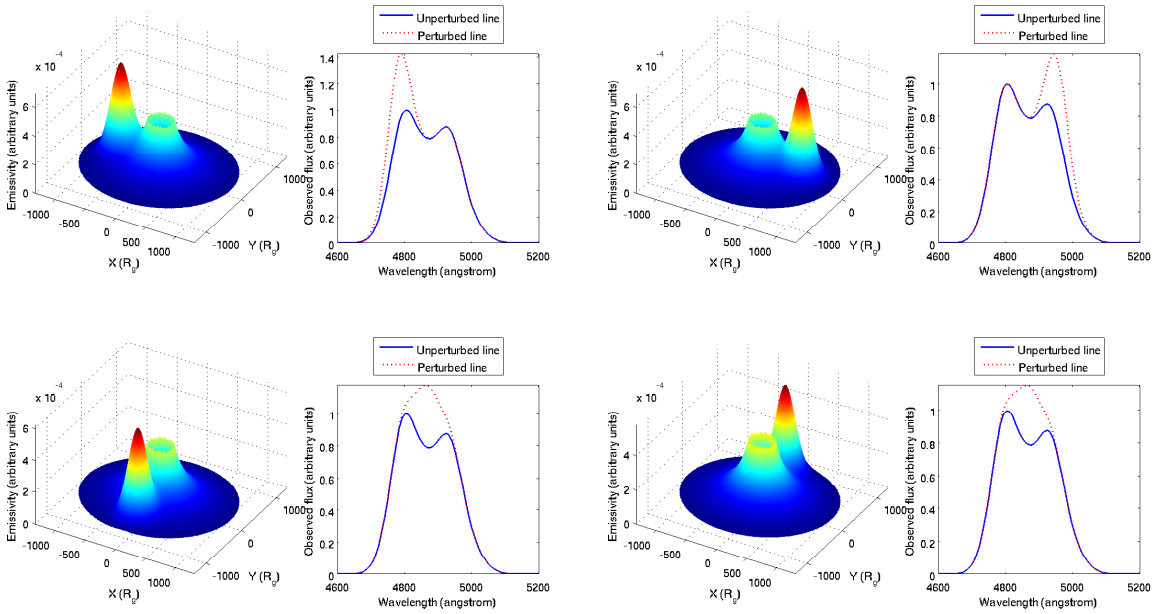

Figure 4.4 Shapes of perturbed emissivity of an accretion disk in Kerr metric and the corresponding perturbed (dashed line) and unperturbed (solid line) Hβ line profiles for the following parameters of perturbing region: $\varepsilon_p = 5$, $w_x = w_y = 200\ R_g$. The positions of perturbing region are: $x_p = -700\ R_g$ and $y_p = 0$ (top left), $x_p = 700\ R_g$ and $y_p = 0$ (top right), $x_p = 0$ and $y_p = -700\ R_g$ (bottom left) and $x_p = 0$ and $y_p = 700\ R_g$ (bottom right).

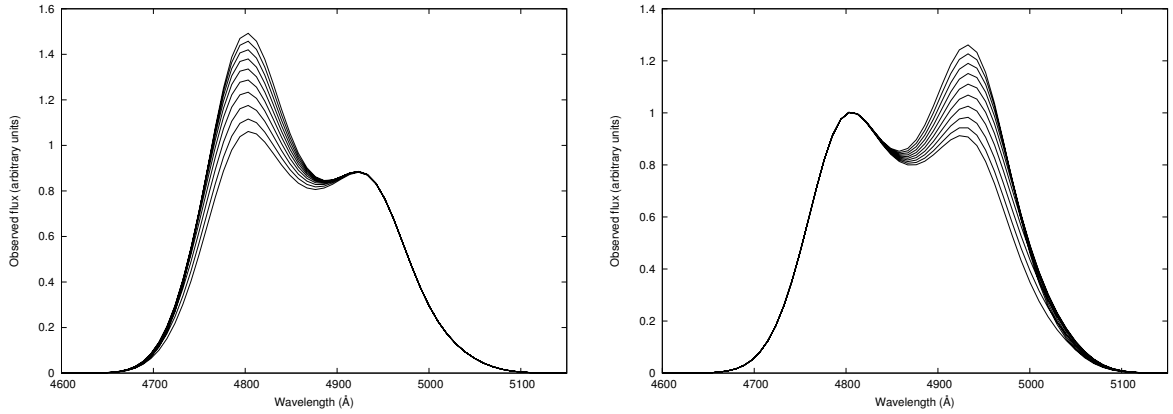

Figure 4.5 Variations of the perturbed Hβ line profile for different positions of the bright spot along the $y = x$ direction. Disk parameters are the same as used in examples in Fig. 4.4. Left panel corresponds to the positions of the bright spot on approaching side of the disk, while the right panel corresponds to the receding side of the disk. In both cases, the positions of the bright spot were varied from the inner radius (bottom profiles) of the disk towards its outer radius (top profiles).

covered was that from 4000 Å to 7500 Å, the spectral resolution varied between 5 and 15 Å and the S/N ratio was > 50 in the continuum near Hα and Hβ. The details on the data reduction can be found in Shapovalova et al. (2001) and Shapovalova et al. (2010).

Perturbation in the accretion disk of 3C 390.3

Radial velocities of the blue and red peaks of the Hβ and Hα broad lines of 3C 390.3 vary with time (see e.g. Gaskell, 1996; Eracleous et al., 1997; Shapovalova et al., 2010). Shapovalova et al. (2010) obtained the Hβ difference profiles by subtracting the average spectrum corresponding to the minimum activity state (September 9, 1997) from the individual spectra (see their Fig. 11). These authors found (see their Table 7) that the radial velocity of the blue peak increased from -3200 km s^{-1} in 1995-1996 to -5200 km s^{-1} in 1999. At the same time the radial velocity of the red peak increased from +4900 km s^{-1} in 1995-1996 to +7000 km s^{-1} in 1999. Here we analyze the possibility that the velocities, corresponding to the peak shifts in the Hβ integral and difference profiles, vary with time due to perturbations in the disk emissivity.

In order to fit the spectral Hβ line shapes of 3C 390.3, we first estimated the disk parameters from several profiles. We found following parameters of the disk: inclination $i = 20^o$, inner and outer radii $R_{in} = 100$ and $R_{out} = 1300\ R_g$, broken power law emissivity with index $a = -1$ for $R_{in} < r < R_{br}$ and $a = -3$ for $R_{br} < r < R_{out}$, radius at which slope of emissivity changes $R_{br} = 500\ R_g$, emissivity of perturbing region $\varepsilon_p = 1$, local turbulent broadening $\sigma = 2000$ km s^{-1} and normalized angular momentum of black hole $a = 0.5$. These values of parameters are in accordance with the corresponding parameters for 3C 390.3 obtained by Flohic & Eracleous (2008), who found the following values: $i = 27^o$, $R_{in} = 450$, $R_{out} = 1400\ R_g$ and $\sigma = 1300$ km s^{-1}. In all our simulations we fixed the emissivity of perturbing region at $\varepsilon_p = 1$, but nevertheless, the brightness of perturbing region varies with time due to its changeable area (i.e. its widths are taken as free parameters which vary in time), as well as due to the power law emissivity of the disk which decreases with radius. We studied the stationary and moving perturbing regions, and in the latter case their coordinates are also assumed as free parameters.

The fitting of the observed Hβ line shapes of 3C 390.3 is performed separately in the case of moving and stationary perturbing regions in the following three steps: (i) the simulated Hβ line profiles are calculated for some initial set of values of free parameters; (ii) the corresponding root mean square (RMS) of residuals between the observed and simulated line profiles is calculated; (iii) the values of free parameters are varied and the procedure (i)-(iii) is repeated until the RMS deviations (RMSD) between the observed and fitted Hβ profiles become as small as possible.

Fig. 4.6. shows comparisons between all 22 observed spectra (black solid line) and the obtained best fits assuming the moving (red solid line) and stationary (blue dashed line) perturbing re-

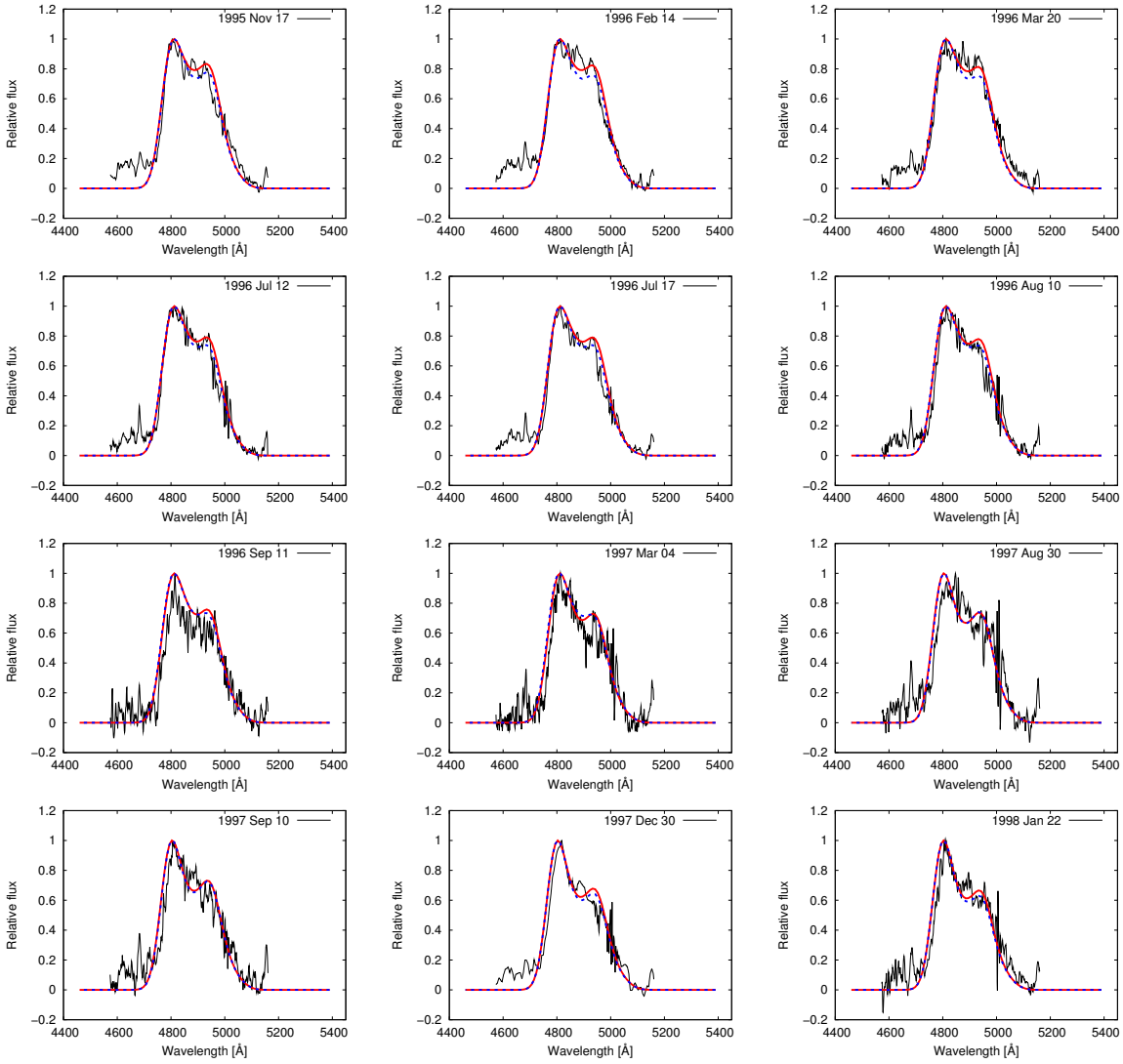

Figure 4.6 Comparisons between the observed Hβ line profiles of quasar 3C 390.3 (black solid line) and the corresponding simulated profiles due to two successive bright spots. The red solid line represents the simulated profiles due to the moving bright spots which estimated positions are presented in Fig. 4.7 and widths in Table 4.1. The blue dashed line corresponds to the simulated profiles due to the stationary bright spots, positioned at $x = -100\ R_g$, $y = 220\ R_g$ during the first outburst and at $x = -220\ R_g$, $y = 125\ R_g$ during the second outburst.

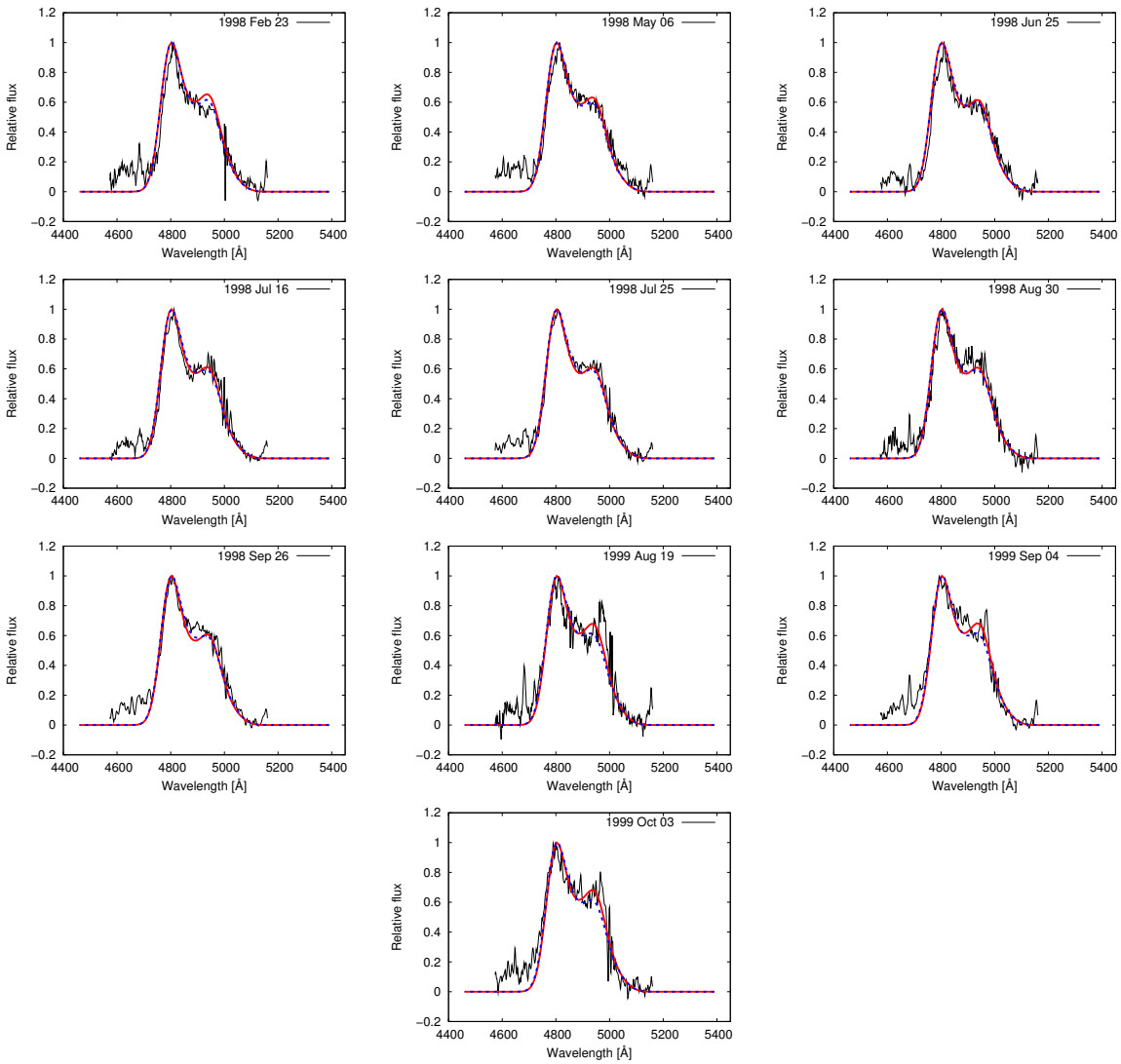

Figure 4.6 (continued)

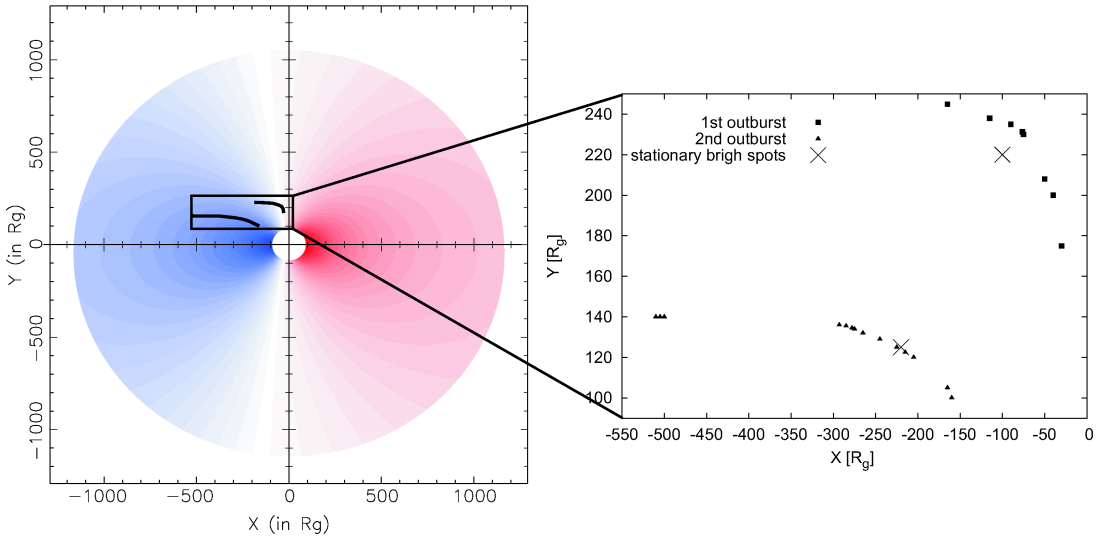

Figure 4.7 Positions of moving perturbing region along the accretion disk corresponding to two observed amplitude outbursts: October 1994 – July 1997 outburst (squares) and July 1997 – June 1999 outburst (triangles). In both cases, the moving perturbation originates in the inner regions of the disk and spirals away towards its outer parts. For the average speed of the first perturbation we obtained value of 7298 km s^{-1} and for the second one 6575 km s^{-1}. Positions of the stationary perturbing region (denoted by crosses in the right panel) are: $x = -100\ R_g$, $y = 220\ R_g$ during the first outburst and $x = -220\ R_g$, $y = 125\ R_g$ during the second outburst.

gions, while the corresponding positions of the perturbing regions are presented in Fig. 4.7. As it can be seen from Fig. 4.7, the obtained positions of the moving perturbing regions are distributed in the form of two spiral arms, indicating that these perturbations originate in the inner regions of the disk and spiral away towards its outer parts, moving faster in the azimuthal direction as they get further away from the center of the disk. Table 4.1. contains the obtained values of the fitted parameters, as well as the corresponding RMSD in the case of both, moving and stationary perturbing regions. We first studied the moving perturbations, but after examining the obtained results we found that, during a period of a few years, such perturbations move only by small distances which are comparable to their widths (see Table 4.1). Therefore, in order to test whether the obtained displacements are reliable, we repeated the fitting, but this time assuming the stationary perturbing regions with variable widths. In this case we obtained the best fits for two perturbations positioned at $x = -100\ R_g$, $y = 220\ R_g$ and at $x = -220\ R_g$, $y = 125\ R_g$, respectively (denoted by crosses in Fig. 4.7). As one can see from Fig. 4.6. and Table 4.1, regardless the significant variations of the Hβ line profile during the analyzed period, both models of perturbing region resulted in similar fits for the most of these spectra, except for the spectra observed during 1999, where the moving perturbing region achieved better fits. The latter result should be taken with caution because the observations from 1999 were performed after a large gap of ≈ 1 year. Therefore, the displacements of the perturbing regions cannot be considered as indisputably confirmed, but on the contrary, their widths almost certainly vary

with time. The last conclusion is valid for both, moving and stationary perturbing regions, since neither of them can provide satisfactory fits with fixed widths.

The obtained best fit positions of both, moving and stationary perturbations are located on the approaching side of the accretion disk (see Fig. 4.7) and these perturbations can be most likely attributed to successive occurrences of two different bright spots. This assumption is in good agreement with observations, since two large amplitude outbursts of Hβ line are observed during the analyzed period (Shapovalova et al., 2001), and therefore each bright spot can be assigned to one of them: the bright spot which positions are denoted by squares corresponds to October 1994 - July 1997 outburst while the other one, which positions are denoted by triangles, corresponds to July 1997 - June 1999 outburst. Using the time differences between two successive observed spectra we were able to estimate the speeds of both moving bright spots (see Table 4.1). For an average velocity of the first bright spot we obtained the value of 7298 km s^{-1} and for the second one 6575 km s^{-1}. As it can be seen from Table 4.1, widths of bright spots are increasing with time, indicating that they decay until they completely disappear. It should be noted that, inevitably, there is a certain degree of degeneracy in the parameter space, since similar results could be obtained with somewhat different combinations of perturbing region positions and widths.

Table 4.1 Parameters of perturbing region obtained by fitting the observed spectra.

Date	JD (2400000+)	$x[R_g]$	$y[R_g]$	$w[R_g]$		$d[R_g]$	v[km s^{-1}]	RMSD	
(1)	(2)	(3)	(4)	(5)	(6)	(7)	(8)	(9)	(10)
The First Outburst									
1995 Nov 17	50039.156	-30	175	100	100			0.09730	0.09460
1996 Feb 14	50127.602	-40	200	105	130	26.93	5203.24	0.09680	0.09900
1996 Mar 20	50162.580	-50	208	106.5	140	12.81	6257.63	0.08476	0.09138
1996 Jul 12	50276.567	-75	230	110	180	33.3	4993.36	0.08518	0.08178
1996 Jul 17	50281.434	-76.3	231.3	110	180	1.84	6456.24	0.08820	0.08249
1996 Aug 10	50305.489	-90	235	112	190	14.19	10082.9	0.09435	0.09201
1996 Sep 11	50338.309	-115	238	120.5	200	25.18	13112.6	0.12337	0.12426
1997 Mar 04	50511.622	-165	245	130	260	50.49	4978.94	0.11448	0.12082
The Second Outburst									
1997 Aug 30	50691.463	-160	100	100	100			0.13717	0.13593
1997 Sep 10	50701.576	-165	105	105	110	7.07	11950.55	0.12034	0.11905
1997 Dec 30	50813.195	-205	120	145	175	42.72	6541.48	0.09499	0.09398
1998 Jan 22	50835.631	-215	122.5	155	195	10.31	7852.39	0.10690	0.10949
1998 Feb 23	50867.560	-225	125	165	215	10.31	5517.75	0.09825	0.09618
1998 May 06	50940.354	-245	129	185	265	20.40	4788.88	0.08867	0.08965
1998 Jun 25	50990.302	-265	132	205	285	20.22	6920.32	0.07229	0.07387
1998 Jul 16	51010.719	-275	134	210	295	10.20	8537.04	0.06809	0.07141
1998 Jul 25	51019.723	-278	134.5	212	300	3.04	5773.22	0.06548	0.06615
1998 Aug 30	51055.551	-285	135.5	215	320	7.07	3373.22	0.07590	0.07638
1998 Sep 26	51082.429	-293	136	218	340	8.01	5097.09	0.07948	0.07788
1999 Aug 19	51410.309	-500	140	250	400	207.04	10792.43	0.10645	0.11163
1999 Sep 04	51426.208	-505	140	252	400	5	5375.06	0.09147	0.09232
1999 Oct 03	51455.172	-510	140	254	400	5	2950.49	0.09977	0.10270

Note. — Col. (1): date of observation; Col. (2): epoch of observation (in JD); Cols. (3-4): x and y coordinates of the moving bright spots; Col. (5): widths ($w = w_x = w_y$) of the moving bright spots; Col. (6): widths ($w = w_x = w_y$) of the stationary bright spots, positioned at $x = -100\ R_g$, $y = 220\ R_g$ during the first outburst and at $x = -220\ R_g$, $y = 125\ R_g$ during the second outburst; Col. (7): linear distance crossed by the moving bright spots between two successive observations; Col. (8): average speed of the moving bright spots between two successive observations; Col. (9): root mean square deviation between the observed and fitted Hβ line profiles in the case of the moving bright spots; Col. (10): the same as Col. (9), but in the case of the stationary bright spots.

4.4 Discussion

Several physical mechanisms could be responsible for perturbations in the accretion disk emissivity, i.e. for bright spot formations. The most plausible candidates for such mechanisms are: disk self-gravity, baroclinic vorticity, disk-star collisions (Flohic & Eracleous, 2008, and references therein), tidal disruptions of stars by central black hole (Strubbe & Quataert, 2009, and references therein) and fragmented spiral arms (Lewis et al., 2010, and references therein).

The disk self-gravity, driven by Jeans instability, could cause production of clumps in the disk which have typical sizes in the range from 10 to 1000 gravitational radii for a 10^8 $M_\odot$ central black hole. Such clumps do not shear with differential rotation and they have high brightness that varies very little over time. Since the obtained results indicate that bright spots decay in time and spiral along the disk, it is not likely that these bright spots could be identified as clumps created by self-gravity, although their sizes are comparable.

Baroclinic vorticity appears in the accretion disk due to its differential rotation in combination with the radial temperature gradient, causing the material in the disk to spiral around the center of vortex. Such a vortex would have a higher density, and hence a higher brightness, causing the formation of a bright spot. The typical sizes of such spots, as well as their shearing with differential rotation of the disk, are still unknown since different numerical simulations gave contradictory results (for more details see e.g. Flohic & Eracleous, 2008, and references therein). Therefore, in the case of 3C 390.3, this mechanism still cannot be neither ruled out, nor accepted.

Disk-star collisions are assumed to be very frequent events which happen on daily timescales and which could increase the disk surface temperature in the region of collision, and thus, create a bright spot. Such bright spots shear with differential rotation of the disk and decay as the material cools down. However, the typical size of a such bright spot immediately after a collision is close to the size of a star, which is very small when expressed in gravitational radii. Therefore, neither this mechanism could be accepted as a potential cause of two bright spots, detected in the case of quasar 3C 390.3.

The tidal disruption of stars by central black hole (Strubbe & Quataert, 2009, and references therein) happens when a star passes the tidal radius of the black hole, i.e. when the black hole's tidal gravity exceeds the star's self-gravity. Gas of a disrupted star falls back to the black hole at a super-Eddington rate, releasing a flare of energy which then blows away a significant fraction of the falling gas as an outflow. Such super-Eddington flares and outflows could induce instabilities in accretion disk in form of bright spots. However, this mechanism is an unlikely candidate for a potential cause of the bright spots in the case of 3C 390.3 due to the following weaknesses: (i) super-Eddington outflows are short living ($\sim$ 10 days); (ii) frequency of star disruptions in a typical elliptical galaxy is very low, between 10^{-5} and 10^{-4} per year, and in the

case of the black hole of 3C 390.3 which mass is $\sim 5 \times 10^8 M_\odot$ (Lewis & Eracleous, 2006), it is near the low end of this range (see e.g. Magorrian & Tremaine, 1999; Wang & Merritt, 2004); (iii) any stellar debris could be hardly released in the case of 3C 390.3 since main sequence stars are disrupted within the innermost stable orbit around a non-rotating black hole as massive as that in 3C 390.3; (iv) it is unclear how the bright spots produced by this mechanism should evolve with time.

Spiral arms in AGN disks could be formed spontaneously due to self-gravity instabilities (see e.g. Flohic & Eracleous, 2008, and references therein) or could be triggered by a close passage of massive object such as another supermassive black hole or a star cluster (see e.g. Lewis et al., 2010, and references therein). Spiral arms increase the flux variability of AGN on timescales of a year to several years, but as noted before, they are unable to reproduce all aspects of the observed variability. However, they are also subjected to fragmentation, causing small variations in the flux on timescales of several months. The fragments in spiral arms can be due to sub-structures in a non-uniform accretion disk, such as isolated clumps which could pass through the arm and dominate in its emissivity, causing the discrete "lumps" of excess emission (Lewis et al., 2010). The observed variability on timescales from a few months to several years in the difference spectra of some AGNs is probably caused by such lumps. It is quite possible that some of these lumps are long-living and that they do not vary significantly in strength, shape, or position over a period of several years (Lewis et al., 2010). As the obtained results show, it is the same case with the large bright spots which are responsible for amplitude outbursts of the 3C 390.3 Hβ line, because they have a constant emissivity and they are either stationary or spiralling over small distances during the period of several years. The only feature which significantly varies with time is their width. Therefore, these bright spots could be most likely explained by the emissivity lumps, caused by fragments in spiral arms of the accretion disk.

4.5 Conclusions

We developed a model of the disk perturbing region in the form of a single bright spot (or flare) by a modification of the power law disk emissivity and used this model to simulate the disk line profiles. This model has been used to fit the observed Hβ line of 3C 390.3 observed from 1995 to 1999. From this investigation we can point out the following results (Jovanović et al., 2010; Stalevski et al., 2010):

(i) The model which includes a perturbation (bright spot) in the accretion disk can successfully explain difference in double peaked line profiles, as e.g. higher red peak even if we have the standard circular disk. The position of a bright spot has a stronger influence on one particular part of spectral line profiles (such as e.g. its core if the spot is in the central part of the disk, or "red" and "blue" wings if the spot is located on receding and approaching part, respectively).

(ii) Using the model with a perturbing region we were able to successfully model and reproduce the observed variations of the Hβ line profile in the case of 3C 390.3, including the two large amplitude outbursts observed during the analyzed period. Therefore, the observed variations of the 3C 390.3 Hβ line could be caused by perturbations in the disk emissivity.

(iii) We found that two outbursts referred by Shapovalova et al. (2001) could be explained by successive occurrences of two different bright spots on approaching side of the disk which are either moving, originating in the inner regions of the disk and spiralling outwards, or stationary. Both bright spots decay in time until they completely disappear.

(iv) Our results support hypothesis that the perturbations in the accretion disk emissivity are probably caused by fragments in the spiral arms of the disk.

The results presented above show that a circular disk with perturbations (bright spots) can be applied to explain different double peaked line profiles, and can be also used to trace perturbations (as well as their characteristics) from the broad double peaked line shapes.

5 Photocentric variability of quasars caused by variations in their inner structure

5.1 Introduction

In the previous chapters we presented the developed models of the dusty torus and accretion disk with perturbing region. We used both of these models to study variations of quasar photocenters, caused by an outburst in the accretion disk luminosity and changes in the torus structure of torus, in the context of the future Gaia mission. Gaia is a global astrometric interferometer mission that aims to determine high-precision astrometric parameters for one billion objects with apparent magnitudes in the range $5.6 \leq V \leq 20$ (see e.g. Perryman et al., 2001; Lindegren, 2008). It is foreseen that around 500 000 quasars will be among these objects. These quasars will be used to construct a dense optical quasar-based celestial reference frame (see Bourda et al., 2010). The relevance of quasars to the celestial frames compliant to the International Celestial Reference System (ICRS), such as the current International Celestial Reference Frame (ICRF2) or the Gaia celestial reference frame, relies on a photocenter position stability at the sub-mas level. Sub-mas accuracy in the measured positions is the goal of Gaia, namely for objects of 12 mag around 0.003 mas, of 15 mag 0.01 mas and 20 mag 0.2 mas (Perryman et al., 2001).

However, in central regions of quasars different physical processes occur that may cause a variation in the photometric center of objects. A well known property of AGNs is their flux variability, which may have multiple origins such as variation in the accretion rate, instabilities of the accretion disk around the central black hole, supernova bursts, jet instabilities, and gravitational microlensing (see e.g. Andrei et al., 2009; Shields et al., 2010; Popović et al., 2011).

Taris et al. (2011) reported on the possibility of a correlation between the flux variability and photocenter motion in quasars, which is a very relevant subject for missions such as Gaia. There are different sources of photocenter variation. It is well-known that the main output of the different structures of an AGN (such as accretion disk, jets, line-emitting regions, torus, etc) differs in energy. Consequently the sizes and position of the emitting regions are "wavelength dependent". Opacity effects also explain the frequency-dependent core-shifts in the radio synchrotron emission at the base of relativistic jets (Porcas, 2009), and core shifts (between two radio wavelengths) of up to 1.4 mas have been reported by Kovalev et al. (2008).

AGNs have a complex structure, and one can expect that the origin of this photocenter variation is caused by changes in their inner structure. As for instance, a dusty torus, illuminated by a varying central continuum, or variable processes occurring in the accretion disk, such as outburst, and perturbations (see e.g. Jovanović et al., 2010; Popović et al., 2011) may contribute to photocenter variation.

In this chapter, we investigate the photocentric variability of quasars caused by changes in their inner structure. We consider: (a) a perturbation in a accretion disk around a SMBH, and (b) changes in the pattern of radiation scattered by the dust particles in the surrounding torus caused by variations in the accretion disk luminosity and resulting change of the dust

sublimation radius.

Our aims are: (a) to show how much these effects may contribute to the variability of the photocenter, i.e. to quantify "noise" and more accurately characterize any resulting error in the position determination; (b) to estimate the possibility of detecting this effect with Gaia mission; and (c) to identify in which quasars these effects may be dominant.

This chapter is organized as follows. In Section 5.2 we present the parameters and relevant properties of the models of accretion disk and dusty torus. Results of our calculations of photocenter variability for different parameters of the disk and torus are given in Section 5.3. In Section 5.4, we consider the properties of two quasars in the context of obtained results from our simulations and discuss possible scenarios of observed variations of photocenter. In Section 5.5, we outline our conclusions. The work presented in this chapter has been published in Popović et al. (2012).

We used the dusty torus model described in Section 2.3 and the accretion disk model with bright spot–like perturbing region described in Section 4.2. We refer the reader to those sections for details; here we will only give an overview of models' parameters and discuss some properties relevant for this study.

5.2.1 Photocenter offset

The observed photocenter (X_{pc}, Y_{pc}) of the source can be modeled as a centroid of observed flux F over the source image (accretion disk or dusty torus), i.e. as the mean of impact parameters (x, y) of all pixels along the image, weighted by F

$$X_{pc} = \frac{\sum_{i=1}^{N}\sum_{j=1}^{N} F(i,j)\cdot x(i,j)}{\sum_{i=1}^{N}\sum_{j=1}^{N} F(i,j)},$$
$$Y_{pc} = \frac{\sum_{i=1}^{N}\sum_{j=1}^{N} F(i,j)\cdot y(i,j)}{\sum_{i=1}^{N}\sum_{j=1}^{N} F(i,j)}, \tag{5.1}$$

where (i, j) is a point on a $N \times N$ grid of the source image pixels.

When considering photocenter offset of the accretion disk, we include a perturbation (a bright spot) at a certain part of the disk, for different values of the spot brightness, and calculate the photocenter and its offset according to the Eq. 5.1.

Variations in the accretion disk emission may also cause a photocenter offset due to another effect. According to Eq. (2.5) the dust sublimation radius (i.e. inner radius of torus) depends on the total bolometric luminosity of the central source (i.e. accretion disk):

$$R_{\rm in} \simeq 1.3 \cdot \sqrt{L_{46}^{AGN}} \cdot T_{1500}^{-2.8} \qquad [\rm pc]$$

Thus, with increasing luminosity of accretion disk, the inner radius of torus also increases. This means that (a) the innermost structure of the torus changes and (b) the radiation from accretion disk is able to penetrate further into the torus. These two effects will change the illumination of clumps and the pattern of the scattered radiation, which may lead to variations in the photocenter position. The photocenter of dusty torus is calculated in the same way as for the accretion disk (Eq. 5.1).

5.2.2 Parameters of the accretion disk and perturbing region

In the model, we are able to change the parameters of the accretion disk (dimension, emissivity, inner and outer radius, inclination) and the parameters of the perturbation (size, position, and brightness). Taking into account the results of previous studies, one can expect the dimensions of the accretion disk to be several thousands of gravitational radii (see e.g. Eracleous & Halpern, 1994, 2003; Popović et al., 2011), hence here we assumed an accretion disk with the inner and outer radius of R_{inn} = 100 R_g and R_{out} = 3000 R_g, respectively. In our simulations, we consider a low-inclined ($i = 5°$) or near face-on disk, because a near face-on disk is preferred from investigations of the broad line shapes (see e.g. Popović et al., 2004; Bon et al., 2009b). Although the adopted inclination angle is small, it is sufficient to induce Doppler and relativistic beaming effects (see e.g. Fig. 9 in Reynolds & Nowak, 2003, and the corresponding discussion below). As shown in Reynolds & Nowak (2003), even in the case of a nearly face-on disk, these effects can still produce rather broad emission lines, unlike in the case of a face-on Newtonian disk, which would display very narrow lines. In addition, for a steep disk emissivity where $a < -2$, the line emission of the disk is dominated by its inner regions $R_{out} < 50\ R_g$. However, for the disk emissivity where $a > -2$, the bulk of the line emission comes from the outer regions of the disk, thus both Doppler and relativistic beaming effects cannot be neglected even at such relatively large distances from the central black hole. Since the most realistic values for the emissivity of the disk are probably between 0 and -2 (see e.g. Eracleous & Halpern, 1994, 2003; Popović et al., 2004; Bon et al., 2009a), we modeled the disk emissivity index as $a = 0$, $a = -1$, and $a = -2$.

In our simulation, the dimensions of the perturbation (bright spot) is around 100 – 300 gravitational radii (see Jovanović et al., 2010), taking different values for the brightness and position along the disk.

5.2.3 Parameters of the dusty torus

Although we discussed in detail properties of IR emission of the dust torus in Section 2.4, here we will once again examine typical SEDs, focusing on the properties relevant for investigation of photocenter variations. The parameter that has a very prominent effect on the emission of a torus is the inclination, with $i = 0°$ corresponding to a face-on (type 1) AGN and $i = 90°$ an edge-on (type 2) AGN. In Fig. 5.1, we present the total SED and its thermal and scattered components, along with primary source SED, for these two inclinations. As it can be seen from this figure, there is a clear distinction between the cases of a dust-free line of sight ($i = 0°$; left panel) and those that pass through the torus ($i = 90°$, right panel). In the case of dust-free lines of sight, we can directly see the radiation coming from the accretion disk, while in the case of dust-intercepting paths most of the radiation is absorbed and re-emitted at different wavelengths. From the figure, one can also see that the thermal component predominates the

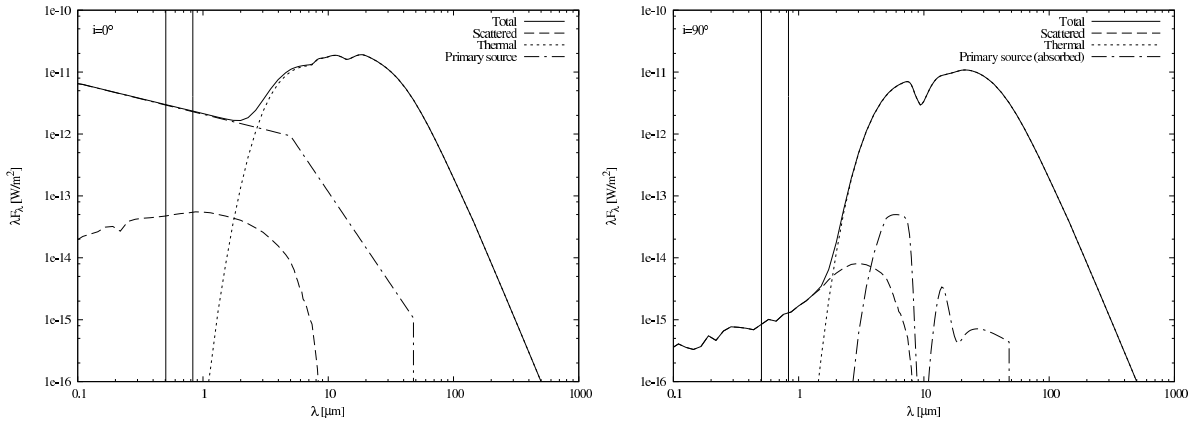

Figure 5.1 The total (solid line), thermal (dotted line), scattered (dashed line), and primary source (dash-dotted line) emission are plotted. The left panel is a type 1 inclination ($i = 0°$), the right panel a type 2 inclination ($i = 90°$). The two vertical lines indicate the central wavelengths of the two dispersing prisms of the Gaia photometric instrument (integrated with the astrometric instrument), at 0.50 and 0.82 μm. Luminosity of the central continuum source is $L = 10^{11} L_{\odot}$ and the rest of torus parameters are the same as described in Section 5.2.3.

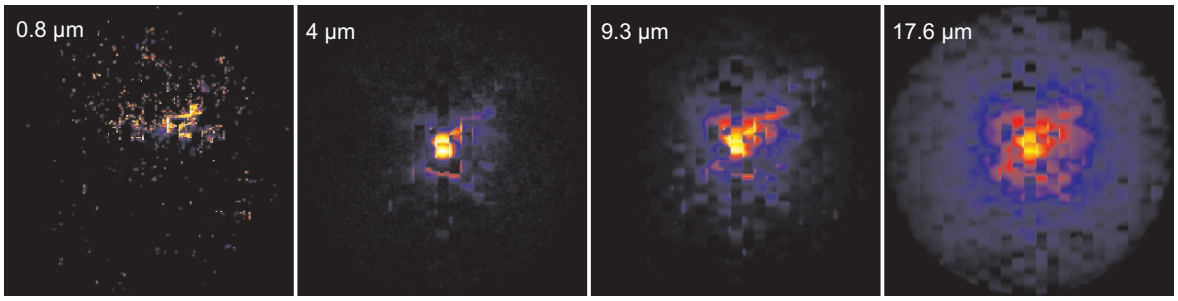

Figure 5.2 Images of the torus at different wavelengths. From left to right, panels represent model images at 0.83, 3.98, 9.31, and 17.6 μm. Images are in logarithmic color scale. The visible squared structure is due to the clumps which in our model are in the form of cubes. The inclination is $i = 50°$; the values of other parameters are the same as taken in Fig. 5.1.

mid- and far-infrared parts of the SED and its overall shape is similar for both the face-on and edge-on orientations. However, the shape and amount of the scattered component is quite different; in the edge-on view, it determines the total SED shortward of 1 μm, while in the face-on view it is negligible compared to the primary source emission. We illustrate this further in Fig. 5.2, where images of the torus at different wavelengths are presented. Shortward of 1 μm (first panel), the thermal component is negligible and only the scattered component that arises randomly from the entire torus is present. In the near- and mid-infrared domain (second and third panel), the thermal radiation from the inner (and hotter) region predominates. At longer wavelengths (forth panel), emission arises from the dust placed further away.

Since in the wavelength range relevant to this work (< 1 μm), the scattered component of the dust emission is dominant, the other parameters, (e.g. those defining geometry and dust

distribution) have only a marginal influence on images of the torus. Therefore, we fixed the following values of torus parameters: optical depth $\tau_{9.7} = 5$; dust distribution parameters (see Eq 2.6) $p = 1$ and $q = 0$; half opening angle $\theta = 50°$; and outer radius $R_{out} = 15$ pc; For the filling factor we adopted the value of 0.25, and for the size of clumps the value of 1.2 pc, allowing single clumps as well as clusters of several merged clumps to appear. We calculated models at two inclinations, $i = 30°$ (dust-free line of sight) and $i = 50°$ (line of sight that passes through the torus). For the total bolometric luminosity of the central continuum source, we adopt the values of $L = 1, 3, 6, 10 \times 10^{11}\ L_{\odot}$. According to Eq. 2.5 (assuming the dust sublimation temperature of 1200 K), the corresponding values of the inner radius of torus are $R_{in} = 0.5, 0.82, 1.16, 1.5$ pc, respectively.

5.3.1 Photocenter offset caused by a perturbation in the accretion disk

We performed simulations for different emissivities and different positions of the bright spot on the disk. As an example, we present three simulations of the photocenter offset due to a perturbation in the disk for three different values of its emissivity index. Fig. 5.3, shows the simulations of the accretion disk without (top left panel) and with a perturbation (other three panels), i.e. the disk images (for a quasar with a SMBH of 10^{10} $M_{\odot}$ at $z = 0.01$) for three different values of the emissivity index $a = 0$ (top right), $a = -1$ (bottom left), and $a = -2$ (bottom right). Photocenter positions are denoted by crosses. The inner and outer radii of the disk are taken to be 100 and 3000 R_g, respectively. The emissivity of the bright spot[1] is $\varepsilon_p = 10$, the position is $X_p = 2500$ R_g, $Y_p = 0$ R_g, and the dimension of the bright spot is taken to be $w_p = 300$ R_g. As can be seen from Fig. 5.3, the offset of the photocenter depends on the disk emissivity and it is the most prominent in a disk with flat emission ($a = 0$): the corresponding offsets are smaller for steeper emissivity laws and vice versa. We also note here that we take a very strong perturbation at the disk edge, and that the maximum emissivity of the perturbing region is taken to be ten times greater than emissivity of the disk disk center.

Occurrences of perturbations in the accretion disk emissivity could be caused by several physical mechanisms, such as disk self-gravity, baroclinic vorticity, disk-star collisions, tidal disruptions of stars by a central black hole, and fragmented spiral arms of the disk (see e.g. Jovanović et al., 2010, and references therein). All these phenomena appear and last at different frequencies and timescales, and could cause perturbations of different strengths, proportions and characteristics. In particular, perturbations of the accretion disk emissivity in the form of flares with high amplitudes are of great significance because they could provide information about accretion physics under extreme conditions. Flares with the highest amplitudes are usually interpreted in terms of tidal disruptions of stars by supermassive black holes (see e.g. Komossa et al., 2008, and references therein). Stars approaching a SMBH will be tidally disrupted once the tidal forces of the SMBH exceed the star's self-gravity, and part of the stellar debris will be accreted, producing a luminous flare of radiation that persists on a timescale of between months and years. This flare is expected to occur in the outer part of the disk (similar to our simulations).

Although, the frequency of these events in a typical elliptical galaxy is very low, between 10^{-5} and 10^{-4} per year (see e.g. Jovanović et al., 2010, and references therein), Komossa et al. (2008) reported the discovery of an X-ray outburst of a large amplitude in the galaxy SDSS

[1] Note here that in the case of tidal disruptions of stars by a supermassive black hole the amplification in the total optical brightness can increase around two times (see Komossa et al., 2008, and discussion below), therefore the small bright spot should have a significantly (around one order) higher emissivity than the disk

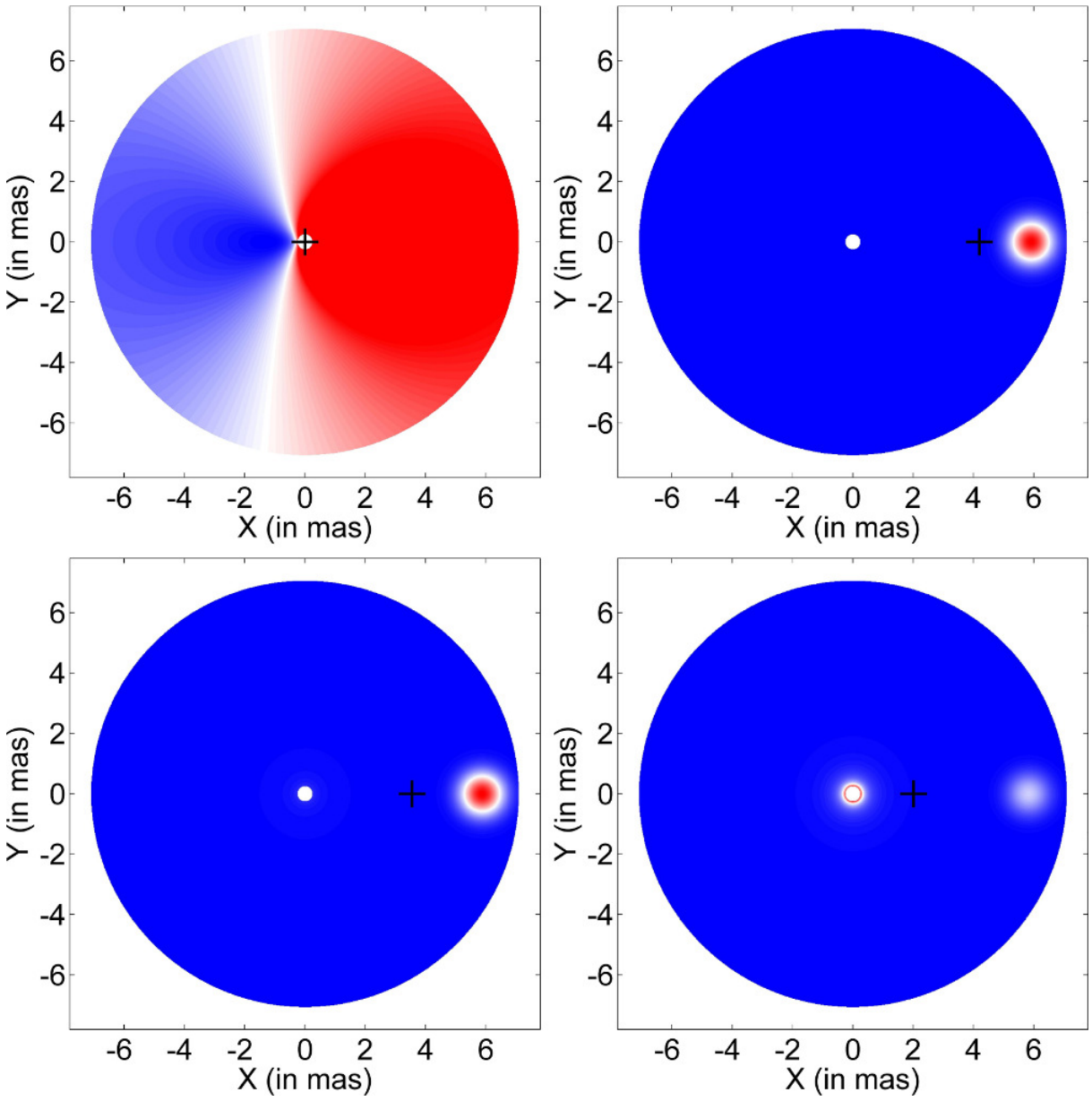

Figure 5.3 Simulations of the accretion disk without (top left) and with perturbation for three different values of the emissivity index: $a = 0$ (top right), $a = -1$ (bottom left), and $a = -2$ (bottom right). The photocenter positions are denoted by crosses. In the top left panel, color represents the energy shift due to relativistic effects (i.e. ratio of the observed to emitted energy), while in the other three panels it represents the observed flux (in arbitrary units). The parameters of the disk and perturbing region are $100\ \mathrm{R_g} \leq r(x,y) \leq 3000\ \mathrm{R_g}$, $\varepsilon_p = 10$, $x_p = 2500\ \mathrm{R_g}$, $y_p = 0\ \mathrm{R_g}$, and $w_p = 300\ \mathrm{R_g}$. The maximum emissivity of the perturbing region is taken to be ten times greater than the emissivity of the disk at its inner radius. Linear distances are converted to angular units along the x and y axes assuming an accretion disk located at cosmological redshift $z = 0.01$ around the central black hole with mass of $10^{10}\ M_\odot$.

Table 5.1 The simulated offsets of photocenter (in mas) caused by perturbation in the accretion disk emissivity for different values of its redshift and mass of a central black hole. Other parameters correspond to the bottom left panel of Fig. 5.3.

M_{BH}	z				
$(M_\odot)$	0.01	0.05	0.10	0.15	0.20
10^8	0.036	0.007	0.004	0.003	0.002
10^9	0.355	0.074	0.039	0.028	0.022
10^{10}	3.550	0.744	0.394	0.278	0.220

J095209.56+214313.3, which was probably caused by the tidal disruption of a star by a supermassive black hole. Although this was a high-energy (EUV, X-ray) outburst, its low-energy (NUV, optical, NIR) echo was also detected.

In general, we found that in the case of luminous bright spot (smaller than the emission in the central source) the offset of the photocenter will be negligible, especially if the bright spot appears close to the center. In addition, when there is high emissivity in the bright spot close to the central source, the effect is small. Only a luminous bright spot located relatively far from the central source can be a good candidate to be observed with Gaia. To estimate whether the offset of the photocenter can be observed we give numerical values of the photocenter offsets (in mas) for different redshifts and black hole masses in Table 5.1. The parameters for the disk and perturbation are taken as given above, for the emissivity index of $a = -1$.

As can be seen from Table 5.1, the largest photocenter offsets ($\sim$ several mas) found at the lowest redshifts ($z \sim 0.01$) and the most massive black holes ($M_{BH} \sim 10^{10}\ M_\odot$), where we can expect to find the accretion disk with the larger dimensions.

5.3.2 Photocenter offset due to the variations in the disk luminosity and changes of the torus structure

As explained in Section 5.2.1, an increase in the accretion disk luminosity may cause variations in the photocenter position. Therefore, for the adopted values of torus parameters (see Section 5.2.3) we generated a set of models for different luminosities and corresponding inner radii (i.e. dust sublimation radii), i.e. $L = 1, 3, 6, 10 \times 10^{11}\ L_\odot$ and $R_{in} = 0.5, 0.82, 1.16, 1.5$ pc, respectively. We calculated models at two inclinations, $i = 30°$ (dust-free line of sight) and $i = 50°$ (line of sight that passes through the torus). For each model, we calculated the photocenter position and its offset from the one in the starting model ($L = 10^{11} L_\odot$).

We found that when the central source is unobscured ($i = 30°$), the brightness of the source is dominant and the photocenter offset is negligible. In Table 5.2, we present values of the photocenter offset in the case of $i = 50°$ and for different accretion disk luminosities and

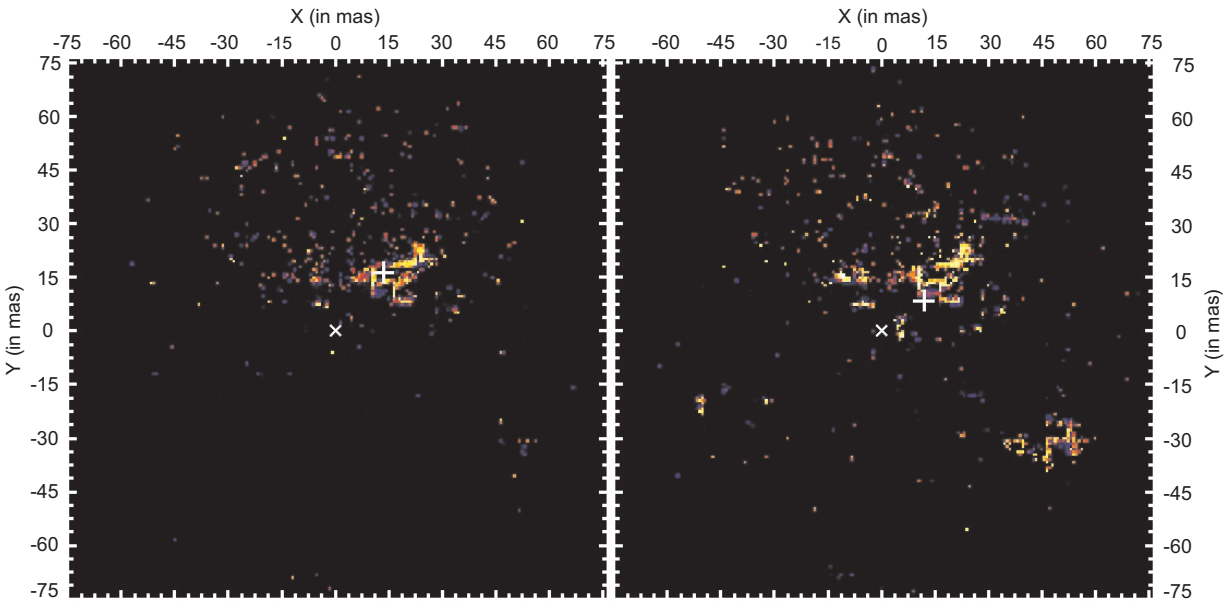

Figure 5.4 Images of the torus at 0.51 μm for two different luminosities and corresponding inner radii, $10^{11} L_{\odot}$ and $R_{in} = 0.5$ pc (left panel) and $6 \times 10^{11} L_{\odot}$ and $R_{in} = 1.16$ pc (right) panel. Photocenter in both panels is denoted with a white cross; black hole in both panels is at the center of the images, denoted with 'x' The photocenter offset between the images is 8.4 mas. The values of other torus parameters are the same as in Fig. 5.2. Images are in a logarithmic color scale.

cosmological redshifts. As can be seen from this table, the photocenter offset is larger for lower cosmological redshifts and bigger luminosity outbursts. In Fig. 5.4, we present images of the torus in the case of the largest photocenter offset (8.4 mas), at $z = 0.01$, for the central source luminosities of 10^{11} $L_{\odot}$ (left panel) and 6×10^{11} $L_{\odot}$ (right panel).

As can be seen from Table 5.2, a large jump in the photocenter offset between the luminosities of 3 and 6×10^{11} $L_{\odot}$ is present. This is caused by the change in the illumination of the torus. As the luminosity of the central source increases, the inner radius of the torus increases as well (the inner structure changes), and the group of clumps farther away from the center may be illuminated (see Fig. 5.4, right panel). However, a further increase in the central source luminosity does not change the illumination pattern of clumps significantly (depending on the actual distribution of clumps) hence the value of the photocenter offset remains nearly the same. In addition, as the central source luminosity continues to increas, the brightness of the central source begins to dominate, and the photocenter gets closer to the central source.

5.3.3 Photocenter position versus flux variation

For one object Taris et al. (2011) found that a relationship between the astrometric and photometric variability exists. We also modeled the expected flux variation with brightness of the perturbed region, and found that the offset of the photocenter in principle can be a function of

Table 5.2 The simulated offsets of photocenter (in mas) for different values of redshift and accretion disk luminosity, calculated for the two photometric instruments with central wavelengths at 0.50 μm and 0.82 μm. The values of torus parameters are the same as in Fig. 5.2.

L	z		
$(10^{11}L_{\odot})$	0.01	0.05	0.10
0.50 μm			
3	1.579	0.208	0.039
6	8.400	1.886	0.860
10	8.170	1.353	0.693
0.82 μm			
3	0.814	0.252	0.135
6	7.120	1.422	0.990
10	7.978	1.466	0.843

the flux variation only in special cases where there is a perturbation located at the same place and the brightness changes with time. In general, there are many possible locations of the perturbations and possible values of their emissivities with respect to the central source. The photocenter position varies in terms of both the accretion disk brightness (that may show variability) and the emissivity of the bright spot, hence the relationship between the astrometric and photometric variability cannot be assumed as the general rule, although it may exist particularly in the μas astrometric regime.

On the other hand, in the case of the changes in the torus structure, as can be seen from Table 5.2, there is a partial correlation between the photometric and astrometric variability, but it is not a rule, especially when illumination stays higher.

The amplitudes of the flux variations in quasars, at certain redshifts, indicate that an enormous amount of energy is produced. The rapid flux variations often seen are convincing evidence of the compactness of the emitting region. Thus, in this case a correlation between astrometric and photometric variability will either not exist or be discerned only with an astrometric precision far higher than the mas level. At the same time, since longer, year-long, and large amplitude variations are also recorded, the same logic would imply that the other quasars elements are not at a standstill, as discussed. The specific causes can be studied when and if an observed long-term, large-amplitude optical variability is related to the astrometric variability of the quasar photocenter (Johnston et al., 2003). In addition, if this were verified, the relationship could indicate that a large photometric variation would make a given quasar less apt to materialize a stable extragalactic reference frame, such as the one from the Gaia mission. The long-term program required to monitor optical fluctuations in long cycles can only be established by ground-based observations. Therefore, the astrometric limit should be on the level of few mas, which, in turn, requires high quality seeing, telescope imaging, and relative astrometry.

We now discuss the possibility that the observed photocenter variability of two observed objects was caused by changes in the inner structure of the AGN.

5.4.1 Observations

To maximize the chances of the photocenter variability being detected on a mas scale, 20 quasars were selected based on their long variability timescales and large photo-variability. Most objects were collected from Teerikorpi et al. (2000), as well as Maccacaro et al. (1987) and inspections of light curves in Smith et al. (1993). The observations were performed under the Observatório Nacional/MCT, Brasil, telescope time contracted to ESO at the Max Planck 2.2 m telescope at La Silla, Chile. The program started on April 2007 and lasted until July 2009, with observations taking place about every two months.

The observing method and the error analysis can be found in Andrei et al. (2009), and some aspects of relative astrometry used to derive mas-level variations are presented in Andrei et al. (2011). A full analysis of the program itself can be found in Andrei et al. (2011). Here we present the results regarding the two selected sources we considered in this study.

Table 5.3 presents the timeline variation in position and magnitude for quasars J121855.80+020002.1 ($z = 0.327$, $18^m.1$) and J162011.28+172427.5 (Mrk 877, $z = 0.112438$, $16^m.2$), and Fig. 5.5 illustrates the observed astrometric variability of the photocenter.

Table 5.3 The summary of the measurements of the offset of photocenter: Col. 1 - the mean epoch of observation; Col. 2 - the time interval in days between each measurement; Col. 3 - the X-direction (basically RA) astrometric variation in mas from the previous measurement ; Col. 4 - the Y-direction (basically DEC) astrometric variation in mas from the previous measurement; Col. 5 - the magnitude variation given in tenths of magnitude from the previous measurement. In the first lines, the values correspond to the offsets to the nominal CDS references. In the subsequent lines, we present the offsets to the previous line values. The combined corresponding errors (σ) are given.

SDSS J121855.80+020002.1, z = 0.327, MAG$_R$ = $18^m.1$

DATE	DAYs	ΔRA$\pm\sigma$ (mas)	ΔDE$\pm\sigma$ (mas)	ΔMAG$_R \pm \sigma$ (10^{-1})
2008.016	0.0	-11±3	- 3±2	-0.420±0.009
2008.163	53.4	+15±3	+ 4±2	+0.134±0.007
2008.263	36.8	+ 6±2	- 3±1	-0.917±0.011
2008.415	55.4	- 4±1	+ 1±1	+1.774±0.012
2008.970	202.7	- 8±1	+ 4±1	-1.773±0.007
2009.382	150.5	0±4	- 3±2	+2.070±0.011

SDSS J162011.28+172427.5, z = 0.112, MAG$_R$ = $16^m.2$

DATE	DAYs	ΔRA$\pm\sigma$ (mas)	ΔDE$\pm\sigma$ (mas)	ΔMAG$_R \pm \sigma$ (10^{-1})
2007.277	0.0	-17±10	+24±22	-0.136±0.007
2007.430	58.8	+ 2±9	0±24	+0.032±0.007
2008.415	356.9	+14±6	+ 4±21	+0.021±0.006
2008.647	84.9	-23±8	-59±16	+0.002±0.005
2009.181	195.1	+76±19	+36±15	+0.550±0.023
2009.382	73.3	-47 ±18	-58±22	-0.560±0.023

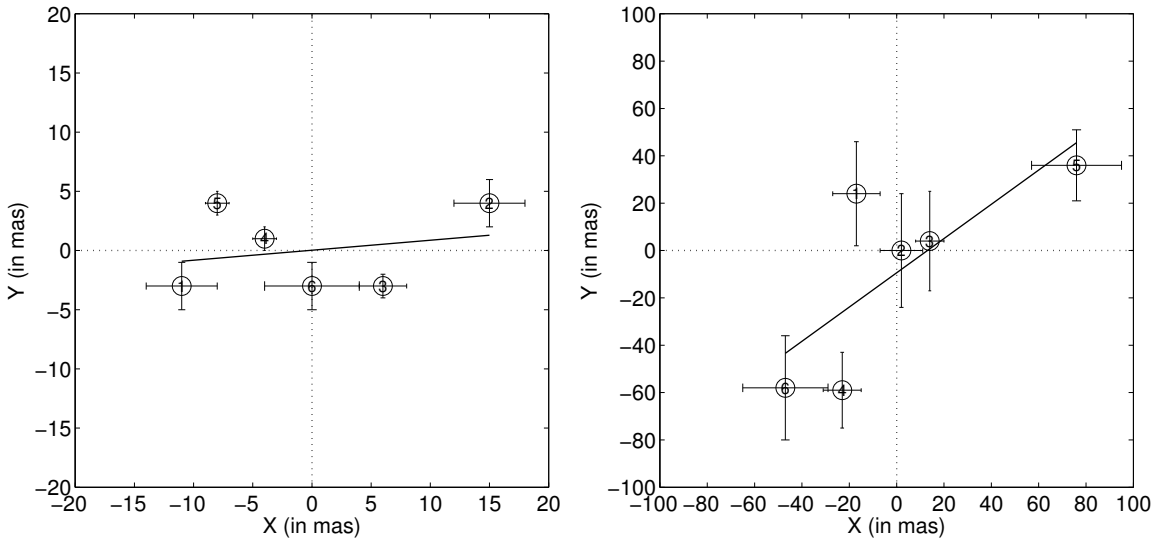

Figure 5.5 Observed astrometric variability of the photocenter, measured for SDSS J121855.80+020002.1 at $z = 0.327$ (left) and SDSS J162011.28+172427.5 at $z = 0.112438$ (right), during the period 2007-2009 (see Table 5.3). The straight solid lines in the panels represent linear fits through the observed positions. Notations of points from 1 to 5 correspond to the observational epochs from first to the last as given in Table 5.3.

5.4.2 Comparison between the simulated and the observed variations

Both observed objects have broad lines (i.e. they are type 1 AGN). In our simulations of dusty torus, we found that the photocenter offset is significant only when the central source is partly obscured by the dust. Therefore, there is a small chance that the observed variations are caused by changes in the torus structure.

To explore whether the observed variations in SDSS J121855.80+020002.1 and SDSS J162011.28 +172427.5 are caused by perturbations in the accretion disk, we first estimated the masses of the black holes (M_{BH}) for these two objects. We used spectra observed with HST (for SDSS J121855.80+020002.1) and from SDSS database (for SDSS J162011.28+172427.5). After measuring the full width at half maximum (FWHM), we used the three estimators M_S, M_V and M_N, given by Shields et al. (2003), Vestergaard & Peterson (2006), and Netzer & Trakhtenbrot (2007), respectively. The estimated masses for SDSS J121855.80+020002.1 are: $M_S = 9.18 \times 10^8\ M_\odot$, $M_V = 1.37 \times 10^9\ M_\odot$, and $M_N = 1.10 \times 10^9\ M_\odot$, or on average $M_{BH} = (1.13 \pm 0.23) \times 10^9\ M_\odot$. In the same way, we estimated the black hole masses of SDSS J162011.28+172427.5 to be $M_S = 3.51 \times 10^8\ M_\odot$, $M_V = 5.25 \times 10^8\ M_\odot$, $M_N = 3.72 \times 10^8\ M_\odot$, or on average $M_{BH} = (4.16 \pm 0.95) \times 10^8\ M_\odot$. For these values of M_{BH} the predicted values of the photocenter offset due to the perturbations in accretion disk are below mas (Table 5.1). Therefore, changes in accretion disk are not a likely cause of the observed variations.

To further estimate the possibility that the photocenter variability is caused by perturbation in

the disk, or in the BLR, we calculated dimensions of the BLR of these two objects, using the relation between the BLR radius and luminosity at 5100 Å (see e.g. Vestergaard & Peterson, 2006). We estimated the BLR sizes for SDSS J121855.80+020002.1 to be around 113 light days (that is $\sim$ 0.02 mas) and for SDSS J162011.28 +172427.5 10 light days ($\sim$ 0.004 mas). Therefore, the observed photocenter variability cannot be explained by the perturbation in the BLR.

5.4.3 Possible explanation of the photocenter variability

As shown, a perturbation in the accretion disk cannot explain the photocenter jitter observed in the two quasars. Moreover, we have estimated that the BLR in both objects is very compact, around 10^{-5} – 10^{-6} arcsec (that translates into light day to several hundred light day scale), which is inconsistent with the photocenter variations. We note that these compact regions cannot be resolved by Gaia, as its PSF will be $\sim$ 200 mas.

For objects that are partially obscured by dust, a variation in both the central luminosity and the dust sublimation radius may produce an offset in the photocenter (at $z = 0.1$, see Table 5.2), of about one milli-arcsec. However it cannot explain the photocenter variations of the two quasars under study, as the jitter is smaller, and they both exhibit broad emission lines, which implies that they have a geometry where obscuration is very small or nonexistent.

Another possible source of photocenter variability are "nuclear" super-novae. Several studies (see e.g. Cid Fernandes et al., 2004; Davies et al., 2007; Popović et al., 2009, etc.) demonstrate that AGN may be associated with star formation regions. For instance Davies et al. (2007) found that on kpc (or pc) scales (corresponding to the observed photocenter variation in our objects) the luminosity of the starburst component may be comparable to that of the AGN.

For the (U)LIRGs (ultra luminous infrared galaxies), the expected supernova rate is very high, as high as 2.4 yr^{-1}, if the infrared luminosity is produced entirely by starbursts (see Mannucci et al., 2003). In the extreme case of this kind of objects, a large supernova rate (SNr) may have influence on the stability of the photocenter. We estimate the SNr, considering the relation given in Mattila & Meikle (2001), and assuming that the SNr and the star formation rate (SFR) are correlated (Mannucci et al., 2003), the latter calculated using the luminosity of the Hα line (Calzetti et al., 2007). We could only calculate the SNr for SDSS J121855.80+020002, because we do not have Hα spectral data for J162011.28+172427.5. We obtained SFR $\approx$ 14.7 yr^{-1} and a corresponding SNr $\approx$ 0.1 yr^{-1} (i.e. one SN every ten years) for SDSS J121855.80+020002. We conclude that it is unlikely that supernovae are responsible for the photocenter shift of this object.

We now discuss a scenario where the photocenter jitter might be related to the jet emission. In terms of radio loudness (Kellermann et al., 1989), i.e. $R = F_{5GHz}/F_{Bband} > 10$, SDSS

J121855.80+020002.1 has a value of $R \sim 1.1$ (Rafter et al., 2009), and J162011.28+172427.5 has $R \sim 0.41$ (Sikora et al., 2007), very far from the values shown by radio loud quasars, which tend to have relativistic jets. Radio-quiet objects can have jet emission (e.g. Mrk 348, see Anton et al., 2002), though their radio-brightness can be significantly higher (Anton et al., 2002) than that of the objects under study. There are VLA 1.4 GHz maps at the position of our sources. The FIRST map of SDSS J121855.80+020002 shows a faint core-morphology on the 1 mJy level, and in the case of J162011.28+172427.5 there is no detection with NRAO VLA Sky Survey (NVSS) at the position of the optical source. We conclude that there is no evidence that the jet plays a role in the photocentric variation of these objects.

It is interesting that in the both objects (see Fig. 5.5) the photocenter offset is almost aligned, especially in SDSS J121855.80+020002, with a straight line. These aligned positions of the photocenter offset may correspond to two variable sources close to each other, with the photocenter always shifting towards the brighter of the two. A speculative possibility is a binary supermassive black-hole system (of the type discussed in e.g., Lauer & Boroson, 2009; Bogdanović et al., 2009; Shields et al., 2010; Barrows, 2011; Popović, 2012), based on the observations of double-peaked narrow and broad lines. We note that the broad-line shapes of the objects under study are complex and can be properly fitted with two broad Gaussians that are shifted (toward either the blue or red) with respect to the central narrow component (see Fig. 7. in Popović et al., 2012). In Popović et al. (2000) and Shen & Leob (2010), a binary broad emission-line region has been investigated, and the line profiles of this system have been discussed. To detect two peaks in the broad line profile, it is necessary to be able to resolve the two BLRs, and the plane of the orbit must be edge-on with respect to the line of observation. An asymmetric line profile might result solely from a system where the two BLRs have different dimensions and luminosities (see Figs. 4-8 in Popović et al., 2000). Such a system might exist at the center of our two observed quasars, and may be the cause of their photocenter variability.

We note that in addition to the binary black hole scenario, the superposition of two visually close and variable sources (see the several examples presented in Popović, 2012) can explain an aligned variability. All of these scenarios should be considered in future investigations.

5.5 Conclusions

We have simulated the perturbation in the inner structure of quasars (bright spots in the accretion disk and changes in the dusty torus structure), to find how much these effects can offset their photocenters, and try to determine whether it will be observable with future Gaia mission. We have considered two quasars which photocenter variations have been observed, in order to compare them with our simulations. From our investigations, we draw the following conclusions (Popović et al., 2012):

(i) Perturbations (or bright spots) in an accretion disk may cause an offset of the photocenter, and this effect has a good chance of being detected by the Gaia mission. The most likely candidates are low-redshifted AGNs with massive black holes (10^9-10^{10}) that are in principle very bright objects. One can expect a maximal offset of the center (in the case of a bright spot located at the edge of the disk) on the order of a few mas.

(ii) A photocenter offset can be caused by changes in the torus structure due to different illuminations of the torus when the central source is obscured by the dust. A maximal offset can be several mas, which will also be detectable with Gaia.

(iii) A photocenter offset caused by both effects is connected to the photometric variation in the quasars, but there is a small probability of a correlation between astrometric and photometric variations. We note here that quasars with a high photometric variability are not good objects for constructing the optical reference frame.

(iv) To exclude the possibility of the photocenter variation being caused by a perturbation in the accretion disk, or in the BLR, one may estimate the dimensions of the BLR and choose objects with a compact BLR. However, to avoid any variation in the photocenter caused by filaments in the torus, it is preferable to choose quasars with face-on oriented tori.

(v) The observed photocenter variability of two quasars cannot be explained by the variation in their inner structure (accretion disk and torus). It seems that the observed photocenter variation can be reproduced very well by a scenario with double variable sources at the center of these objects. It may indicate (as well as complex broad line shapes) that these objects are good candidates for binary black hole systems.

At the end, we conclude that Gaia, in addition to providing astrometrical measurements, may be very useful for an astronomical investigation of the inner quasar structure (physical processes), especially in low redshift variable sources.

6 Summary

6.1 Active galactic nuclei

Nowadays it is widely accepted that every massive galaxy harbors a supermassive black hole (SMBH) at its center. A number of apparent correlations between SMBH mass and host galaxy structural and dynamical properties have been observed. The correlation between the masses of SMBHs and the bulges of their host galaxies suggests a link between their growth (Kormendy & Richstone, 1995; Kormendy & Gebhardt, 2001). An active galactic nucleus (AGN) represents a phase in the life of a galaxy, during which the SMBH growth is directly observable. The term AGN encompasses a variety of energetic phenomena in galactic centers, triggered by matter spiralling into a SMBH at a relatively high rate.

The radiation coming from AGNs originates in the conversion of gravitational potential energy into thermal energy, as matter spirals towards the SMBH through an accretion disk (Lynden-Bell, 1969). Their luminosity can be up to 10,000 greater than the total luminosity of a normal galaxy. The radiated AGN continuum covers a broad spectrum, from the X-ray to the radio domain, it is partially polarized and variable in time. Radiation from the central engine is ionizing the surrounding medium, creating conditions for a strong emission line spectrum, superimposed on the continuum. Sometimes, highly collimated and fast outflows ("jets") emerge perpendicular to the accretion disk.

Since the discovery by Keel (1980) that the orientation of Seyfert 1 galaxies is not random, it has been recognized that the appearance of an AGN varies with the viewing angle. This has led to the picture of "orientation unification" (see Antonucci, 1993; Urry & Padovani, 1995) where the structure of AGNs is believed to be basically similar but what we see is a strong function of orientation (see Fig. 6.1). In this unified model, the central black hole is surrounded by a geometrically-thin accretion disk that is the source of the strong X-ray emission and UV/optical continuum (see Jovanović, 2012, and references therein). Above and below the disk is the broad-line region (BLR), a turbulent, rapidly-moving, and dense emission-line gas orbiting the black hole (see Gaskell, 2009, for a review). Both the accretion disk and the BLR are surrounded by a geometrically- and optically-thick, roughly toroidal structure of dust and gas (the "dusty torus"), which is absorbing the incoming radiation and re-emitting it in the infrared (IR). In addition to these components, there is lower density, more slowly moving gas present on a scale similar to or significantly larger than that of the torus. This gas can be seen when it is illuminated by the cone of ionizing radiation emanating from inside the torus. It is a source of narrow emission lines and thus is know as the "narrow-line region" (NLR). The broad emission lines and the thermal continuum emission can only be seen when the torus is close to face-on and thus, such an object appears as a type 1 active galaxy. When the orientation is close to edge-on, the dusty torus blocks the radiation coming from the accretion disk and the BLR. In this case, the UV/optical bump and broad emission lines are absent and the object appears as a type 2 active

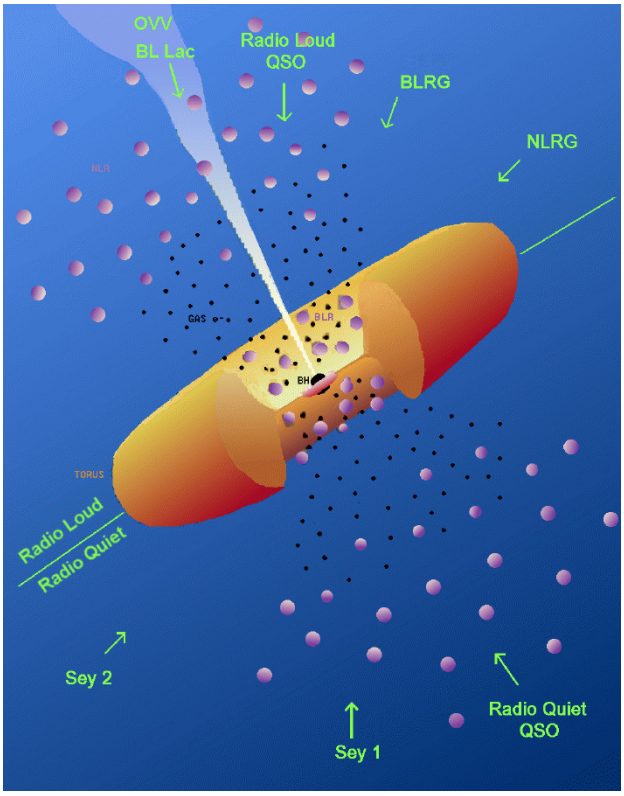

Figure 6.1 The standard AGN unification scheme. Depending on the orientation, an observer will see different emitting regions and thus, an intrinsically same objects would appear to him as different type of AGN (M. Polletta, adapted from Urry & Padovani, 1995).

galaxy. If a jet of matter, ejected perpendicular to the accretion disk is present, then viewing such an object along the jet would exhibit strong non-thermal, polarized and rapidly variable continuum (see Antonucci, 2012 for an in-depth discussion on different types of AGN).

The masses of SMBHs can be readily estimated in some types of AGN, (Dibai, 1977) and AGNs are currently our only way of studying the evolution of SMBHs over cosmic time. Furthermore, the brightest AGNs are the most luminous quasi-steady compact sources of radiation in the universe, and hence they are valuable probes of cosmic evolution up to very high redshifts. In order to understand black hole growth across cosmic time and the connection between galaxies and black holes, we need to understand how AGNs work. We need to test the basic picture outlined above, and, in particular, to be able to explain observations which presently challenge this picture and might force modifications of it.

The scope of this thesis The aim of this thesis was to take a step forward towards a better understanding of the AGN structure, focusing on the dusty torus. This dusty torus has a major effect on the appearance of an AGN. The matter that is feeding a SMBH through an accretion disk comes from the dusty torus. Although the torus is a vital component of an AGN, it is still

not understood well enough. The basic picture has been clear for some time, but there are still many unresolved issues. The intensity and shape of the observed silicate features, at 10 and 18 μm, which represent an unique window into the dust distribution and chemical composition, do not match the theoretical expectations. Another common problem reported in many works is the lack of near-IR emission when trying to apply the state-of-the art models of torus to the observed infrared spectral energy distributions (SEDs) of AGNs. Other unresolved questions include the origin and formation of the torus, and the question how the required scale height is maintained. Although the main focus of this research was on modeling and analyzing the dusty torus, we also investigated some related phenomena, such as perturbations in accretion disk. We have applied the developed models of the torus and disk in the investigation of microlensing effects and photometric variability of quasars. Here we present a brief summary of the research for this thesis and outline the most important conclusions.

The dusty torus We introduced a new, physically-motivated model for the dusty torus as a clumpy two-phase medium, with high-density clumps and low-density medium filling the space between them. We used the 3D Monte Carlo radiative transfer code SKIRT (Baes et al., 2003, 2011) to obtain SEDs and images of the torus at different wavelengths. We calculated a grid of models for different parameters, analyzed the properties of IR emission and compared them to the properties of the corresponding sets of clumps-only models and models with a smooth dust distribution. From our analysis, we found the following (Stalevski et al., 2011, 2012a):

(i) The shape and amount of near- and mid-infrared emission are determined by the conditions of the dust in the innermost region of the torus: different random distributions of the clumps may result in the very different SEDs in otherwise identical models.

(ii) The dust distribution, the optical depth, the clump size and the actual arrangement of the clumps in the innermost region all have an impact on the appearance of the 10 μm silicate feature. The silicate feature is naturally suppressed in clumpy models, but models with a smooth dust distribution are also able to produce a wide range of silicate feature strengths.

(iii) Low-density dust, distributed smoothly between clumps, significantly contributes to the near-infrared emission. Therefore, having the dust distributed in such a two-phase medium might offer a natural solution to the problem reported in many papers – the lack of emission in the near-infrared when fitting observed SEDs with other clumpy models from the literature.

A different behavior of near- and mid-infrared emission in the two-phase, clumps-only and smooth models is illustrated in Fig. 6.2.

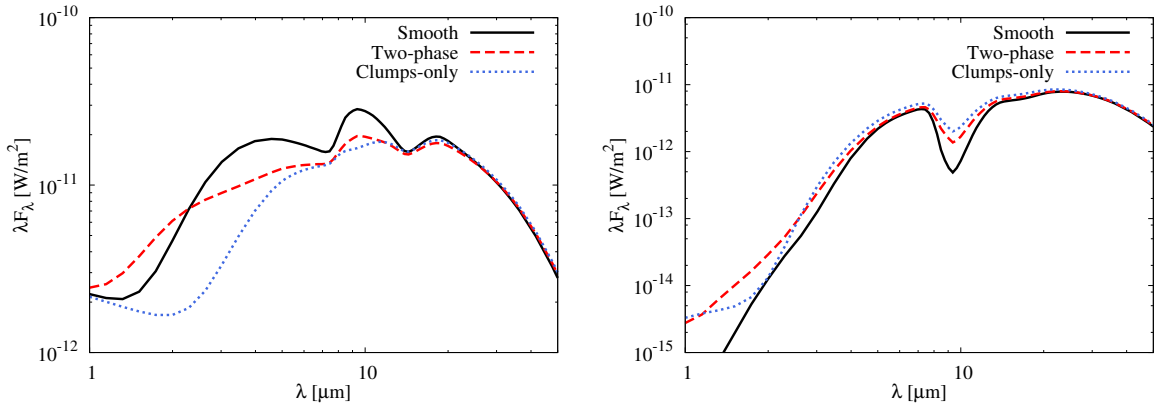

Figure 6.2 Comparison of the smooth, two-phase and clumps-only model SEDs for typical torus parameters. Full solid line represents smooth model, dashed line two-phase model and dotted line clumps-only model. *Left panel*: face-on view; *right panel*: edge-on view.

The influence of microlensing Gravitationally lensed systems with multiple images represent a powerful tool to study the size and structure of both the galaxy which acts as the lens and the background source. However, in a number of lensed systems in which a quasar is the source, the flux ratios between the lensed quasar images deviate from those predicted by simple lens models. When investigating this flux ratio anomaly, it is important to determine the true flux ratios between the images, in the absence of microlensing. In principle, this could be done by looking at the emission-line, infrared, and radio-emitting regions of quasars, as they all should be large enough to safely disregard microlensing effects. However, none of the works presented in the literature so far, has exploited a realistic torus model in microlensing studies. We have used our two-phase models of dusty tori as sources, generated magnification maps and simulated microlensing by stars in the lens galaxy, in order to estimate if microlensing can significantly affect the infrared emission. From our investigation, we conclude the following (Stalevski et al., 2012b):

(i) Despite their large size, AGN dusty tori could be significantly magnified by microlensing in some cases. As the size of torus is wavelength dependent, the amplitude of magnification strongly depends on wavelenght as well (see Fig. 6.3). The magnification is the highest in the near-infrared, decreases rapidly towards the mid-infrared range, and stays almost constant in the far-infrared part of SED.

(ii) As microlensing is sensitive to the size of the source, parameters determining the geometry and the apparent size of the torus have a very important role. Tori with $R_{\rm out} \lesssim 10$ pc could be appreciably microlensed.

(iii) Estimated rise times, between the beginning and the peak of high magnification events, range from several decades to several hundreds of years.

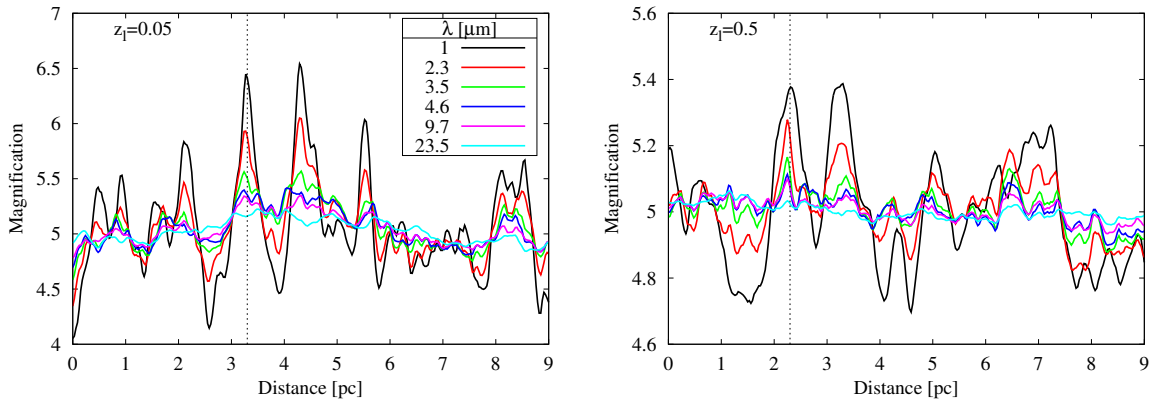

Figure 6.3 Simulated microlensing light curves for different rest-frame wavelengths (indicated in the legend), for lens galaxy at redshift of 0.05 (left panel) and 0.5 (right panel). Note the different range of y axis shown in the two panels.

Given such long time-scales, microlensing would hardly prove to be a practical tool to study and constrain the properties of dusty tori, as it is in the case of AGN accretion disks. However, the results of our study should be kept in mind when investigating the flux ratio anomaly of lensed quasar images in different wavelength bands. We have shown that the infrared emission of dusty tori could be significantly microlensed in some cases, and thus, it is a less reliable tool for determining the "intrinsic" flux ratios.

Perturbations in the accretion disk Some physical considerations indicate that the variability of the accretion disk has to be highly non-axisymmetric. A wide range of AGN puzzles can be solved by a non-axisymmetric variability. If off-axis variability is important, this has significant implications for using reverberation mapping to probe the structure of AGNs, and for searches for binary SMBHs. We have modeled such non-axisymmetric emissivity perturbations in the form of a bright spot in the accretion disk. The developed model was applied to the observed Hβ line profiles of the quasar 3C 390.3. From this investigation we point out the following results (Jovanović et al., 2010; Stalevski et al., 2010):

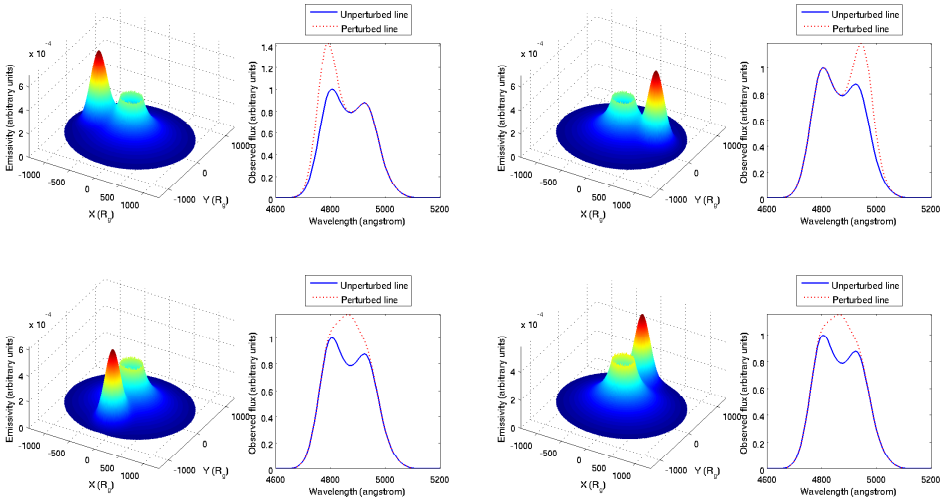

Figure 6.4 Shapes of perturbed emissivity of an accretion disk and the corresponding perturbed (dashed line) and unperturbed (solid line) Hβ line profiles. Depending on the position of a bright spot, it affects only one of the wings of the line, or the line core.

(i) The model of emissivity perturbations as a bright spot in the accretion disk can successfully explain the different shapes and the variability of double peaked line profiles (see Fig. 6.4).

(ii) Using this model of a perturbing region, we were able to successfully model and reproduce the observed variations of the Hβ line profile in the case of 3C 390.3, including the two large amplitude outbursts observed during the analyzed period.

(iii) Our results support the hypothesis that perturbations in the accretion disk emissivity are probably caused by fragments in the spiral arms of the disk.

Photocentric variability of quasars We have used the developed models of the dusty torus and accretion disk with a perturbing region to study variations of quasar photocenters, caused by an outburst of accretion disk luminosity and changes in the torus structure of torus, in the context of the future Gaia mission. Gaia is a global astrometric interferometric mission that aims to determine high-precision astrometric parameters for one billion objects. It is foreseen that 500,000 quasars will be among these objects. These quasars will be used to construct a dense, optical quasar-based celestial reference frame. We have considered perturbations in the accretion disk and changes in the pattern of radiation scattered by the dust particles in the surrounding torus. We estimated how much these effects may contribute to the variability of the photocenter and the possibility of detecting this effect with the Gaia mission. From our investigation, we drew the following conclusions (Popović et al., 2012):

(i) Perturbations in the accretion disk may cause an offset of the photocenter, and this effect has a good chance of being detected by the Gaia mission. The expected maximal offset of the center (in the case of a bright spot located at the edge of the disk) is on the order of a few mas.

(ii) A photocenter offset can be caused by changes in the torus structure due to different illuminations of the torus when the central source is obscured by the dust. A maximal offset can be several mas, which will also be detectable with Gaia.

(iii) The observed photocenter variability of two observed quasars cannot be explained by the variation in their inner structure (accretion disk and torus). It seems that the observed photocenter variation can be reproduced very well by a scenario with double variable sources at the center of these objects. This may indicate (as well as the complex broad line shapes) that these objects are good candidates for binary black hole systems.

6.3 Future work

The research conducted in the scope of this thesis is a part of an on-going investigation, which will be continued along the lines presented below.

Radiative transfer modeling of the dusty torus. We have shown that treating the dusty torus as a multiphase medium represents a step forward towards a solution of some issues, such as the lack of the near-infrared emission. To further validate this, more detailed models are needed. Also, although current modeling is able to reproduce a wide range of the silicate feature intensities, its exact shape and position in a number of observed objects still remains unexplained and deserves further investigation. Therefore, we will continue and expand the work on modeling of the dusty torus. The radiative transfer code SKIRT is being very actively developed, led by Prof. Maarten Baes and his group (Ghent University, Belgium). The improvements being implemented will enable us to produce more detailed models of the dusty torus. Among other improvements, an adaptive grid for the dust cells will guarantee that all the dust cells are optically thin. This will, in turn, ensure that the temperature is properly sampled and consequently, that the shape and intensity of the silicate feature, which drastically depends on the temperature, are correctly reproduced. A large grid of models will be calculated. The analysis of the model properties and comparison with observed infrared SEDs will allow a deeper insight into the structure of the torus. The database of models will be continually updated and will be made publicly available for other interested researchers.

Modeling complex dust distributions and geometries. Wada & Norman (2002), with model update in Wada et al. (2009) and Wada (2012), performed 3D hydrodynamical simulations of the interstellar medium around an AGN, taking into account self-gravity of the gas, radiative cooling and heating due to supernovae. They found that such a turbulent medium would produce a multi-phase filamentary (sponge-like) structure. In a collaboration with this group, we will use these results to calculate the corresponding dust density distributions. The goal is to analyze and compare properties of SEDs and images in the infrared of such a realistic dust distributions in AGNs. Since the simulations of Wada et al. are on the scale of up to several hundreds of parsecs, we could also analyze contribution of other regions, placed further away (e.g., star forming regions), to the IR SEDs of AGNs.

Gravitationally-lensed quasars. When investigating the flux ratio anomaly of lensed quasars, it is important to determine the true magnification ratios between the images, in the absence of other effects which might contaminate it. Therefore, we will continue and expand the presented microlensing study with investigation of milli- and strong-lensing effects, using updated models

of the dusty torus. To date, there have been only limited efforts, with simple or toy models, to study the source size effects in millilensing. Thus, using realistic and physically motivated models of the dusty torus, which are demonstrating wavelength dependency of the size, will present a significant improvement of our understanding of the flux ratio anomaly. Consequently, it will allow us to constrain the size and mass of the lens substructure better, and thus to further evaluate the hypothesis that the substructure inferred from the flux ratio anomalies is actually the substructure predicted by ΛCDM cosmological model.

Bibliography

Abajas C., Mediavilla E., Muñoz J. A., Popović L. Č., Oscoz A., 2002, ApJ, 576, 640

Agol E., Jones B., Blaes O., 2000, ApJ, 545, 657

Agol E., Gogarten S. M., Gorjian V., Kimball A., 2009, ApJ, 697, 1010

Alonso-Herrero A., Quillen A. C., Rieke G. H., Ivanov V. D., Efstathiou A., 2003, AJ, 126, 81

Alonso-Herrero A., Ramos Almeida C., Mason R., Asensio Ramos A., Roche P. F., Levenson N. A., Elitzur M., Packham C., Rodríguez Espinosa J. M., Young S., Díaz-Santos T., Pérez-García A. M., 2011, ApJ, 736, 82

Andrei, A.H., Bouquillon, S., Camargo, J.I.B., Penna, J.L., Taris, F., Souchay, J., Silva Neto, da D.N., Vieira Martins, R., Assafin, M., 2009, Proc. of the "Journes 2008 Systmes de refrence spatio-temporels", M. Soffel and N. Capitaine (eds.), Lohrmann-Observatorium and Observatoire de Paris.

Andrei, A.H., et al. 2012 in preparation.

Antonucci R., 1993, ARA&A, 31, 473

Antonucci, R. 2012, to be published in Astronomical and Astrophysical Transactions, arXiv:1210.2716

Antonucci R. R. J., Miller J. S., 1985, ApJ, 297, 621

Anton, S., Thean, A. H. C., Pedlar, A., Browne, I. W. A. 2002, MNRAS, 336, 319

Aretxaga I., Joguet B., Kunth D., Melnick J., Terlevich R. J., 1999, ApJL, 519, L123

Baes M., 2008, MNRAS, 391, 617

Baes M., Davies J. I., Dejonghe H., Sabatini S., Roberts S., Evans R., Linder S. M., Smith R. M., de Blok W. J. G., 2003, MNRAS, 343, 1081

Baes M., Dejonghe H., 2001, ApJ, 563, L19

Baes M., Dejonghe H., 2002, MNRAS, 335, 441

Baes M., Dejonghe H., Davies J. I., 2005a, AIPC, 761, 27

Baes M., Fritz J., Gadotti D. A., Smith D. J. B., Dunne L., da Cunha E., Amblard A., et al. 2010, A&A, 518, L39

Baes M., Stamatellos D., Davies J. I., Whitworth A. P., Sabatini S., Roberts S., Linder S. M., Evans R., 2005b, NewA, 10, 523

Baes M., Verstappen J., De Looze I., Fritz J., Saftly W., Vidal Pérez E., Stalevski M., Valcke S., 2011, ApJS, 196, 22

Bao, G., Hadrava, P., Ostgaard, E. *ApJ*, 1994, *435*, 55

Baptista, R. & Catalán, M. S. 2000, NewAR, 44, 1P

Barrows, R. S., Lacy, C. H. S., Kennefick, D., Kennefick, J., Seigar, M. S. 2011, New Ast., 16, 122

Barvainis R., 1987, ApJ, 320, 537

Bate N. F., Floyd D. J. E., Webster R. L., Wyithe J. S. B., 2008, MNRAS, 391, 1955

Beckert T., Duschl W. J., 2004, A&A, 426, 445

Bianchi S., 2008, A&A, 490, 461

Bianchi, S., Ferrara, A., & Giovanardi, C. 1996, ApJ, 465, 127

Bjorkman J. E., Wood K., 2001, ApJ, 554, 615

Blackburne, J. A., & Kochanek, C. S. 2010, ApJ, 718, 1079

Blackburne J. A., Pooley D., Rappaport S., Schechter P. L., 2011, ApJ, 729, 34

Bogdanović, T., Eracleous, M., Sigurdsson, S. 2009, ApJ, 697, 288

Bon, E., Gavrilović, N., La Mura, G., Popović, L. Č. 2009a NewAR, 53, 121

Bon, E., Popović, L. Č., Gavrilović, N., La Mura, G., Mediavilla, E. 2009b, MNRAS, 400, 924

Bourda G., Charlot P., Porcas R.W., Garrington S.T. 2010, A&A, 520, A113

Bromley, B.C., Chen, K., Miller, W.A. *ApJ*, 1997, *475*, 57

Browne, I. W. A. 1983, MNRAS, 204, 23P

Calzetti, D., Kennicutt, R. C., Engelbracht, C. W., et al. 2007, ApJ, 666, 870

Cao, S., Covone, G., & Zhu, Z.-H. 2012, ApJ, 755, 31

Cashwell, E. D., & Everett, C. J., 1959, A Practical Manual on the Monte Carlo Method for Random Walk Problems, Pergamon, New York

Čadež, A., Fanton, C., Calivani, M. *New Astronomy*, 1998, *3*, 647

Chang, K., & Refsdal, S. 1979, Nature, 282, 561

Chang, K., & Refsdal, S. 1984, A&A, 132, 168

Chen, K., Halpern, J. P. & Filippenko, A. V. 1989, ApJ, 339, 742

Chen, K. & Halpern, J. P. 1990, ApJ, 354, L1

Chiba M., Minezaki T., Kashikawa N., Kataza H., Inoue K. T., 2005, ApJ, 627, 53

Cid Fernandes, R., Gu, Q., Melnick, J., et al. 2004, MNRAS, 355, 273

Collin-Souffrin, S. 1987, A&A, 179, 60

Collin-Souffrin, S., & Dumont, A. M. 1990, A&A, 229, 292

Courbin, F., Saha, P., & Schechter, P. L. 2002, Gravitational Lensing: An Astrophysical Tool, Lecture Notes in Physics, Berlin Springer Verlag, 608, 1

Dai X., Kochanek C. S., Chartas G., Kozłowski S., Morgan C. W., Garmire G., Agol E., 2010, ApJ, 709, 278

Davis S. W., Laor A., 2011, ApJ, 728, 98

Davies, R. I., Mueller-Sanchez, F., Genzel, R., et al. 2007, ApJ, 671, 1388

de Looze I., Baes M., Zibetti S., Fritz J., Cortese L., Davies J. I., Verstappen J., et al. 2010, A&A, 518, L54

Deo, R. P., Richards, G. T., Nikutta, R., Elitzur, M., Gallagher, S. C., Ivezić, Ž., & Hines, D. 2011, ApJ, 729, 108

Dexter, J., & Agol, E. 2011, ApJL, 727, L24

Dibai, E. A. 1977, Soviet Astronomy Letters, 3, 1

Dobler G., Keeton C. R., 2006, MNRAS, 365, 1243

Dovčiak, M., Karas, V., Matt, G., Goosmann, R. W. 2008, MNRAS, 384, 361

Dullemond C. P., van Bemmel I. M., 2005, A&A, 436, 47

Dumont, A. M., & Collin-Souffrin, S. 1990a, A&A, 229, 302

Dumont, A. M., & Collin-Souffrin, S. 1990b, A&A, 229, 313

Dumont, A. M., & Collin-Souffrin, S. 1990c, A&AS, 83, 71

Efstathiou A., Rowan-Robinson M., 1995, MNRAS, 273, 649

Elíasdóttir, Á., Hjorth, J., Toft, S., Burud, I., & Paraficz, D. 2006, ApJS, 166, 443

Elitzur, M. 2007, The Central Engine of Active Galactic Nuclei, ASP Conference Series, 373, 415

Elitzur, M. 2012, ApJL, 747, L33

Eracleous, M. & Halpern, J. P. 1994, ApJS, 90, 1

Eracleous, M. & Halpern, J. P. 2003, ApJ, 599, 886

Eracleous, M., Livio, M., Halpern, J. P. & Storchi-Bergmann, T. 1995, ApJ, 438, 610

Eracleous, M., Halpern, J. P., Gilbert, A. M., Newman, J. A., & Filippenko, A. V. 1997, ApJ, 490, 216

Eracleous, M., Lewis, K. T. & Flohic, H. M. L. G. 2009, New Astronomy Review, 53, 133

Fadely R., Keeton C. R., 2011, AJ, 141, 101

Fanton, C., Calivani, M., Felice, F., Čadež, A. *PASJ*, 1997, *49*, 159

Feltre, A., Hatziminaoglou, E., Fritz, J., & Franceschini, A. 2012, MNRAS, 426, 120

Fischer, O., Henning, T., & Yorke, H. W. 1994, A&A, 284, 187

Flohic, H. M. L. G., Eracleous, M. 2008, ApJ, 686, 138

Fritz J., Franceschini A., Hatziminaoglou E., 2006, MNRAS, 366, 767

Garsden, H., Bate, N. F., & Lewis, G. F. 2011, MNRAS, 418, 1012

Gaskell, C. M. 1996, ApJL, 464, L107

Gaskell, C. M. 2008, Revista Mexicana de Astronomia y Astrofisica Conference Series, 32, 1

Gaskell, C. M. 2009, NewAR, 53, 140

Gaskell, C. M. 2010, arXiv:1008.1057

Gaskell, C. M. 2011, Baltic Astronomy, 20, 392

Gaskell, C. M., Klimek, E. S., & Nazarova, L. S. 2007, Bulletin of the American Astronomical Society, 39, #118.02

Gezari, S., Halpern, J. P., Eracleous, M. 2007, ApJS, 169, 167

Gilbert, A. M., Eracleous, M., Filippenko, A. V. & Halpern, J. P. 1999, in ASP Conf. Ser. 175: Structure and Kinematics of Quasar Broad Line Regions, ed. Gaskell, C. M., Brandt, W. N., Dietrich, M., Dultzin-Hacyan, D. & Eracleous, M. (San Francisco: ASP), 189

Gil-Merino R., Wambsganss J., Goicoechea L. J., Lewis G. F., 2005, A&A, 432, 83

Goldberg D. M., Chessey M. K., Harris W. B., Richards G. T., 2010, ApJ, 715, 793

Gordon K. D., Misselt K. A., Witt A. N., Clayton G. C., 2001, ApJ, 551, 269

Granato G. L., Danese L., 1994, MNRAS, 268, 235

Hao L., Spoon H. W. W., Sloan G. C., Marshall J. A., Armus L., Tielens A. G. G. M., Sargent B., van Bemmel I. M., Charmandaris V., Weedman D. W., Houck J. R., 2005, ApJL, 625, L75

Ho, L. C., Filippenko, A. V., & Sargent, W. L. W. 1993, ApJ, 417, 63

Ho, L. C., Filippenko, A. V., & Sargent, W. L. W. 1997, ApJ, 487, 568

Hony, S., Kemper, F., Woods, P. M., et al. 2011, A&A, 531, A137

Hönig S. F., Beckert T., Ohnaka K., Weigelt G., 2006, A&A, 452, 459

Hönig S. F., Kishimoto M., 2010, A&A, 523, A27+

Ingrosso, G., Novati, S. C., de Paolis, F., et al. 2009, MNRAS, 399, 219

Inoue K. T., Chiba M., 2005, ApJ, 634, 77

Ivezić, Z., & Elitzur, M. 1997, MNRAS, 287, 799

Jaffe W., Meisenheimer K., Röttgering H. J. A., Leinert C., Richichi A., Chesneau O., Fraix-Burnet D., Glazenborg-Kluttig A., Granato G., Graser U., Heijligers B., Köhler R., Malbet F., et al. M., 2004, Nature, 429, 47

Jarosik, N., Bennett, C. L., Dunkley, J., et al. 2011, ApJS, 192, 14

Johnston, K. J., Boboltz, D., Fey, A., Gaume, R., Zacharias, N., 2003, SPIE.4852, 143

Jonsson, P. 2006, MNRAS, 372, 2

Jovanović, P. 2012, NewAR, 56, 37

Jovanović, P., Popović, L. Č. 2008a, Fortschritte der Physik, 56, 456

Jovanović, P., Popović, L. Č. 2008b, POBeo, 84, 467

Jovanović, P., Popović, L. Č. 2009a, chapter in the book ”Black Holes and Galaxy Formation”, eds. A. D. Wachter and R. J. Propst by Nova Science Publishers, Inc., 249-294

Jovanović, P., Popović, L. Č. 2009b, PASRB, 9, 45

Jovanović, P., Popović, L. Č., & Simić, S. 2009c, NewAR, 53, 156

Jovanović, P., & Popović, L. Č. 2010, POBeo, 88, 91

Jovanović, P., Popović, L. Č., Stalevski, M., Shapovalova, A. I. 2010, ApJ, 718, 168

Jovanović P., Zakharov A. F., Popović L. Č., Petrović T., 2008, MNRAS, 386, 397

Juvela, M. 2005, A&A, 440, 531

Kawaguchi, T., & Mori, M. 2010, ApJL, 724, L183

Kawaguchi, T., & Mori, M. 2011, ApJ, 737, 105

Kayser R., Refsdal S., Stabell R., 1986, A&A, 166, 36

Keel, W. C. 1980, AJ, 85, 198

Keeton C. R., Gaudi B. S., Petters A. O., 2003, ApJ, 598, 138

Kellermann, K. I., Sramek, R., Schmidt, M., Shaffer, D. B., Green, R. 1989, AJ, 98, 1195

Kishimoto M., Hönig S. F., Antonucci R., Barvainis R., Kotani T., Tristram K. R. W., Weigelt G., Levin K., 2011, A&A, 527, A121+

Kochanek C. S., 1991, ApJ, 373, 354

Kochanek C. S., 2004, ApJ, 605, 58

Kogut A., Lineweaver C., Smoot G. F., Bennett C. L., Banday A., Boggess N. W., Cheng E. S., et al. 1993, ApJ, 419, 1

Komossa, S., Zhou, H., Wang, T. et al. 2008, ApJL, 678, 13

Kormendy, J., & Richstone, D. 1995, ARA&A, 33, 581

Kormendy, J., & Gebhardt, K. 2001, 20th Texas Symposium on relativistic astrophysics, 586, 363

Kovalev, Y. Y.; Lobanov, A. P.; Pushkarev, A. B.; Zensus, J. A. 2008, A&A, 483, 759

Krolik, J. H. 1998, Active Galactic Nuclei: From the Central Black Hole to the Galactic Environment, by J.H. Krolik. Princeton: Princeton University Press, 1998.

Krolik J. H., 2007, ApJ, 661, 52

Krolik J. H., Begelman M. C., 1988, ApJ, 329, 702

Laor A., Draine B. T., 1993, ApJ, 402, 441

Lauer, T. R. & Boroson, T. A. 2009, ApJ, 703, 930

Lawrence, A. 1991, MNRAS, 252, 586

Leipski, C., & Meisenheimer, K. 2012, Journal of Physics Conference Series, 372, 012037

Lewis, K. T. 2005, Bulletin of the American Astronomical Society, 37, 1240

Lewis, K. T., & Eracleous, M. 2006, ApJ, 642, 711

Lewis, K. T., Eracleous, M., & Storchi-Bergmann, T. 2010, ApJS, 187, 416

Li A., Draine B. T., 2001, ApJ, 554, 778

Lindegren, L., Babusiaux, C., Bailer-Jones, C., Bastian, U. et al. 2008, IAUS, 248, 217

Lucy L. B., 1999, A&A, 344, 282

Lutz, D., Sturm, E., Genzel, R., et al. 2000, ApJ, 536, 697

Lynden-Bell, D. 1969, Nature, 223, 690

Maccacaro, T, Garilli, B., Mereghetti, S. 1987, AJ, 93, 1484

Magorrian, J., & Tremaine, S. 1999, MNRAS, 309, 447

Maiolino, R., & Rieke, G. H. 1995, ApJ, 454, 95

Maiolino, R., Shemmer, O., Imanishi, M., et al. 2007, A&A, 468, 979

Maloney, P. R., Begelman, M. C. & Pringle, J. E. 1996, ApJ, 472, 582

Mannucci, F., Maiolino, R., Cresci, G., Della Valle, M., Vanzi, L., Ghinassi, F., Ivanov, V. D., Nagar, N. M., Alonso-Herrero, A., 2003, A&A, 401, 519

Mao, S., & Schneider, P. 1998, MNRAS, 295, 587

Marziani, P., Sulentic, J. W., Calvani, M., Perez, E., Moles, M. & Penston, M. V. 1993, ApJ, 410, 56

Massey, R., Rhodes, J., Ellis, R., et al. 2007, Nature, 445, 286

Mathis J. S., Rumpl W., Nordsieck K. H., 1977, ApJ, 217, 425

Mattila, K. 1970, A&A, 9, 53

Mattila, S., Meikle, W. P. S., 2001, MNRAS, 324, 325

Metcalf R. B., Madau P., 2001, ApJ, 563, 9

Mie, G. 1908, Annalen der Physik, 330, 377

Minezaki T., Chiba M., Kashikawa N., Inoue K. T., Kataza H., 2009, ApJ, 697, 610

Misselt, K. A., Gordon, K. D., Clayton, G. C., & Wolff, M. J. 2001, ApJ, 551, 277

Mor, R., & Netzer, H. 2012, MNRAS, 420, 526

Mor, R., Netzer, H.,& Elitzur, M. 2009, ApJ, 705, 298

Morgan, C. W., Kochanek, C. S., Morgan, N. D., & Falco, E. E. 2010, ApJ, 712, 1129

Mortlock, D. J., Warren, S. J., Venemans, B. P., et al. 2011, Nature, 474, 616

Mortonson M. J., Schechter P. L., Wambsganss J., 2005, ApJ, 628, 594

Mosquera A. M., Muñoz J. A., Mediavilla E., 2009, ApJ, 691, 1292

Mosquera A. M., Muñoz J. A., Mediavilla E., Kochanek C. S., 2011, ApJ, 728, 145

Nenkova M., Ivezić Ž., Elitzur M., 2002, ApJL, 570, L9

Nenkova M., Sirocky M. M., Ivezić Ž., Elitzur M., 2008a, ApJ, 685, 147

Nenkova M., Sirocky M. M., Nikutta R., Ivezić Ž., Elitzur M., 2008b, ApJ, 685, 160

Netzer, H. 1987, MNRAS, 225, 55

Netzer, H., Trakhtenbrot, B. 2007, ApJ, 654, 754

Neugebauer G., Matthews K., 1999, AJ, 118, 35

Newman, J. A., Eracleous, M., Filippenko, A. V. & Halpern, J. P. 1997, ApJ, 485, 570

Niccolini G., Woitke P., Lopez B., 2003, A&A, 399, 703

Nikutta R., Elitzur M., Lacy M., 2009, ApJ, 707, 1550

Oguri, M., Inada, N., Strauss, M. A., et al. 2012, AJ, 143, 120

Osterbrock, D.E. 1989, "Astrophysics of Gaseous Nebulae and Active Galactic Nuclei", University Science Books: Mill Valley

Osterbrock, D.E. & Ferland, G.J. 2006, "Astrophysics of Gaseous Nebulae and Active Galactic Nuclei", second edition, University Science Books: Mill Valley

Packham C., Young S., Hough J. H., Axon D. J., Bailey J. A., 1997, MNRAS, 288, 375

Perryman, M.A.C., de Boer, K.S., Gilmore, G., Hog, E. etc. 2001, A&A, 369, 339.

Pier E. A., Antonucci R., Hurt T., Kriss G., Krolik J., 1994, ApJ, 428, 124

Pier E. A., Krolik J. H., 1992, ApJ, 401, 99

Pier E. A., Krolik J. H., 1993, ApJ, 418, 673

Pogge R. W., 1988, ApJ, 328, 519

Pogge R. W., 1989, ApJ, 345, 730

Polletta, M., Weedman, D., Hönig, S., Lonsdale, C. J., Smith, H. E., & Houck, J. 2008, ApJ, 675, 960

Popović, L. Č. 2012, NewAR, 56, 74

Popović L. Č., Chartas G., 2005, MNRAS, 357, 135

Popović L. Č., Jovanović P., Mediavilla E., Zakharov A. F., Abajas C., Muñoz J. A., Chartas G., 2006, ApJ, 637, 620

Popović, L. Č., Jovanović, P., Stalevski, M., et al. 2012, A&A, 538, A107

Popović, L. Č., Mediavilla, E. G., Pavlović, R. 2000, SerAJ,162,1

Popović, L. Č, Mediavilla, E. G., & Muñoz, J. A. 2001, A&A, 378, 295

Popović L. Č., Mediavilla E. G., Jovanović P., Muñoz J. A., 2003, A&A, 398, 975

Popović, L. Č., Mediavlilla, E. G., Bon, E., Ilić, D., A&A, 2004, 423, 909

Popović, L. Č., Shapovalova, A. I., Ilić, D., Kovačević, A., Kollatschny, W., Burenkov, A. N., Chavushyan, V. H., Bochkarev, N. G., Leon-Tavares, J. 2011, A&A, 528, A130

Popović, L. Č., Smirnova, A.A., Kovačević, J. et al. 2009, AJ, 137, 3548

Porcas, R. W. 2009, A&A, 505L, 1.

Rafter, S. E., Crenshaw, D. M., Wiita, P. J. 2009, AJ, 137, 42

Ramos Almeida, C., Levenson, N. A., Rodríguez Espinosa, J. M., et al. 2009, ApJ, 702, 1127

Ramos Almeida C., Levenson N. A., Alonso-Herrero A., Asensio Ramos A., Rodríguez Espinosa J. M., Pérez García A. M., Packham C., Mason R., Radomski J. T., Díaz-Santos T., 2011, ApJ, 731, 92

Reynolds, C. S., & Nowak, M. A. 2003, Phys. Rep., 377, 389

Ricci, C., Walter, R., Courvoisier, T. J.-L., & Paltani, S. 2011, A&A, 532, A102

Richard, J., Kneib, J.-P., Ebeling, H., et al. 2011, MNRAS, 414, L31

Romano, P., Marzianii, P. & Dultzin-Hacyan, D. 1998, ApJ, 495, 222

Roseboom, I. G., Lawrence, A., Elvis, M., et al. 2012, submitted to MNRAS, arXiv:1205.4543

Schartmann M., Meisenheimer K., Camenzind M., Wolf S., Henning T., 2005, A&A, 437, 861

Schartmann M., Meisenheimer K., Camenzind M., Wolf S., Tristram K. R. W., Henning T., 2008, A&A, 482, 67

Schartmann M., Meisenheimer K., Klahr H., Camenzind M., Wolf S., Henning T., 2009, MNRAS, 393, 759

Schmidt, M. 1963, Nature, 197, 1040

Schmitt, J. L. 1968, Nature, 218, 663

Schneider, P., Ehlers, J., Falco, E.E. 1992, Gravitational Lenses, (Springer, Berlin)

Schneider P., Weiss A., 1986, A&A, 164, 237

Schneider P., Weiss A., 1987, A&A, 171, 49

Schneider, P., & Wambsganss, J. 1990, A&A, 237, 42

Sergeev, S. G., Pronik, V. I. & Sergeeva, E. A. 2000, A&A, 356, 41

Seyfert, C. K. 1943, ApJ, 97, 28

Shalyapin, V. N. 1995, AZh, 72, 668

Shapovalova, A. I., Burenkov, A. N., Carrasco, L., et al. 2001, A&A, 376, 775

Shapovalova, A. I., Popović, L. Č., Bochkarev, N. G., et al. 2009, NewAR, 53, 191

Shapovalova, A. I., Popović, L. Č., Burenkov, A. N., et al. 2010, A&A, 517, A42

Shen, Y., Leob, A. 2010 ApJ, 725, 249

Shi Y., Rieke G. H., Hines D. C., Gorjian V., Werner M. W., Cleary K., Low F. J., Smith P. S., Bouwman J., 2006, ApJ, 653, 127

Shields, G. A., Gebhardt, K., Salviander, S., Wills, B. J., Xie, B., Brotherton, M. S., Yuan, J., Dietrich, M. 2003, ApJ, 583, 124S

Shields, G. A., Rosario, D. J., Smith, K. L. et al. 2010, ApJ, 707, 936

Siebenmorgen R., Haas M., Krügel E., Schulz B., 2005, A&A, 436, L5

Sikora, M., Stawarz, Ł., & Lasota, J.-P. 2007, ApJ, 658, 815

Sim, S. A., Miller, L., Long, K. S., Turner, T. J., & Reeves, J. N. 2010, MNRAS, 404, 1369

Sluse D., Claeskens J.-F., Altieri B., Cabanac R. A., Garcet O., Hutsemékers D., Jean C., Smette A., Surdej J., 2006, A&A, 449, 539

Smith, A.G., Nair, A.D., Leacock, R.J., Clements, S.D., 1993;, AJ, 105, 437.

Stalevski, M. 2012, accepted for publication in BlgAJ

Stalevski, M., Jovanović, P., Popović, L. Č. 2008, POBeo, 84, 491

Stalevski, M., Jovanović, P., & Popović, L. Č.. 2010, POBeo, 89, 387

Stalevski, M., Fritz, J., Baes, M., Nakos, T., & Popović, L. Č. 2011, Baltic Astronomy, 20, 490

Stalevski, M., Fritz, J., Baes, M., Nakos, T., & Popović, L. Č. 2012a, MNRAS, 420, 2756

Stalevski, M., Jovanović, P., Popović, L. Č., & Baes, M. 2012b, MNRAS, 425, 1576

Stamatellos, D., & Whitworth, A. P. 2003, A&A, 407, 941

Steeghs, D., Harlaftis, E. T. & Horne, K. 1997, MNRAS, 290, L2

Strateva, I. V., Strauss, M. A., Hao, L., et al. 2003, AJ, 126, 1720

Strateva, I. V. Brandt, W. N., Eracleous, M., Garmire, G. 2008, ApJ, 687, 869S

Storchi-Bergmann, T., Nemmen da Silva, R., Eracleous, M., et al. 2003, ApJ, 598, 956

Strubbe, L. E., Quataert, E. 2009, MNRAS, 400, 2070

Tadhunter C., Tsvetanov Z., 1989, Nature, 341, 422

Taris, F., Souchay, J., Andrei, A. H., Bernard, M., Salabert, M., Bouquillon, S., Anton, S., Lambert, S. B., Gontier, A.-M., Barache, C. 2011, A&A, 526, id.A25

Teerikorpi, P., 2000, A&A, 353, 77

Tristram K. R. W., Meisenheimer K., Jaffe W., Schartmann M., Rix H., Leinert C., Morel S., Wittkowski M., Röttgering H., Perrin G., Lopez B., Raban D., Cotton W. D., Graser U., Paresce F., Henning T., 2007, A&A, 474, 837

Turner, T. J., Miller, L., George, I. M., Reeves, J. N. 2006, A&A, 445, 59

Urrutia, T., Lacy, M., Spoon, H., et al. 2012, ApJ, 757, 125

Urry C. M., Padovani P., 1995, PASP, 107, 803

van Bemmel I. M., Dullemond C. P., 2003, A&A, 404, 1

Veilleux, S. & Zheng, W. 1991, ApJ, 377, 89

Vestergaard, M. & Peterson, B. M. 2006, ApJ, 641, 689

Vidal E., Baes M., 2007, BaltA, 16, 101

Vignali, C., Piconcelli, E., Lanzuisi, G., et al. 2011, MNRAS, 416, 2068

Wada, K. 2012, ApJ, 758, 66

Wada K., Norman C. A., 2002, ApJL, 566, L21

Wada K., Papadopoulos P. P., Spaans M., 2009, ApJ, 702, 63

Wambsganss J., Paczynski B., Katz N., 1990, ApJ, 352, 407

Wang, J., & Merritt, D. 2004, ApJ, 600, 149

Weigelt G., Wittkowski M., Balega Y. Y., Beckert T., Duschl W. J., Hofmann K., Men'shchikov A. B., Schertl D., 2004, A&A, 425, 77

Weingartner J. C., Draine B. T., 2001, ApJ, 548, 296

Witt A. N., 1977, ApJS, 35, 1

Witt A. N., Gordon K. D., 1996, ApJ, 463, 681

Wittkowski M., Balega Y., Beckert T., Duschl W. J., Hofmann K., Weigelt G., 1998, A&A, 329, L45

Wolf S., 2003, CoPhC, 150, 99

Wu, S.-M., Wang, T.-G., & Dong, X.-B. 2008, MNRAS, 389, 213

Wyithe J. S. B., Agol E., Fluke C. J., 2002, MNRAS, 331, 1041

Wyithe J. S. B., Webster R. L., Turner E. L., 1999, MNRAS, 309, 261

Xu D. D., Mao S., Cooper A. P., Wang J., Gao L., Frenk C. S., Springel V., 2010, MNRAS, 408, 1721

Yonehara A., Hirashita H., Richter P., 2008, A&A, 478, 95

Yusef-Zadeh F., Morris M., White R. L., 1984, ApJ, 278, 186

Zakharov, F., Popović, L. Č., & Jovanović, P. 2004, A&A, 420, 881

Zakharov, A. F. 2009, NewAR, 53, 202

Zheng, W., Veilleux, S. & Grandi, S. A. 1991, ApJ, 381, 41